Structural insights into the organization and channel behavior of Pannexin isoforms

Thesis submitted to

Indian Institute of Science

in partial fulfillment for the award of the degree of

Doctor of Philosophy

by

Nazia Hussain

(15180)

Under the supervision of

Dr. Aravind Penmatsa

Molecular Biophysics Unit

Indian Institute of Science

March 2023

DECLARATION

This is to certify that the work reported in this thesis is original and has been carried out by Nazia Hussain under the guidance of Dr. Aravind Penmatsa. The work has not been submitted to any other institute for a diploma or degree. The Indian Institute of Science is authorized to lend this thesis to other institutions or individuals for scholarly research. The author has conformed to the norms and guidelines given in the Ethical code of Conduct of the Institute.

Dr. Aravind Penmatsa
(Research Supervisor)

Nazia Hussain
(Candidate)

ACKNOWLEDGMENT

Alhamdulillah! am extremely grateful to all the individuals who have supported me throughout my Ph.D. journey. Firstly, I want to express my gratitude towards my guide Dr. Aravind Penmatsa for providing me with the opportunity to work under his guidance. Being a part of the lab during its formative years has allowed me to learn a great deal directly from him, which has enabled me to become an independent researcher. I will always be thankful for his kindness and support.

I also extend my appreciation to my collaborators, including Dr. K.R. Vinothkumar, Prof. S.K. Sikdar, Ashish Apotikar, Shabareesh, and Sourajit, for their invaluable assistance with my work. In particular, I want to thank Dr. K.R. Vinothkumar, Dr. Somanth Dutta, and Dr. Aravind Penmatsa for teaching me grid freezing, data collection, and the theoretical aspects of Cryo-EM.

I am also thankful to Sucharita Bose and the National Electron Cryo-Microscopy facility, BLiSc, Bangalore, for their assistance with grid screening and data collection, as well as the advanced Cryo-EM facility, IISc, for their support with preliminary data collection. I am grateful for the computational support provided by the high-performance computing facility "Beagle," which allowed me to process multiple Cryo-EM datasets simultaneously. Additionally, I want to thank the MBU Staff (Pavitra) and X-ray facility members (Dhruva, Babu, and Dr. James).

Although nerve-racking, I thoroughly enjoyed my interaction with my comprehensive committee (Prof. N. Srinivasan, Dr. Somnath Dutta, Dr. K.R. Vinothkumar, Dr. Ramray Bhat, and Dr. Aravind Penmatsa). I have fond memories of the questions asked by Prof. Srinivasan on X-ray Crystallography. I want to express my gratitude towards past and present chairmen Prof. Raghavan Varadarajan, Prof. N. Srinivasan, and Prof. Siddhartha P. Sarma.

I am grateful to the MBU faculty members who taught me the concepts through the rigorous coursework. I want to thank Prof. N. Srinivasan and Dr. Anand Srivastava for the Conformations course, Prof. Suguna and Dr. Aravind Penmatsa for X-ray crystallography, and Prof. Siddhartha P. Sarma and Dr. Mahavir Singh for the Spectroscopy and NMR course. I also want to express my appreciation towards Prof. MRN Murthy, Prof. B. Gopal, and Prof. T. N. Gururaja for their extensive course on X-ray crystallography. The

experience of interacting with them and learning from them has been unforgettable. I regret not putting in more effort during my coursework with Prof. Siddhartha P. Sarma and appreciate Dr. Giriraj Sahu and Prof. Rishikesh Narayanan for their valuable discussions regarding my experiments, which have helped me increase the depth of my knowledge. I am forever indebted to my labmates for their support, who have made my stay on campus enjoyable. I have learned everything in the lab from my seniors, Shabareesh, Sushant, Aditya, and Puja, and have spent a carefree and happy time with them. I will always cherish the time I spent with Puja, a wonderful senior who I have missed dearly in the final year of my Ph.D.

Arunabh and Smruti have been a blessing in the lab. Smruti's constant jokes have evoked mixed feelings of annoyance and appreciation for his humor. I will always be thankful to him for being a constant in my life. Arunabh, on the other hand, has been instrumental in my research progress, challenging me with thought-provoking questions and offering constructive criticism that has helped me improve. I have shared numerous meals with both of them and have enjoyed their company.

Dipanjana and Archisman are also invaluable members of my lab, and I am grateful for their unwavering support. Interestingly, they always seem to view my work in a positive light, even when I am unsure of myself.

I extend my gratitude to all past and present members of my lab, including Samreen, Himansha, Pragya, Ananth, Arnab, Nandika, Shirshadri, Deepthi, Biswanath, Shashank, Raja, Guru, Shabareesh, Sushant, Puja, Aditya, Balu, and especially Samreen for her assistance with administrative tasks. They have collectively created a wonderful environment in which to work.

I have spent a wonderful time with Vikram. He has taught me many valuable lessons that will help me in my career and life. I am grateful to Pehu, Ila, Firdausi, Sameer, and Sarah. My friends Ila, Pehu, Sameer, Sarah, Vikram, Firdousi, Pankaj, and Ashish have been an immense source of support throughout my journey. I am grateful for their guidance and counsel during challenging times, and I truly believe I would not have been able to complete my Ph.D. without their unwavering support. A special thanks to Pehu for being a constant in my life.

I have fond memories of spending time with Pankaj, Ashish, Suhail, Debashree, Divyansh, Sivaji, Venkat, Rituparna, Nayanika, Suman, Tabish, Gaurav, and Vasam, and am thankful for the interactions we've had.

Lastly, I would like to express my appreciation for my batchmates Pehu, Arunabh, Ashish, Debashree, Vasam, Krishnakanth, Munmun, Nisha, Rohit, Rohan, Priyanka, Vandana, Haaris, Hansika, and Souptik, for making my time in the program enjoyable.

I am immensely grateful to my family for their unwavering support.

-Nazia Hussain

Publications

- Majumder P, Khare S, Athreya A, **Hussain N**, Gulati A, Penmatsa A. **Dissection of Protonation Sites for Antibacterial Recognition and Transport in QacA, a Multi-Drug Efflux Transporter.** J Mol Biol. 2019 May 17;431(11):2163-2179. doi: 10.1016/j.jmb.2019.03.015. Epub 2019 Mar 23. PMID: 30910733; PMCID: PMC7212025.

- **Nazia Hussain**, Ashish Apotikar, Pidathala Shabareesh, Sourajit Mukherjee, Ananth Prasad Burada, Sujit Kumar Sikdar, Kutti R. Vinothkumar & Aravind Penmatsa. **Structural insights into pore dynamics of human Pannexin isoforms.**bioRxiv;2022.09.09.507385;doi:https://doi.org/10.1101/2022.09.09.507385

Table of Contents

Abbreviations

POPE **P**hosphatidyl **E**thanolamine

FBS **F**etal **B**ovine **S**erum

SDS-PAGE **S**odium **D**odecyl **S**ulfate **P**oly **A**crylamide **G**el **E**lectrophoresis

WT **W**ild **T**ype

DM **D**ecyl-ß-**D**-**M**altopyranoside

DDM **D**odecyl-ß-**D**-**M**altopyranoside

OG **O**ctyl **G**lucopyranoside

OM **O**ctyl **M**altopyranoside

UDM **U**ndecyl-ß-**D**-**M**altopyranoside

CHS **C**holesteryl **H**emi **S**uccinate

LMNG **L**auryl **M**altose **N**eopentyl **G**lycol

GDN **G**lyco**d**iosgeni**n**

EL **E**xtracellular **L**oop

IL **I**ntracellular **L**oop

FSEC **F**luorescence-detection **S**ize **E**xclusion **C**hromatography

TM **T**rans **M**embrane

PANX1/PANX1$_{WT}$ **Pan**ne**x**in**1** **W**ild **T**ype

PANX1$_{R217H}$ Congenital mutant of **Pan**ne**x**in**1** (**R217H)**

PANX1$_{DM}$ **Pan**ne**x**in**1** **D**ouble **M**utant

PANX3 **Pan**ne**x**in**3** Wild Type

ATP-γS **A**denosine 5’ –[γ-thio] **t**riphos**p**hate tetralithium salt

CHAPSO [3-[(3-**Ch**olamidopropyl) dimethylammonio]-2-hydroxy-1-propanesulfonate]

Symbols

λ_{Ex} Excitation wavelength

λ_{Em} Emission wavelength

α Alpha

β Beta

μ Micron

° Degree

ϵ Epsilon

Å Angstrom

Synopsis

Pannexins are a family of glycoproteins involved in multiple physiological and pathological processes, such as apoptosis, cell migration, odontoblast differentiation, and viral replication through ATP release activity[1–4]. They were discovered in the early 2000s through their limited sequence similarity with innexins, the invertebrate gap junctions[5]. However, the Pannexin isoforms do not form gap junctions and act as single membrane channels[6].

The Pannexin family consists of three isoforms, Pannexin1, 2, and 3. Pannexin1 is the most widely studied protein and has ubiquitous expression. Pannexin3 is observed to play an essential role in the development of skin, bone, cartilage, and teeth[7]. Although Pannexin2 also has a broad distribution like Pannexin1, little is known about this isoform.

Pannexin1 is activated with diverse stimuli, including mechanical stress, high extracellular potassium, depolarization, and C-terminal cleavage by caspases 3/7[8]. Nevertheless, high extracellular potassium and depolarization remain the most commonly used stimuli to understand the function of Pannexin1.

Pannexin2 is the largest among the three isoforms, with its comparatively longer C-terminus than Pannexin1 and 3. It is mainly localized in the cytoplasmic compartments as opposed to the other isoforms that primarily reside in the plasma membrane. Although not much is known about the functions of Pannexin2, it has been reported to play a vital role in keratinocyte differentiation, skin homeostasis, and the growth of glioma tumors[9].

Pannexin3 is the smallest isoform and shares 42 % identity with Pannexin1. It is a major candidate for calcium homeostasis and regulates osteoblast differentiation through its ER calcium channel activity[7,10]. Moreover, Pannexin3 plays an important role in skeletal formation and development, odontoblast differentiation, and growth of metatarsals through its ATP and calcium release activity through mice experiments.

This study attempts to understand the structural-functional relationship between Pannexin isoforms and the Pannexin1 mutants.

Chapter 1 outlines a detailed introduction to the Pannexin family, especially Pannexin1, as it is the most studied isoform. It provides an overview of the involvement

of Pannexin isoforms in health and disease. The Pannexin1 activation mechanisms are discussed in detail. The chapter also covers the contradictions in the literature on the opening and closing of the Pannexin1 channel. This thesis also summarize the available literature on Pannexin isoforms 2 and 3 and the congenital mutant of Pannexin1.

Chapter 2 provides the details of the methods that have been used in the study. The thesis employs a wide array of expression, biochemical, and electrophysiological assays in combination with electron cryomicroscopy (Cryo-EM). A brief overview of the steps involved in sample preparation, assays, and Cryo-EM processing is described in this chapter.

In **Chapter 3,** I delve into the optimization of protein purification, which includes choosing a suitable detergent that would stabilize the protein outside its native environment. It also describes our attempts and the rationale for optimizing the Cryo-EM parameters required to get a moderate resolution structure from a small dataset of particles. We determined the structure of Pannexin1 at a resolution of 3.75 Å in the presence of high potassium that stimulates the opening of the channel.

The structure reveals that transmembrane helices in Pannexin1 are arranged similarly to other large pore channels such as LRRC8, Connexins, and Innexins. We also explored the voltage dependence of the Pannexin1 channel and observed weak dependence of Pannexin1 to high positive voltages, thereby displaying outward rectification. Although the ATP release activity of Pannexin1 has been explored extensively, we provided a proof of concept by attempting to measure the binding affinity of Pannexin1 with ATP-γS using microscale thermophoresis.

In **Chapter 4,** I describe the structure determination of the Pannexin1 congenital mutant (R217H) that causes intellectual disabilities and hearing loss and a double pore mutant (W74R, R75D), which mimics the pore-gating residues of Pannexin2 at a resolution of 3.9 and 4.3 Å respectively. A comparison of the wild-type and the mutants reveals that the mutation in the channel induces structural changes that lead to the partial closure of the pore. Although the overall structure of the mutants resembles the wild-type Pannexin1, changes in the TM1 (transmembrane1) and the ECD (extracellular domain) lead to the movement of the pore-gating residues, thereby partially closing the channel. Apart from exploring the structural changes as a

consequence of the mutations, we aimed to understand the functional impact of these mutations on the channel. We measured the voltage dependence and the ATP-γS binding affinities of the mutants and drew a comparison with the wild-type Pannexin1. The binding affinities of the mutants calculated with an ATP analog (ATP-γS) revealed a decrease in the affinity of the mutants compared to the wild-type suggesting a role for these residues in the ATP-γS interactions. Patch clamp studies revealed that the pore residues in Pannexin1 do not play a role in sensing the voltage. However, the measured conductance of R217H implies a role of arginine in the voltage dependence of the channel.

Chapter 5 describes the structural organization of Pannexin3 and a comparison with Pannexin1. The overall fold of Pannexin3 resembles that of Pannexin1 but with several unique features. The interior surface electrostatic potentials in Pannexin3 are uniquely organized within the pore and have a more prominent lateral tunnel that could serve as a permeation pathway for small ions. The pore of the Pannexin3 is wider than the Pannexin1and has isoleucine instead of tryptophan as a gating residue. The vestibule is also organized as two distinct compartments with distinct surface charges. To understand the functional differences in Pannexin isoforms, I performed ATP binding studies of Pannexin3 with ATP-γS, a non-hydrolyzable ATP analog. MST studies revealed a decreased ATP-γS interaction affinity of Pannexin3 compared to Pannexin1. We also investigated the voltage dependence of Pannexin3 in HEK293 cells. In contradiction to the earlier studies performed in N2A cells, we observed voltage dependence of Pannexin3 at higher voltages similar to Pannexin1 wild-type suggesting an overlap inchannel behavior among Pannexin isoforms in their electrical properties.

In **Chapter 6,** I conclude the thesis with the major findings of the study. This chapter outlines a comparison between Pannexin members and other large pore ion-channels. I also discuss the differences between the pore radius of the Pannexin isoforms and the mutants and their relevance in the charge alteration. Moreover, I discuss the functional relevance of the changes in the structure ofPannexin isoforms and the mutants and draw comparisons with the existing literature.

The study provides a starting point for understanding the structural differences in the isoforms, which can be correlated with the differences in their functions. Although we

have explored the voltage dependence of Pannexin1 and 3, ion selectivity in the isoforms could be addressed to have a better understanding of their functions. We have made a preliminary attempt to understand the ATP-γS binding. Further, extensive screening of potential binding sites followed by molecular simulations can be done to map the ATP binding site in Pannexin1 and 3. Moreover, the Pannexin1 / 3 ATP bound structures would clarify the role of these channels in ATP interactions and release. Likewise, understanding the role of lipids in channel gating would be advantageous for the large pore channel community.

Summary

Chapter 1: Introduction

Chapter 2: Materials and methods

Chapter 3: Structural and functional characterization of human Pannexin1

Chapter 4: Structural insights into pore dynamics in Pannexin1 mutants

Chapter 5: Structural and functional comparison of Pannexin isoforms.

Chapter 6: Discussion

References

1. Harcha, P. A., López-López, T., Palacios, A. G. & Sáez, P. J. Pannexin Channel Regulation ofCell Migration: Focus on Immune Cells. *Front. Immunol.* **12**, (2021).
2. Makarenkova, H. P. & Shestopalov, V. I. The role of pannexin hemichannels in inflammation andregeneration. *Front. Physiol.* **5**, (2014).
3. Paoletti, A. *et al.* Editorial: Pannexin-1-the hidden gatekeeper for HIV-1. *J. Leukoc. Biol.* **94**, 390–392 (2013).
4. Iwamoto, T. *et al.* Pannexin 3 regulates proliferation and differentiation of odontoblasts via itshemichannel activities. *PloS One* **12**, e0177557 (2017).
5. Panchina, Y. *et al.* A ubiquitous family of putative gap junction molecules. *Curr. Biol.* **10**, R473–R474 (2000).
6. Penuela, S., Gehi, R. & Laird, D. W. The biochemistry and function of pannexin channels.
   Biochim. Biophys. Acta – Biomembr. **1828**, 15–22 (2013).
7. Ishikawa, M. *et al.* Pannexin 3 functions as an ER Ca2+ channel, hemichannel, and gap junctionto promote osteoblast differentiation. *J. Cell Biol.* **193**, 1257–1274 (2011).
8. Sandilos, J. K. *et al.* Pannexin 1, an ATP Release Channel, Is Activated by Caspase Cleavage ofIts Pore-associated C-terminal Autoinhibitory Region. *J. Biol. Chem.* **287**, 11303–11311 (2012).
9. Xu, X., Hao, Y., Xiong, S. & He, Z. PANX2 and brain lower grade glioma genesis: A bioinformaticanalysis. *Sci. Prog.* **104**, 003685042110118 (2021).
10. Ishikawa, M. & Yamada, Y. The Role of Pannexin 3 in Bone Biology. *J. Dent. Res.* **96**,

CHAPTER 1

Introduction

1.1 Overview

Intercellular communication is vital for the maintenance of homeostasis between the cells. In neurons, two modes of synaptic communication have been reported, namely, chemical and electrical neurotransmission (Fig. 1.1). The chemical synapse was thoroughly studied in early 1930, for which Otto Loewi and Sir Henry Dale got the Nobel

prize in 1936[1] followed by Bernard Katz who defined vesicular release[2]. The electrical synapse was discovered 30 years later by David Potter and Edwin Furshpan[3], which paved the way for the discovery of gap junctions[4].

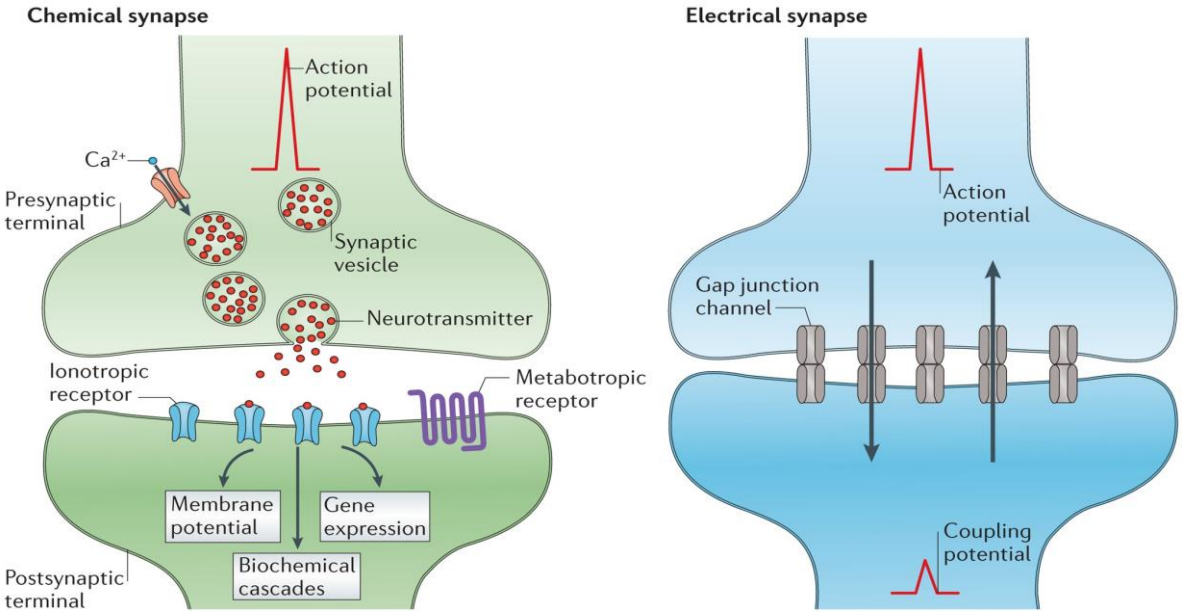

Fig. 1.1: Two modes of synaptic transmission reported in neurons[5]. The chemical synapse includes the movement of neurotransmitters through synaptic vesicles. The electrical synapse includes the rapid movement of ions through a continuous path formed by gap junctions.

Gap junctions are found in the entire animal kingdom; within vertebrates, they are known as connexins and as innexins in invertebrates[6]. The PANX family was discovered as the second family of gap junctions in the human genome in early 2000 by Panchin *et al*. while discovering the homologs for innexins[7]. It is a family comprising three isoforms PANX1, 2, and 3[6,8].

1.2 Discovery of PANXs

Panchin *et al*. were the first to discover the Pannexin (PANX) family of proteins in 2000 in the different taxonomic groups, including vertebrates. Using PCR with degenerate primers, they generated the sequence clones, homologous in molluscs and flatworm cDNA library. The authors observed the presence of four transmembrane helices and two cysteine residues in extracellular loops in PANXs, like innexins and connexins.

Due to their presence in multiple animal phyla such as platyhelminthes, nematoda, arthropoda, mollusca, and chordata, these proteins were named Pannexins (PANXs) from the Latin (pan—all, throughout and nexus—connection, bond)[7].

1.3 PANXs do not form gap junctions

Vertebrate gap junctions, connexins, typically show junctional conductance in a paired oocyte assay, where robust trans junctional currents have been observed once the oocyte pair was established[9]. A similar setup was used for testing the gap junctional properties of PANX channels. Most reports negated the idea of PANXs forming gap junction[10,11,12], although few reports observed gap junctional properties in Hela cell lines and oocyte pairs expressing PANX1[13,14].

In the last 15 years, the PANX field has agreed that PANXs do not form gap junctions and remain as large pore channels. Interestingly, PANXs have an N-glycosylation site at their extracellular loop, which is absent in gap junctions[11,15,16]. Their inability to form gap junctions was linked to their glycosylation site, which was recently proven by Ruan *et al*. In their study, the authors mutated the glycosylation site(N255) to alanine, they observed a mixed population of single channels and gap junctions[17]. In conclusion, glycosylation at the extracellular loop in PANXs makes them incompatible with forming gap junctions.

1.4 PANXs topology and glycosylation

PANXs are a family of glycoproteins discovered due to their limited sequence homology with invertebrate gap junctions, innexins, and have no sequence homology with vertebrate gap junctions, connexins. Although there is no sequence similarity between connexins and PANXs, these proteins exhibit similar topologies. The PANX protomer contains four transmembrane α-helices, two extracellular loops, and one

intracellular loop, with their amino terminus and carboxy terminus towards the cytoplasm (Fig. 1.2-a). PANX members exhibit similarity in the N-terminus, and the maximum diversity is observed in C-terminus. PANX1 and PANX3 display greater sequence similarity and share 41% identity, whereas PANX2, is the most diverse isoform with only 27% identity with PANX1. PANX2 also has a longer C-terminus compared to its isoforms. PANXs are glycoproteins and have glycosylation at their extracellular loops. PANX2 and 3 have N-glycosylation at the first extracellular loop at N86 and N71 residue, respectively, while PANX1 is N-glycosylated at N255(human) in the second extracellular loop[8] (Fig. 1.2-b). N-Glycosylated PANX1 have three species gly0, gly1, gly2[18,19].

N-Glycosylation in PANX1 has been proposed to play a role in the proper trafficking of the channel to the membrane and can affect the channel's localization[15].

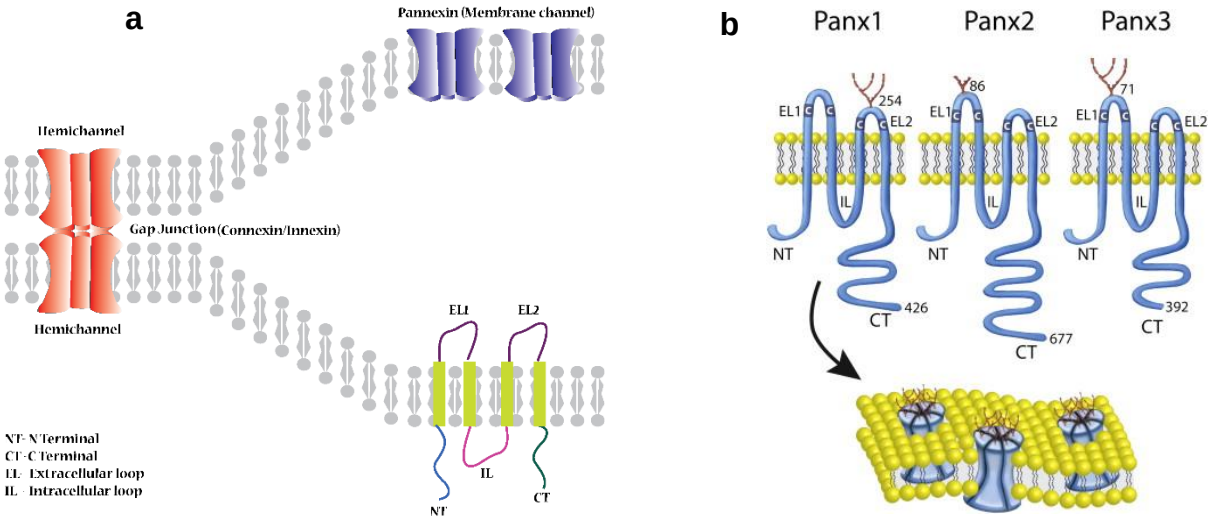

Fig. 1.2: a) PANXs have a similar topology as innexins and connexins consisting of four transmembrane helices, two extracellular loops, one intracellular loop, and N, C terminus toward the cytoplasmic side, **b)** N-Glycosylation site in PANX isoforms shows the presence of N-glycosylation in PANX1 in extracellular loop 2, whereas PANX2 and 3 exhibits N-glycosylation at extracellular loop 1[8].

1.5 PANXs expression

Apart from humans, PANXs expression has been observed in other species such as *Rattus norvegicus* (rat), *Canis familaris* (dog), *Danio rerio* (zebrafish). However, these proteins are well characterized in humans and mice. PANX1 has ubiquitous

expression and is expressed in the brain, blood endothelium, heart, skeletal muscle, ovary, spleen, skin, testis, placenta, thymus, prostate, lung, liver, small intestine, pancreas, colon, and erythrocytes determined by northern blot at mRNA level and by PANX1 specific antibody at protein level[11,20].

Initially, PANX2 was believed to have more restricted localization, and the expression was observed in the rodent brain and spinal cord by northern blot analysis[20,21,22]. However, recent studies have shown PANX2 expression in the skin[23] and other tissues[24] and are believed to have more ubiquitous expression than previously thought.

PANX3 exhibits more restricted localization than other PANX isoforms and has been reported to express in skin, cochlea, bones, teeth, and cartilage[25,26].

1.6 Ion selectivity in PANX1

Large pore channels, PANXs are not selective like canonical potassium channels. For example, the fundamental property of K^+ channels is to distinguish between potassium and other ions and conduct potassium ions across the membranes[27]. Even though there is only a minor difference between the radius of K^+(1.33) and Na^+(0.95), the potassium channel excludes Na^+. However, PANX1 allows the rapid movement of different sizes of ions[28,29].

With vast and diverse literature on PANX1 selectivity, it is difficult to conclude if PANX1 is non-selective or anionic, as suggested by various groups[28,30,31]. For instance, Ma *et al.* determined the permeability of various monovalent anions by measuring the E_{rev} when the extracellular solution was replaced with different anions. The rank order for the permeabilities of different anions at +70 mV suggests $NO3^-$be highly permeable and gluconate least permeable[30].

$NO3^-$ >I− >Br− >Cl− > F− >>aspartate− ≈glutamate− ≈gluconate−

A similar study was done by Michalski *et al.,* where they assessed the residue involved in the anionic selectivity of PANX1. They hypothesized the role of positive residue R75 in anion selectivity. R75 was mutated to neutral, hydrophobic, and charge reversal mutants, keeping the intracellular solution constant (NaCl) while the extracellular solution was changed. When the solution was changed to gluconate, E_{rev} shifted to

+26 mV, suggesting higher chloride permeability over gluconate. The authors observed a decrease in the chloride permeability when the charge was neutralized, whereas the charge reversal mutant showed more permeability to gluconate over chloride[28].

In another study by Narahari *et al*., it was observed that when the C-terminus of PANX1 was cleaved off, it allowed the release of ATP and other large metabolites[29]. Although the movement of large anionic molecules was more rapid compared to large cationic metabolites such as spermidine, PANX1 did not eliminate the passage of cationic molecules completely. In conclusion, although PANX1 shows some preference towards anionic molecules, it does not discriminate against cationic molecules extensively.

1.7 PANX1 functions as an ATP release channel

ATP has been considered as the cellular energy store. Besides acting as an energy source, ATP has gained recognition as a signaling molecule. To act as a transmitter, ATP must pass through the plasma membrane. One of the ways ATP can be released is through vesicle exocytosis, like other neurotransmitters, which has been observed in chemical synaptic transmissions, such as the release of norepinephrine, acetylcholine, and GABA [32–34].

The second mode of ATP release is during a pathological condition or apoptosis, where the membrane loses integrity, and cellular contents and ATP are released out of the cell[35–37]. The third way is through membrane proteins that allow the conditional movement of ATP. Several membrane proteins have been proposed to be putative ATP release channels, including CFTR, CALHMs, Connexin 43 hemichannels, and PANX channels[31,38–41].

Several criteria must be met to act as an ATP release channel. Here, a few critical and essential criteria are discussed. The first essential criterion is the ability to permeate ATP and its expression in ATP-releasing cells. For example, erythrocytes release ATP, but there is no gap junction formation in these cells, invalidating connexins as universal ATP release channels[42,43]. However, PANX1 expression has been observed in erythrocytes, and also ATP release has been observed[42,44].

Like connexins, CALHMs also require extracellular calcium removal, which might not even be possible in pathological conditions. Moreover, a protein must be able to activate at resting membrane potential allowing the ATP release along the concentration and voltage gradient. Unfortunately, both connexins and CALHMs open at a positive potential. PANX1, on the other hand, can be open at resting membrane potential in the presence of a stimulus[45]. Interestingly CFTR is not permeable to ATP, suggesting CFTR cannot be responsible for ATP release[41,46].

Moreover, multiple groups independently have shown the ATP release through PANX1 channels in different cell types[41,47–49]. In short, PANX1 channels fulfill all the requirements and are considered the cells' main ATP release channels.

1.8 Mechanism of PANX1 activation

PANX1 channels can be activated reversibly and can have small or large conductance states[50]. The small conductance (70-80 pS) is mediated by voltage, whereas large conductance can be moderated by high extracellular potassium and high intracellular calcium. Large conductance is associated with the release of ATP, whereas small conductance can mediate only the release of ions but not ATP[51].

1.8.1 PANX1 Voltage-mediated activation

The first evidence for voltage-mediated activation of PANX1 was given by Ma *et al.* in mammalian HEK293 cells by whole-cell patch recording. The cells were clamped at -60, and the voltage steps of 20mV were given from -120 to +80 mV. Control recordings with the untransfected cells were done to ensure that the currents were generated from the overexpressed PANX1. Moreover, the PANX1 channels were activated at +10 mV or more, and PANX1 inhibitors, carbenoxolone, and probenecid attenuated this current. The PANX1-expressing cells led to the generation of outward rectifying currents[52].

The voltage-activated PANX1 channel is permeable to chloride ions but not ATP and large molecules. However, this conformation is activated only at positive potentials, and the physiological role of chloride permeant PANX1 is still unknown[53].

Although PANX1 channels are activated at a positive potential, it is still difficult to conclude if they are voltage-gated channels like canonical voltage-gated channels.

For example, in a typical voltage-gated potassium channel (K_v), there is a separate structural domain for sensing the voltage, known as the voltage sensor domain consisting of four transmembrane helices (S1-S4). The S4 consists of positively charged residues lined up. This domain is linked to the other structural domain known as the ion conduction domain.

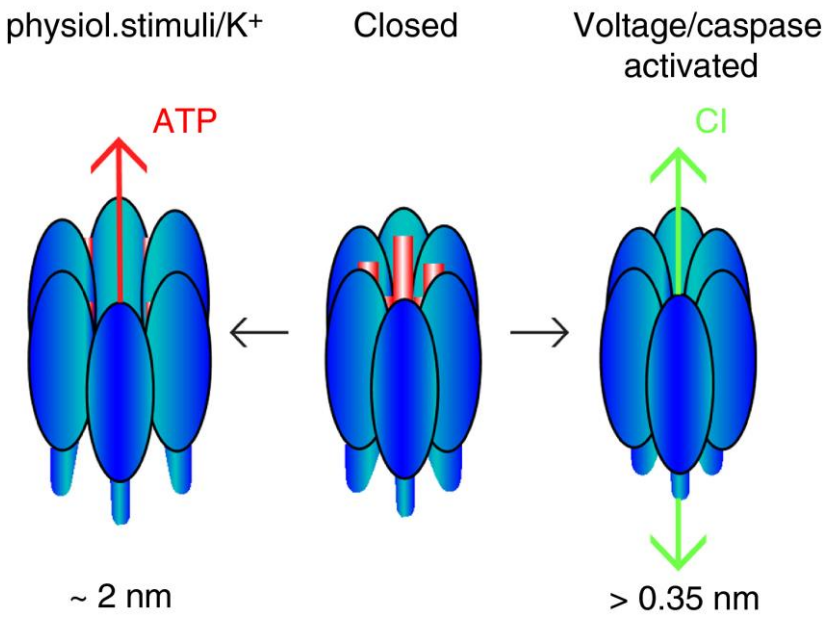

Fig. 1.3: The Illustration of PANX1 opening in response to different stimuli suggests that high extracellular potassium leads to a larger channel opening than when activated by voltage[53].

The voltage domain senses a change in the membrane, and the change in the conformation in the voltage domain is translated to the ion conduction domain leading to the opening or closing of the channel[54].

In contrast, structural analysis of PANX1 does not reveal two domains in a subunit; also, no such transmembrane region consisting of a stack of positive charge is present in PANX1[17,28,55–57].

Voltage dependence in PANX1 remains controversial, with the emergence of multiple reports on the voltage dependence of PANX1. Although HEK293 cells have been used in the studies, different results were obtained[53,58]. Ma *et al.* have observed the activation of PANX1 in response to depolarization. However, in a similar setup, Chiu *et al.* failed to observe the activation of PANX1 by voltage. At this juncture, a conclusion about what parameters or changes led to such diverse observations cannot be drawn.

In similar lines, Michalski *et al.* observed PANX1 to weakly activated channels, but a modification of the N-terminus by adding GS (glycine-serine motif) led to the robust voltage activation of PANX1. The authors inserted GS after the first methionine and observed an increase in open probability and the number of unitary conductance classes in the single-channel recording. Although the addition of GS increased the voltage-dependent activation of PANX1, the insertion of GFP at the N-terminus led to the elimination of voltage-dependent channel activity[59].

1.8.2 Activation by high extracellular potassium

High extracellular potassium leads to the activation of PANX1, observed in oocytes. However, electrophysiology data suggests that activation of PANX1 is observed only during the depolarization of the membrane by positive potentials. To understand this discrepancy, Silverman *et al.* performed electrophysiology recordings in oocytes at negative potentials (-50 mV) at which the channel is closed. An increasing potassium concentration increased the current amplitude, which was attenuated by PANX1 inhibitors, carbenoxolone, and probenecid. This dose-dependent effect of extracellular potassium was observed for a minimum concentration of 20 mM. Moreover, replacing Na^+ with choline did not change the effect indicating the need for extracellular potassium to activate PANX1 channels[60].

1.8.3 Activation by purinergic receptors

ATP released by PANX1 can act as a signaling molecule or is disintegrated into ADP, AMP, and adenosine by ectonucleotidases in the extracellular space. ATP activates two purinergic families of receptors, P2XRs and P2Yrs. P2XRs are a family of 7 proteins named P2XR1-7, whereas P2Yrs are a family of 8, P2YR1-8[61,62]. Apart from ATP, ADP can act as an agonist for P2Y receptors, and adenosine can activate P1/adenosine receptors[63].

At this juncture, two modes of activation of PANX1 can be proposed. A) Through signaling molecules; Activation of P2X-Y receptors leads to the release of intracellular calcium[64], which can activate PANX1, b) Physical activation; PANX1 and P2X receptors have been observed to co-localize[62,65] in the different systems by co-immunoprecipitation, this physical coupling can lead to a conformational change in PANX1 leading to ATP release through PANX1[66].

1.8.4 PANX1 Activation by mechanical stimulation

Mechanosensitivity in PANX1 channels was observed by Bao *et al*. through a single-channel patch clamp[45]. The mechanical stress was applied to cell-attached or excised membrane patches through suction in the patch pipette. PANX1 showed an increase in the activity proportionate to the applied stress. PANX1 switched from lower sub-conductance to high conductance or from closed state to higher conductance state. A typical response of mechanical stress from the cell is the release of calcium. An increase in cytoplasmic calcium concentration leads to the spread of a calcium wave that can propagate to neighboring and distant cells. Purinergic receptors, P2X, play an essential role in calcium wave formation and are activated by the ATP released by PANX1. In another study, Lee *et al*. showed the PANX1-mediated calcium release in invasive cancer cells through focus ultrasound stimulation (FUS). FUS is a technology that aims to discover potential mechanosensitive mediated cellular processes. The authors demonstrated the direct activation of PANXs located in ER to generate calcium waves. Although PANX1 in ER has a mechanosensitivity, no mechanosensitivity was detected for the PANX1 present in the plasma membrane[67].

1.8.5 PANX1 C-tail cleavage by Caspase

Irreversible activation of PANX1 is observed during apoptosis, where cleavage of the C-terminus by caspase3/7 results in a constitutively open channel.

Apoptosis is a programmed cell death essential for maintaining tissue homeostasis that occurs in many pathological and physiological states and is accompanied by cell shrinkage, DNA fragmentation, and membrane blebbing[35]. Apoptosis can be initiated by the intrinsic/mitochondrial pathway or extrinsic/death receptor pathway. It is caspase-dependent cell death, which is considered immunologically silent[68]. These caspases have cysteine at their active site and cleave their targeted protein at specific aspartic acid. Extrinsic or intrinsic factors can trigger the activation of the proteolytic caspases[69].

The extrinsic factors activate the extrinsic pathway mediated by death receptors such as Fas, and binding of the ligands to these receptors leads to the recruitment of adaptor protein which activates the initiator caspase, caspase 8[70,71].

On the other hand, intrinsic factors such as intracellular stress, infection, and

chemotherapeutic drugs lead to the activation of the intrinsic pathway, where the mitochondrial outer membrane becomes permeable to the release of cytochrome c, which initiates a signaling cascade leading to the activation of caspase 9. Both the pathways converge upon activation of executioner caspases, caspases 3 and 7, that act on the PANX1 C-terminus, thereby opening the channel for the release of ATP, which acts as a signal for clearance of apoptotic cells[72–74].

In a study by Gizem Ayna *et al*., a decrease in ATP release from the apoptotic cells was observed with no leakage of cellular contents[75]. An investigation into different mechanisms, such as exocytosis and blebbing, did not show any effect on ATP release, indicating a membrane protein's role in ATP release. PANX1 has a conserved caspase cleavage motif (DVVD) at its C-terminus (residue 376-379) and has been identified as a mediator as a find-me signal from the apoptotic cells[76].

.

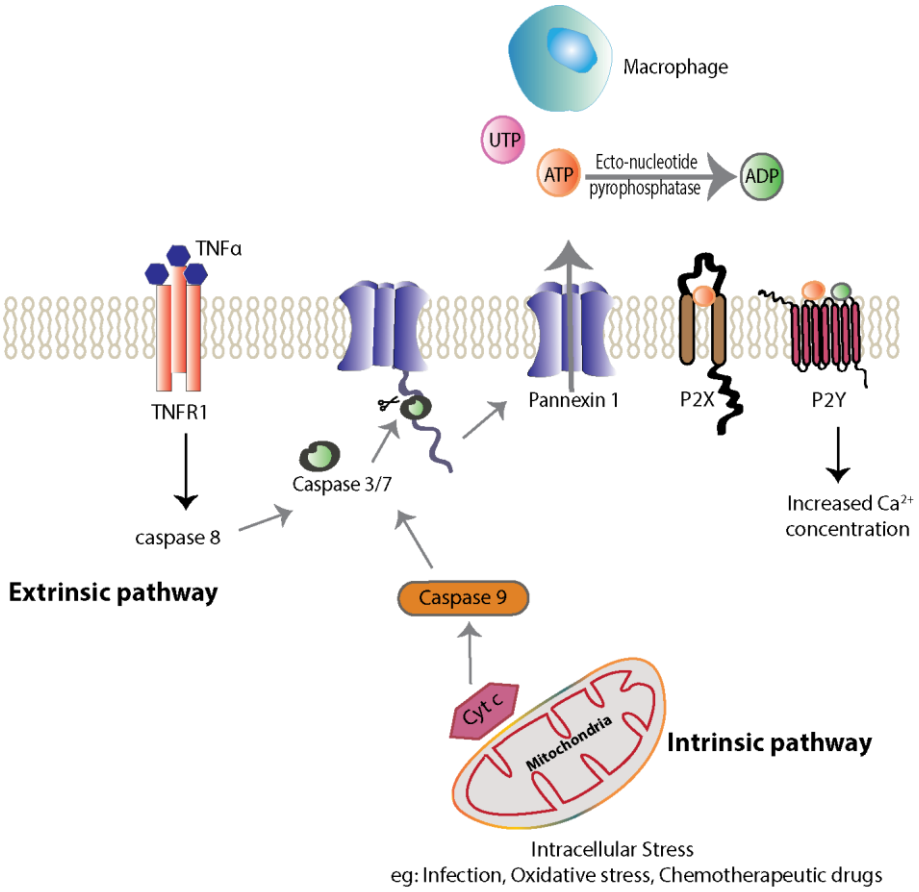

Fig. 1.4: Cleavage of PANX1 C-terminus during apoptosis leads to ATP release that acts as a signal for activating other purinergic receptors.

Cleavage of the C-terminus by caspase 3/7 leads to the constitutive activation of PANX1 and an increase in nucleotide release and phagocytic recruitment for the clearance of the cell[75]. PANX1 is also required in intrinsic and extrinsic apoptosis for NLRP3 inflammasome activation[60].

A detailed study on the PANX1 activation by C-terminus cleavage was done by Yu-Hsin Chiu *et al.* using wild-type and engineered concatemeric channels[77]. The authors observed an increase in the ATP/dye permeation and unitary conductance with successive C-terminal cleavage, suggesting C-terminus is a pore blocker. Ionic currents were observed after the removal of a single C-tail. In contrast, the permeation for larger molecules such as ATP and fluorescent dyes was observed only after removing two C-tails[77].

1.9 Post-translational modification in PANXs

After translation, eukaryotic membrane proteins undergo diverse post-translational modifications (PTM). Post-translational modifications alter the conformation of the protein affecting its functions positively or negatively. The three types of PTMs have been observed in the PANX family.

1.9.1 N-Glycosylation

All three members of the PANX family are N-glycosylated denoting attachment of an oligosaccharide to the protein at asparagine residue. The position and the role of glycosylation in PANX have been discussed in section 1.3.

1.9.2 S-nitrosylation

S-nitrosylation is defined as the addition of a nitrosyl group to a cysteine residue and is considered an important post-translational modification. A post-translation modification at this position might likely play an important role in regulating channel function.

A study by Stefanie Bunse *et al*. demonstrated intracellular cysteine's role. The authors mutated three intracellular cysteine residues to serine (C136S, C346S, and C426S). While there was no effect on PANX1 expression by C136S and C426S, mutation at position C346S led to early cell death in the oocyte. Moreover, the addition of CBX prolonged the oocyte death, revealing the role of C346 in oocyte survival. An

increased channel activity in C346S was also reported in oocytes measured by electrophysiology and dye transfer experiments[78].

Similarly, a study by Alexander Lohman *et al*. found that S-nitrosylation at Cys-40 and Cys-346 affects the channel activity by inhibiting PANX1 current and ATP release[79].

1.9.3 Phosphorylation

Phosphorylation is the covalent addition of phosphate group to amino acids performed by kinases. Phosphorylation is a reversible process where the phosphate group can be removed by phosphatases.

DeLalioa *et al.* studied the phosphorylation in PANX1, serine at 198 positions, in an intracellular loop and was observed to be constitutively phosphorylated in vascular smooth muscles. The phosphorylation is modulated by the activity of SRC kinase[80]. The authors also suggested the constitutive activation of PANX1 by phosphorylation, which can activate purinergic receptor signaling.

In PANX3, a study by Ishikawa *et al*., phosphorylation was observed at serine 68 by ATP/PI3/AKT signaling and is critical for osteoblast differentiation. They screened 17 phosphorylation sites, but a serine mutation to alanine at 68 position inhibited osteoblast differentiation via reduced olx and alkaline phosphatase[81].

1.10 PANXs role in health and disease

Due to its ubiquitous expression, PANX1 is linked to many diseases[82,83]. Apart from PANX1, its other isoforms are also linked to multiple diseases, which is not surprising given PANXs role in various physiological and pathological processes such as inflammation[84], apoptosis[85], wound healing[86], and bone differentiation[87].

Although PANXs are believed to release ATP as the major candidate, PANXs are non-selective channels and can pass various anionic or cationic molecules in different processes. However, tight regulation of PANXs is required for the cell's physiology. It is also interesting to note that PANXs expression can provide both protective and deleterious roles in the progression of the disease.

A list of a few diseases, along with the observation and the PANX isoform involved, is summarized in the table below.

Table 1.1: Role of PANXs in health and diseases.

Disease/condition	Observation	PANX	Reference(s)
Melanoma	PANX1 is up-regulated, and the knockout of PANX1 leads to a decrease in tumor progression.	PANX1	[88]
Epilepsy	Up-regulation of PANX1 in animal seizure models and patients with temporal lobe epilepsy.	PANX1	[89,90]
Ischemia	Protection in cultured neurons was provided in double knockout mice(PANX1 and PANX2)	PANX1/2	[91]
Multiple sclerosis	ATP released by PANX1 is involved in inflammatory processes, although it is unclear if the released ATP has a deleterious or protective role in multiple sclerosis.	PANX1	[92]
Diabetes	ATP released by PANX1 is required to fully activate insulin-stimulated glucose uptake in adipocytes.	PANX1	[49]
Hypertension	Inhibition of PANX1 by the hypertensive drug spironolactone reduced blood pressure in smooth muscles.	PANX1	[93]
Osteoarthritis	Up-regulation of PANX3 in cartilage degeneration in a mouse model.	PANX3	[87,94]
Duchenne's muscular dystrophy	Significantly low levels of PANX3 in the diseased mouse model compared to the healthy individual.	PANX3	[95]

1.11 PANX1 is a target for commonly used drugs

Gap junctions and PANXs do not share sequence similarities but possess similar topologies. Although both protein families play different roles in cells, they share

similar pharmacological properties. Interestingly, most gap junction blockers inhibit PANX1 function, including the most commonly used blocker for PANX1, carbenoxolone. Unlike gap junctions, PANXs can be inhibited by drugs that are commonly used and are specific targets of different proteins. A list of a few inhibitors of PANX1, along with their function, is stated below.

Table 1.2: Inhibitors of PANX1

Drug	Function	observation	Reference(s)
Tenofovir	Antiviral drug	Inhibition of PANX1 by tenofovir was observed to prevent liver and skin fibrosis by reducing adenosine levels.	[96]
Spironolactone	Hypertensive drug	Spironolactone inhibits PANX1 and reduces hypertension	[93]
Trovafloxacin	Broad spectrum antibiotic	Inhibition of PANX1 was observed during apoptosis	[97]
Probenecid	Gout medicine	Reduce morphine withdrawal symptoms by inhibiting PANX1.	[13,98]
Carbenoxolone	Anti-ulcer drug	Carbenoxolone has been observed to inhibit PANX1 in different cell types and processes and is the most common blocker used in PANX biology.	[99]
Mefloquine	Anti-malarial drug	Reduces morphine withdrawal symptoms by inhibiting PANX1.	[100]

Although there are multiple blockers for PANX1, the mechanism of inhibition of PANX1 by these drugs is still unknown. However, a detailed study was done by Michalski *et al.* to understand the putative binding residues for carbenoxolone. The authors made a series of extracellular loop mutants and measured the current's attenuation using a patch clamp[99]. Using this approach, the authors discovered that a non-aromatic mutation at W74 leads to a reversal of action polarity and is the primary residue

involved in inhibiting PANX1 by carbenoxolone. Moreover, they suggested the supporting role of other residues of the first extracellular loop in carbenoxolone binding.

1.12 PANX1 congenital mutant(R217H)

Although due to its ubiquitous expression, PANX1 has been linked to multiple diseases where it plays a protective or deleterious role, no congenital mutational conditional was reported until 2016, when Qing Shao *et al*. reported the first case of PANX1 congenital mutant where a 17-year-old female patient initially presented for genetic evaluation with multiple severe concerns such as including primary ovarian failure, intellectual disability, sensorineural hearing loss, and kyphosis. Psychological testing revealed both verbal comprehension index and perceptual reasoning indices of 45 (less than 2nd percentile) on the Wechsler Intelligence Scale for Children (WISC-IV), which is equivalent to the intelligence of a six-year-old.

Although she is independent with her basic activities but requires some help with batching, cooking, and oral care. Apart from this, she cannot count beyond 30 and mainly uses signs for communication[101]. A pedigree chart is shown below for a better understanding of the family's conditions.

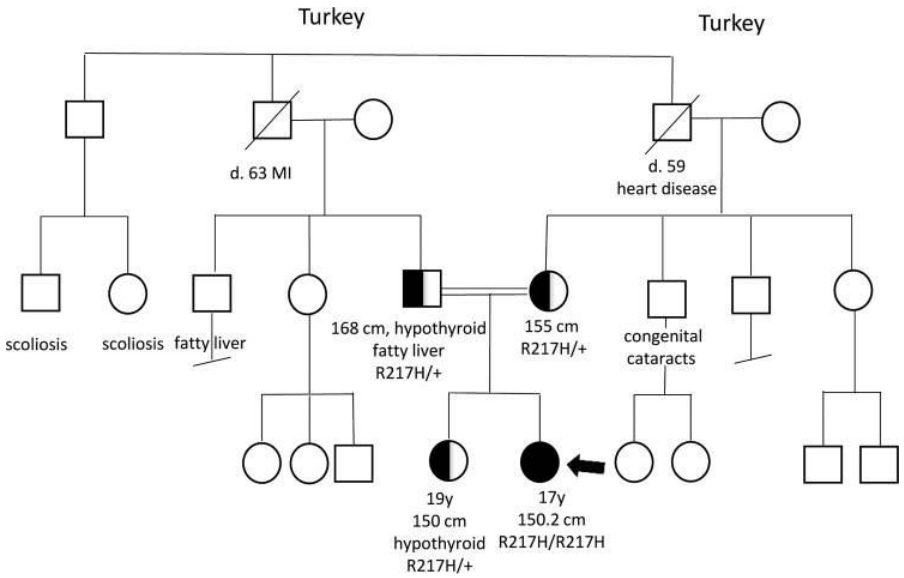

Fig. 1.5: Pedigree diagram displaying homozygosity for R217H in the patient[101]. The patient's parents are heterozygous for the mutation and do not show any symptoms.

The authors considered a possibility of a new genetic disorder given the complex phenotype of the patient and performed whole exome sequencing of the patient and her parents. A missense mutation R217H was seen in the family. Although the patient's parents and sister were heterozygous for the variant, the patient was homozygous. The mutation was confirmed by sanger sequencing.

To understand the cause of these severe conditions, the authors generated an R217H mutant. The expression of the congenital mutant in neuroblastoma and NRK cells reveal proper trafficking to the membrane $PANX1_{WT}$.

To understand the role of arginine and how the replacement of arginine to histidine affects the channel's activity, the authors performed electrophysiology recordings, EtBr uptake, and ATP release experiments of both wild-type and PANX1 congenital mutant.

The experimental finding suggests a partial loss of function in the mutant channel. While the expression of the mutant channel did not affect the morphology of different cells tested, a loss of 50% channel activity was observed in the mutant compared to the wild type. The authors concluded that the PANX1 mutant does not create toxicity in the cell, which will affect the cell's morphology but reduces the channel function leading to severe abnormalities in the patient.

Given the role of PANX1 in multiple processes and the activation of other proteins through ATP released by PANX1, it is safe to conclude that the PANX1 mutant might also be affecting other proteins[101].

A recent report by R Purohit *et al.* suggests that the mutational effect of the R217H germline variant depends on its interaction with the carboxy-terminal of the channel. They performed electrophysiology studies of the mutant with and without the C-terminus. The authors observed a decrease in the current when the C-terminus was intact. However, there was no effect on the mutant current when the C-terminus was cleaved off (386-426)[102].

1.13 Large pore channels

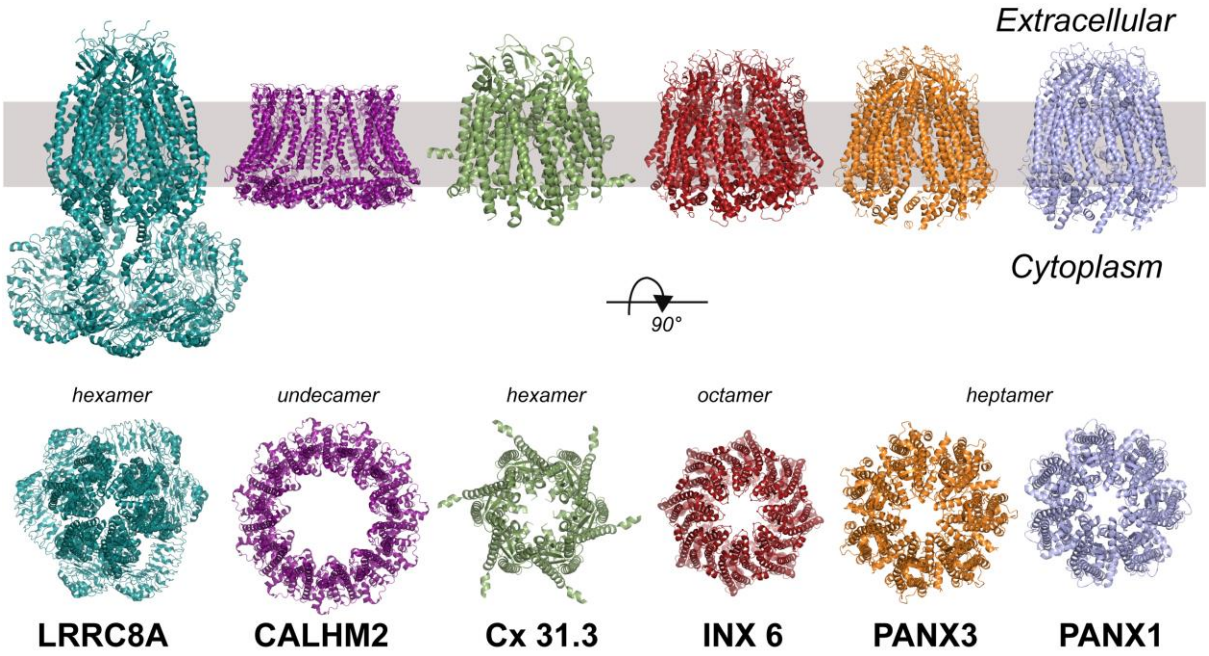

Fig. 1.8: large-pore channels, A Representative structure from different large-pore channel families showing the side (upper panels) and the top (lower panels) view from the membrane plane. For clarity, only one structure is shown. The PDB codes for LRRC8A, CALHM2, Cx31.3, INX6, PANX3 and PANX1 are 5ZSU, 6LMU, 6L3V, 6KFG, 8GTR and 6WBF respectively[103–106].

Large pore channels differ from canonical channels in selectivity and pore size. These channels are not highly selective and allow the passage of small and large molecules of different charges. The oldest large pore channels are Connexins gap junctions involved in the electrical synapse. Innexins are gap junctions present in invertebrates. Interestingly, Connexins and Innexins have been observed to form both hemichannels and gap junctions. The recently discovered large pore channels include LRRC8, CALHM, and PANX (Pannexin) family of proteins. PANX is the smallest family, with only three members.

LRRC8 belongs to the VRAC (Volume regulated anion channel) family of channels essential to regulate volume homeostasis in vertebrate cells by mediating chloride ions and organic osmolytes[107–109]. CALHM (calcium homeostasis modulator) family comprises six isoforms. They form non-selective channels and are speculated to release ATP and other large molecules. CALHM1 is the most characterized isoform

and is activated by depolarization and decreased extracellular Ca^{2+} concentration[39,103,110,111].

Although these channels vary greatly in their oligomeric assembly, they all have a large non-selective pore. They also share similar topologies and have four transmembrane helices in a subunit. CALHM, Connexins, and Pannexins have been speculated to release ATP from the cells. However, recent advances in the large pore channel field have concluded that Pannexin1 is the major conduit for ATP release.

The mechanism of channel opening and closing in these large pore channels remains elusive as different channel conformations have not been achieved yet.

1.14 PANX2

Pannexin2 (PANX2) is the largest family member of the PANX family. Although it has four transmembrane helices like PANX1 and 3, the C-terminus is comparatively larger (~300 amino acids) to PANX1 (~50 amino acids) and PANX3 (~20 amino acids). PANX2 has fairly ubiquitous expression and has been documented to express in the brain and skin. A study by Daniela Bossa *et al*. determined the location of endogenous PANX2 and heterologous expressed PANX2 in Hela, MDCK, and HEK293T cell lines[112]. PANX2 was localized in cytoplasmic compartments in both neurons and astrocytes. It was partially glycosylated as opposed to the other two isoforms localized on the plasma membrane, suggesting different trafficking routes for PANX2[112].

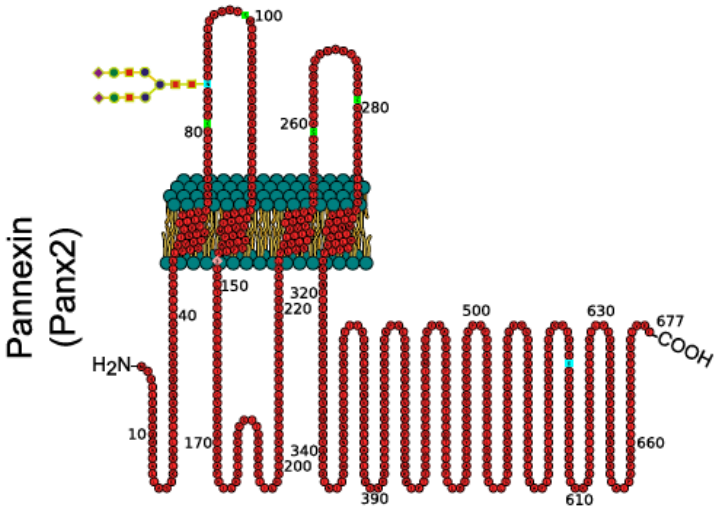

Fig. 1.6: PANX2 topology displaying a long C-terminus[113]. PANX2 shares a similar topology with the other PANX isoform but has a long C-terminus compared to PANX1 and 3.

Rafael E. Sanchez-Pupo *et al*. observed the expression of PANX2 in murine skin cells. They detected the expression of PANX2 in the suprabasal layer of the mouse epidermis and also observed up-regulation of PANX2 in vitro model of rat epidermal keratinocyte differentiation. Interestingly, PANX2 has been observed to cleave its C-terminus at the D416 position in apoptotic rat keratinocytes when exposed to UV-B to induce apoptosis without increasing the apoptotic rate measured by caspase3/7. Furthermore, the authors suggested the role of PANX2 in skin homeostasis[23]. The role of PANX2 in apoptosis is of further interest as a similar role of PANX1 has been observed.

Another study by C.P.K. Lai *et al*. examined human glioma cell lines using a western blot and showed a reduction or absence of PANX2. To understand the role of PANX2 in the growth of glioma cells, the authors explored the reduction in the growth of the glioma cells upon restoring PANX2 expression. They used a well-established cell line, rat C6 cells, and observed a flattened morphology in PANX2-expressing cells compared to PANX1-expressing cells. Moreover, they observed the PANX2-GFP signal from the cytoplasm and not from the plasma membrane suggesting PANX2 localizes in the cytoplasmic compartment and does not co-localize with PANX1 in the plasma membrane.

The authors also tested the effect of PANX2 on the oncogenicity in glioma cells using an anchorage-independent growth test. Anchorage-independent growth is a hallmark of cancer as they continue to grow without support. The test includes the growth of anchorage-dependent colonies on soft growth, which was reduced in the presence of PANX2.

They further examined the growth-suppressor role of PANX2 and observed significantly smaller tumors than the control[114]. These findings suggest a suppressive role of PANX2 in glioma tumor cells and can act as a therapeutic target.

1.15 PANX3

Pannexin3 (PANX3) has been reported to express in osteoprogenitors, osteoblasts, and chondrocytes[25,112]. PANX was found at the plasma membrane and also diffused

in the cytoplasm. An endoplasmic reticulum marker, calnexin, showed co-localized with PANX3 suggesting PANX3 is also localized in ER membranes and might perform various roles depending on its localization. A study by Masaki Ishikawa *et al.* demonstrated the role of PANX3 in osteoblast differentiation and metatarsal growth[115].

The authors reported that PANX3 mRNA was not detected in undifferentiated cells. However, when the cells were differentiated to osteoblast, the PANX3 expression was detected simultaneously with that of osteoblast induction marker genes such as Runx2, alkaline phosphatase, and osterix. They also observed that PANX3 expression promotes osteoblast differentiation by comparing it with different differentiation markers. To understand the role of PANX3 in the ex-vivo growth of metatarsals, the authors cultured metatarsals from newborn mice and infected them with PANX3. A comparison with the control indicated PANX3 promotes the growth of metatarsals. Like PANX1, PANX3 has been associated with ATP release activity[115]. Using caged luciferin, PANX3 expressed and control cells were imaged. A decrease in the intracellular ATP was observed after a few minutes compared to control cells indicating the role of PANX3 in ATP release.

Peipei Zhang *et al*. used panx3 $^{-/-}$ mice to understand the role of PANX3 in skin development. Panx3$^{-/-}$ mice exhibited thin epidermis and delayed hair follicle regeneration compared to the control mice. Panx3$^{-/-}$ also showed inhibition of keratinocytes differentiation and cell proliferation. The authors also provided evidence for keratinocyte differentiation by PANX3 is regulated by epiprofin via Akt/NFAT signaling pathways and acts as an upstream regulator of epiprofin[116].

PANX3 expression has been detected in odontoblast. Tsutomu Iwamoto *et al.* explored the role of PANX3 in odontoblast differentiation. The authors performed an ATP flux assay to quantitate the ATP release through PANX3 in pre-odontoblasts. A PANX3 blocking peptide was used as a blocker to inhibit PANX3 channel activity. The authors suggested that the decrease in the intracellular ATP by PANX3 activates the AMPK signaling pathway, which leads to the inhibition of cell proliferation by expression of p21[117].

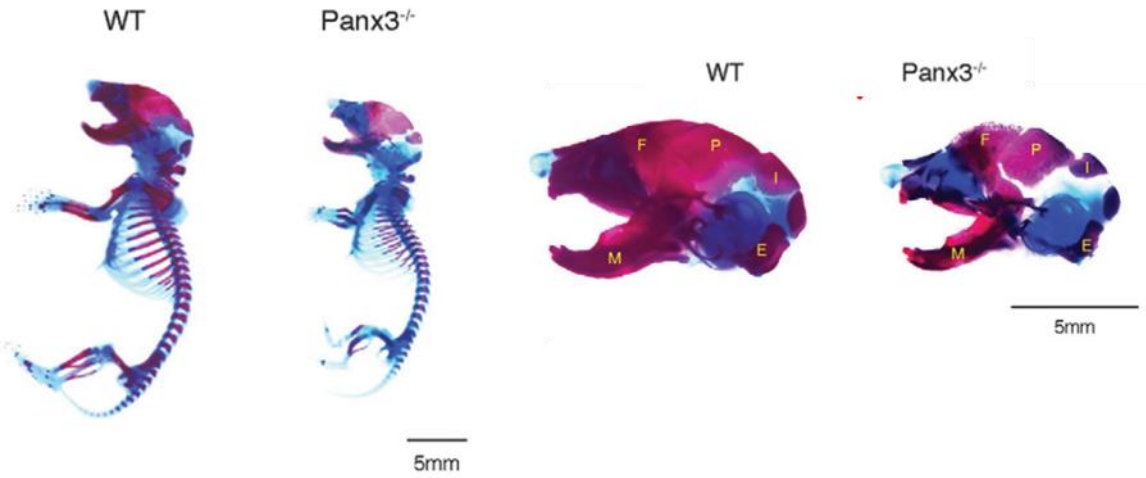

Fig. 1.7: PANX3 knockout mice exhibit skeletal abnormalities and stunted growth compared to PANX3 wild type[117].

Gap junction connexin43 and PANX3 are the two important wide pore proteins expressed in osteoblasts. Masaki Ishikawa *et al.* studied these proteins' functional and structural relationship in skeletal formation and development. The authors generated PANX3 null mice (Panx3-/-) an PANX3/connexin43 null mice (Panx3-/- Cx43-/-).

PANX3 null mice exhibited severe dwarfism and reduced bone density compared to the control mice. Panx3$^{-/-}$ Cx43$^{-/-}$ mice exhibited a phenotype similar to Panx3$^{-/-}$. Although the expression of chondrocytes and osteoblasts was increased in PANX3 null mice, their differentiation was inhibited. Moreover, PANX3 functions as an endoplasmic reticulum channel to release calcium, promoting differentiation. The authors suggested that PANX3 regulates differentiation by modulating Wnt/β-catenin signaling and regulating Osx[118].

PANX3 is the shortest of the three isoforms and has 41 % sequence identity to PANX1. PANX2 is the most divergent of the three, with a sequence identity of approximately 24% and a significantly longer C-terminus. Surprisingly, despite the sequence similarity of PANX isoforms, PANX1, PANX2, and PANX3 possess distinct residues at the channel pore, which likely account for their divergent behaviors.

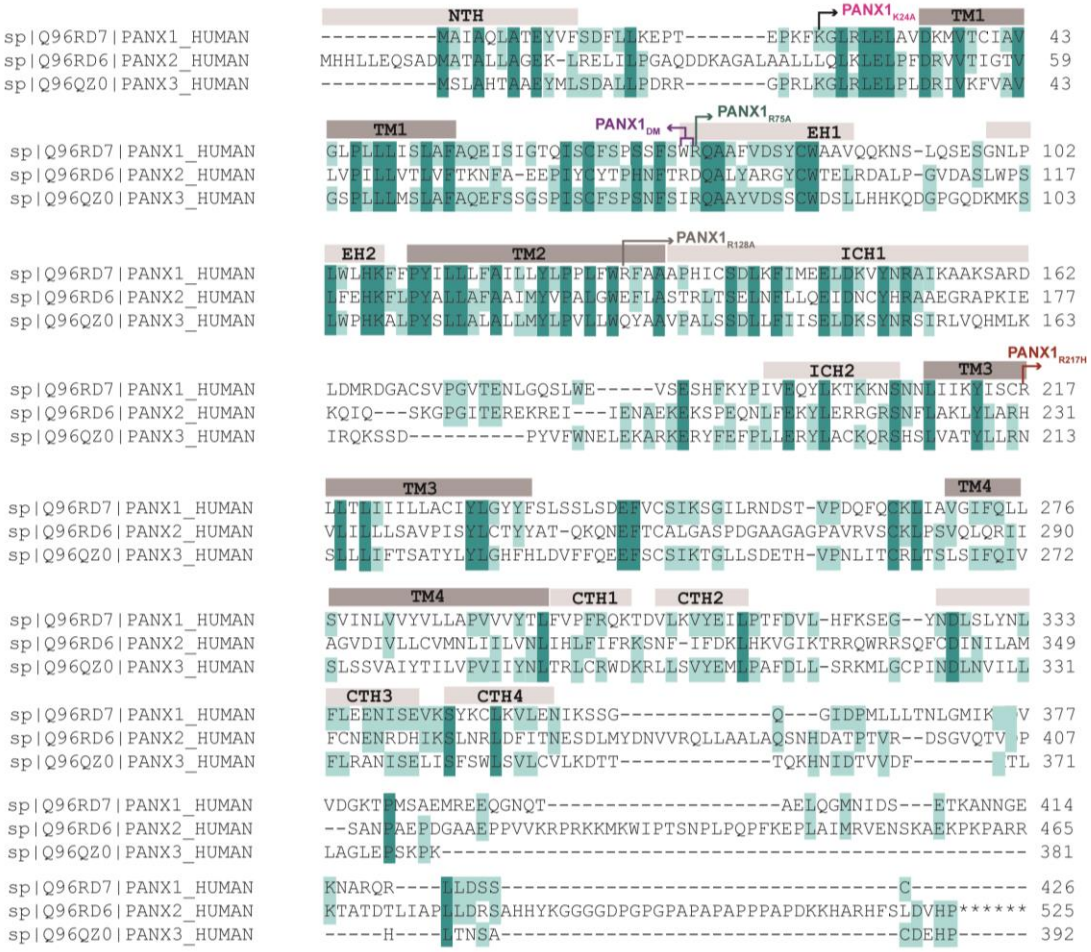

Fig. 1.8: Multiple sequence alignment of human PANX isoforms. The mutants studied are marked; $PANX1_{DM}$, PANX2 pore residues mimic, represents a double mutant (W74R, R75D). $PANX1_{R217H}$ is a congenital mutant, $PANX1_{K24A}$ is an N-terminus mutant, $PANX1_{R75A}$ is a pore mutant, and $PANX1_{R128A}$ is located at TM2.

In this study, we aim to determine the electron cryomicroscopy (Cryo-EM) structures of human Pannexin1 (PANX1) and its mutants to capture PANX1 in a different conformation. The congenital mutant has partial loss of function, suggesting that

PANX1 might be present in a different conformation owing to the mutation. This study aims to propose a mechanism for the loss of function in the PANX1 (R217H) mutant.

We also generated a PANX1 double mutant where the pore residues (W74 and R75) are replaced by PANX2 pore residues (R74, D75). The aim is to demonstrate the structural and functional effects of these substitutions on the PANX1 channel.

We also intend to determine the structure of PANX3, a PANX1 isoform, to understand oligomeric organization in the PANX family and deduce the structural and functional differences in PANX isoforms owing to their distinct localization and functions.

In order to highlight the effects of substitutions on the channel function among PANX isoforms, we further conducted our research focused on understanding the modification of channel properties by using electrophysiological measurements and ATP interactions.

CHAPTER 2

Materials and methods

2.1 Plasmid and cloning

Full-length genes of human *panx1* (UniprotID-Q96RD7) and *panx3* (UniprotID-Q96QZ0) were synthesized by Geneart (Invitrogen). Each gene was inserted into the pEG-Bacmam vector at EcoR1 and Not1 restriction sites using double digestion and ligation. Enhanced green fluorescence protein (eGFP) along with an 8X his tag was inserted at the C-terminus of the protein. To cleave GFP during the purification stage, a TEV protease site (ENLYFQS) was inserted between GFP and the C-terminus of the protein.

2.1.1 Generation of mutants

The mutants were generated using mega primer-based site-directed mutagenesis[119]. The mutants are generated in two steps. In the first step, the mega primer of flexible length(1-1.5 kb) is amplified using forward and reverse primers. For all the mutants, the forward primer was synthesized with the mutation, and the reverse primer was complementary to the wild-type sequence. The mega-primer amplification was visualized by EtBr fluorescence.

The amplified product from the excised gel was extracted from agarose gel using a purification kit by Favorgen. The purified mega primer (containing mutation) was used as a primer for the whole plasmid amplification. Prior to the transformation of plasmid in *E.coli* Top10 cells, methylated parent/template DNA was digested by Dpn1 (0.5 µl of Dpn1 was used for 20 µl of reaction for 4-6 hours at 37℃).

The newly amplified whole plasmid was transformed into *E.coli* Top10 competent cells using a standard transformation protocol.

The transformed cells were plated on Luria broth-Agar (LB-agar) plate for 13-15 hours. The transformed colonies were picked and inoculated in ampicillin antibiotic-containing LB media. The plasmid was extracted from the culture using a plasmid extraction kit from favorgen, and the mutation was confirmed by Sanger sequencing.

2.2 Constructs used in the study

Table 2.1: Constructs used in the study

List of mutants	Abbreviation	Description
PANX1-WT	PANX1/PANX1$_{WT}$	Full-length human PANX1
K24	PANX1$_{K24A}$	Lysine to alanine mutation at 24 position (N-terminus) in full-length human PANX1
W74R/R75D	PANX1$_{DM}$	Tryptophan to arginine at 74 position and arginine to aspartate at 75 position in full-length human PANX1
R128A	PANX1$_{R128A}$	Arginine to alanine mutation at 128 position (TM2) in full-length human PANX1
R75A	PANX1$_{R75A}$	Arginine to alanine mutation at 75 position(pore) in full-length human PANX1
R217H	PANX1R127H	Arginine to alanine mutation at 217 position (TM3) in full-length human PANX1
PANX3-WT	PANX3	Full-length human PANX1

2.3 Small-scale transfection

HEK293S GnTI$^-$ (ATCC- CRL-3022) cells were seeded at a density of 1*10^6 cells in DMEM media supplemented with 10 % FBS (Foetal Bovine Serum). The cells were allowed to adhere for 12-16 hours in the incubator (5 % CO_2, 80-90 % humidity, 37 ℃). Lipofectamine 3000 was used as a transfection reagent, and the transfection was performed according to the manufacturer's protocol. Transfection efficiency was qualitatively analyzed by fluorescence microscope by visualizing eGFP fluorescence.

2.4 Fluorescence-detection size exclusion chromatography (FSEC)

FSEC is a fluorescence-based chromatography that utilizes the fluorescence property of eGFP or other fluorescent tags[120]. It is an efficient strategy where the protein is covalently linked to the eGFP enabling the screening of the desired GFP-tagged protein in a crude solubilized cell sample of other proteins without purifying it[120]. For

FSEC, the transfected cells were harvested after 36-40 hours of transfection, solubilized in 25 mM Tris pH 8.0, 100 mM KCl, 1% glycerol, and 10 mM glycodiosgenin (GDN), buffer. The solubilized cells were spun down at 66,000 for one hour to remove the cell debris and the insolubilized membranes. Post centrifugation, the supernatant was loaded on a superose6 increase 10/300 GL column. To screen the monodispersity and the quality of the protein, GFP fluorescence was monitored (λ_{Ex}= 488 nm, λ_{Em}= 509 nm).

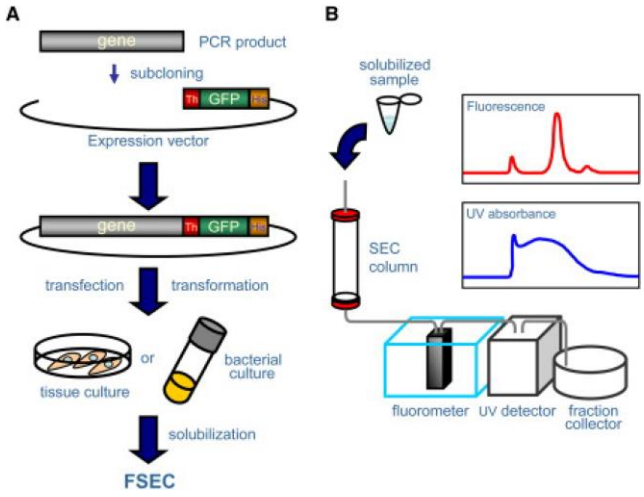

Fig. 2.1: Flowchart of screening GFP-tagged proteins through FSEC. The gene of interest is tagged with a GFP, and the GFP fluorescence is monitored to check the quality of the protein[120].

One of the major advantages of FSEC is the requirement of a very small quantity of protein(~ng). Also, the expression level of the tagged protein can be quantified without purifying the protein.

2.5 Detergent Screening

Membrane proteins contain hydrophobic transmembrane domains and hydrophilic cytoplasmic or extracellular domains. The transmembrane region is embedded in the membrane bilayer. To purify the membrane proteins, they are first solubilized and then purified in the presence of a detergent. The purified membrane proteins are a protein-detergent complex where the transmembrane region is covered by an amphipathic detergent molecule, making them soluble in the buffer[121,122].

Thus, it is critical to select a suitable detergent for the optimal purification of the protein[123]. Multiple detergents were screened using FSEC. The cells were transfected as described earlier, and the transfected cells were solubilized in different detergents. The solubilized crude lysate was loaded on a superose6 10/300 GL column. GFP fluorescence was monitored, and the FSEC profile (aggregation, homogeneity, elution volume) was compared for different detergents. After selecting the detergent, the protein was purified on a large scale. For the large-scale expression and purification, we employed the Bacmam system[124,125].

2.6 Baculovirus transduction of mammalian cells (Bacmam)

Hofmann *et al.*[126] and Boyce & Bucher[127] reported the first evidence of transduction of recombinant baculovirus in mammalian cells. Due to its high gene delivery efficiency, non-replicative nature in mammalian cells, low toxicity, and ease of creating the virus, the Bacmam system has become a safe, economical, and convenient technique for large-scale mammalian membrane protein expression.

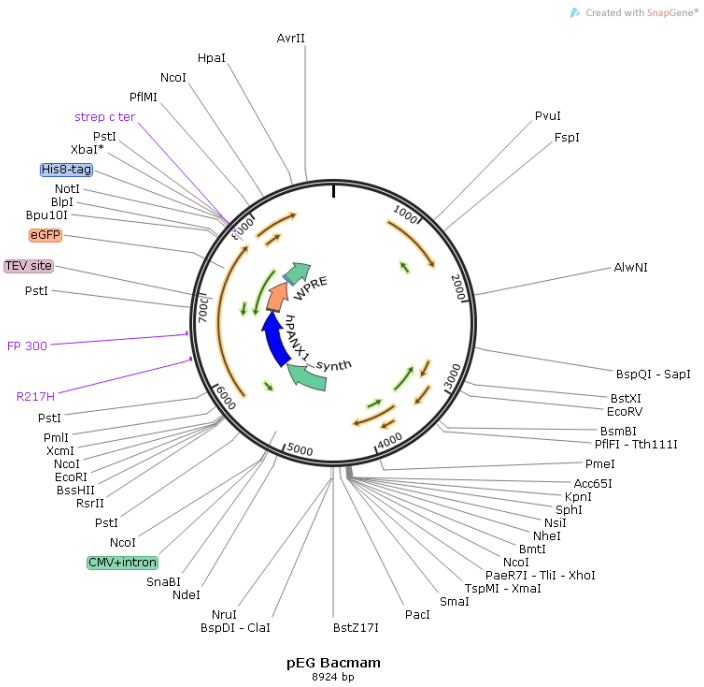

Fig. 2.2: Map of the pEG-Bacmam vector with human PANX1 with a C-terminal GFP and an 8x his tag.

The pEG-Bacmam vector contains a strong CMV promoter for robust transcription. The intron is used for efficient RNA splicing and RNA processing, and the WPRE

element is required for mRNA processing, export, and stability[125]. These synthetic elements were derived from a vector pVLAD[128]. To generate the pEG-Bacmam vector, these synthetic elements were incorporated into the pFBDM vector that allows the assembly of multiple expression cassettes[129]. SV40 poly-A late signal is required for the termination of transcription, and p10 and polh are the promoters for the baculovirus amplification and insect cell expression.

2.7 Bacmid Generation

2.7.1 Transformation

E.coli DH10Bac cells harbor two plasmids for the efficient generation of recombinant bacmid. The helper primer(pMON7142) is tetracycline-resistant, and the shuttle vector(bMON14272) is kanamycin resistant. These plasmids support the process of site-specific recombination between pEG-Bacmam and the shuttle vector. The recombinant bacmid can be isolated for transfection in insect cells to generate baculovirus. The recombinant bacmids are picked based on blue-white screening. Blue-white screening depends on the activity of the β-galactosidase enzyme, which converts lactose into galactose and glucose. For screening, X-gal, a chromogenic substance, is used that can be hydrolyzed by β-galactosidase enzyme 5-Bromo 4-chloro indoxyl, which dimerizes to form a blue pigment called 5,5'-dibromo-4,4'-dichloro-indigo. The insertion in the lacZ gene leads to the inactivation of the enzyme resulting in white recombinant colonies.

The pEG-Bacmam vector(20ng) was transformed using a standard protocol in *E.coli* DH10Bac competent cells. The transformed cells were given a recovery of four hours in fresh 500 µl of Luria broth (LB) without antibiotics. Post recovery, the transformed cells were plated on antibiotics and X-gal containing [(gentamycin(7ug/ml), kanamycin(50ug/ml), tetracycline(10ug/ml), IPTG (40ug/ml), Blue gal/ X-gal (300ug/ml)] LB-Agar plates. The plates were incubated for 36-40 hours, and the recombinant white colonies were picked for inoculation[130,131,132].

2.7.2 Inoculation

Few white colonies (containing recombinant bacmid) were picked and inoculated in antibiotics [(gentamycin (7 ug/ml), kanamycin (50 ug/ml), tetracycline (10 ug/ml)]

containing LB media. The cells were kept at 37° C and 180 rpm for 14-16 hours in a shaking bacterial incubator, and the recombinant bacmids were isolated from the cells.

2.7.3 Bacmid Isolation

Cells containing recombinant bacmids were pelleted down at 5000 rpm for 15 minutes. The pellet was then resuspended in 200 µl of resuspending buffer (Favorgen). The pellet was vortexed for efficient resuspension. The resuspended pellet was transferred to a fresh 1.5 ml MCT (Micro Centrifuge Tube). The cells were lysed using a lysis buffer(200 µl). For better lysis, MCT was inverted 3-4 times, and pipetting, and vertexing was not used to avoid shearing the bacmid. Post lysis, 200µl of neutralizing buffer was added. The mixture was spun down at max speed(18000 g) for 10 minutes to remove the debris. The clear supernatant was collected in a fresh 1.5 ml MCT without disturbing the pellet; 600 µl of isoamyl alcohol (pH=8) was added and was mixed with the supernatant by inverting the MCT. The mixture was spun down at 18000 g for 2 minutes. The clear supernatant was transferred without taking the interface in a fresh 1.5 ml MCT, 1.2 ml of isopropanol was added to the supernatant, and a vortex was used for efficient mixing.

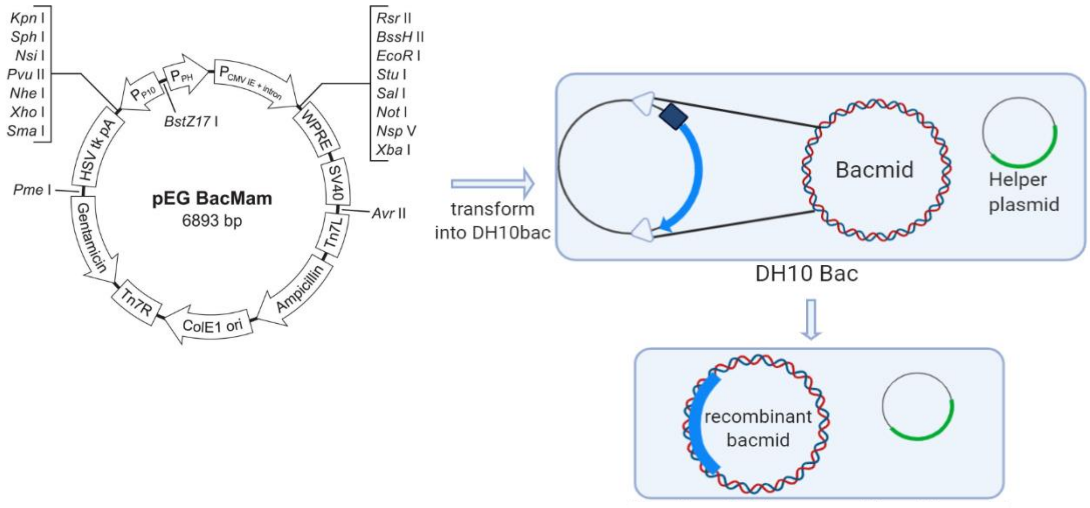

Fig. 2.3: Schematics of the process involved in the formation of a recombinant bacmid. The recombinant bacmid is selected based on blue-white screening, where white recombinant colonies are used for bacmid isolation[125].

The MCT was kept at -20 ℃ for 30 minutes. After 30 minutes, it was spun down at 18000 g for 30 minutes at 4 ℃. Post centrifugation, the supernatant was discarded, and the pellet was washed with 1 ml of 80 % ethanol. The solution was spun down at 18000 g for 5 minutes at room temperature. The supernatant was discarded, and the pellet was kept overnight for drying. The dried pellet was resuspended in 30 ml of autoclaved MQ water before transfection.

2.8 Generation of virus

Materials Required: Cellfectin (5 ul for one reaction), Sf9 cells (2 million/ml), Sf9 media, bacmids. For small-scale transfections, cells were seeded at ~0.8*10^6 per well in a six-well dish and were allowed to adhere for ~2 hours. Meanwhile, the transfection mix(cellfectin(5 ul) + media(95 ul) + bacmids(10 ug) was prepared. The transfection mix was incubated for ~1 hour. (Bacmids were mixed by tapping gently to avoid shearing, pipetting should be avoided). Before transfection, the old media in the dish was replaced by 2 ml/well of fresh media. The transfection mix was added dropwise and was incubated at 27 ºC for ~ 4 days.

As the constructs are eGFP tagged, GFP fluorescence was checked through a fluorescence microscope to check the transfection efficiency. (The green cells imply the presence of the P1 virus). The P1 virus was filtered through a 0.22 µm filter and harvested. The titers of the virus were improved by generating P2/P3 generation of the virus. Sf9 cells in suspension at a cell count of 2x10^6 cells per ml were infected for the generation of the P2 virus. Four days after the infection, cells were spun down at 7000 g, and the supernatant was filtered and stored at 4℃, protected from the light.

2.9 Large-scale protein isolation and purification

High titer virus was added to HEK293 GntI$^-$ cells at a density of 2.5-3*10^6 cells/ml in a ratio of 1:40 (virus: cells). Twelve hours post-transfection, sodium butyrate was added at a final concentration of 5 mM, and the temperature was reduced to 32 ℃. Cells were harvested after 55-60 hours post-infection at 5000 rpm for 30 minutes. The pellet was resuspended in a resuspension buffer and sonicated for 15 minutes at 35% amplitude (3s on and 5s off cycle).

The sonicated cells were spun down at 7000 g for 15 minutes to remove the cell debris.

The supernatant (sonicated cells) was centrifuged at 100,000 g for 90 minutes using a Backman rotor (Ti50.2/SW32). Post centrifugation, the supernatant was discarded, and the membranes were flash-frozen in liquid nitrogen and kept at -80 ℃ till further use.

For solubilization, membranes were thawed at 4 ℃ and homogenized in buffer using a Dounce homogenizer. The membranes were solubilized in the presence of a solubilization buffer (Tris pH 8.0, 100 mM KCl, 10 mM GDN, 0.1 % PMSF) for two hours at 4 ℃ on end-to-end rotation. The solubilized membranes were spun down at 100,000 g for 90 minutes. Meanwhile, Ni-NTA beads were equilibrated with the detergent buffer. Post centrifugation, the supernatant was added to the pre-equilibrated Ni-NTA beads and was kept for binding on end-to-end rotation at 4 ℃ for two hours. The protein bound to Ni-NTA resin was passed into a 24 ml Biorad column. The Ni-NTA resins were washed with the wash buffer(Tris pH 8.0, 100 mM KCl, 100 µM GDN, 1 % glycerol, 0.1 % PMSF) (50x bead volume) to remove the impurity. The protein was eluted in a 5x2 ml fraction in elution buffer (wash buffer+ 0.25 M imidazole). The eluted protein was kept for GFP cleavage for 12-16 hours at 18 ℃ using tev protease.

The protein was further purified by SEC (size exclusion chromatography) in the purification buffer (Tris pH 8.0, 100 mM KCl, 50 µM GDN, 1 % glycerol), during which the cleaved GFP was also removed.

2.10 Grid freezing and data collection

The SEC purified protein was concentrated using a 100 KDa cut-off concentrator at 7000 g. Before grid freezing, the concentrated protein was centrifuged at 66,000 g for one hour.

Quantifoil 300 mesh gold holey carbon grids (R1.2/1.3) were glow discharged in the air for 60 seconds at 25 mA, and 3 µl of purified protein was loaded on a grid in FEI vitrobot. The temperature and humidity of the vitrobot were kept at 16 ℃ and 100 %, respectively. Post-sample application, the grids were blotted to create a thin film. A duration of 3.5 seconds was optimized for PANXs (the grids had the optimal thickness and particle distribution). During blotting, the pipetted protein on the grid is blotted by the filter papers surrounding it.

The more the blotting time, the thinner the ice was. An image showing the blotting process is given below[133] (Fig: 2.4).

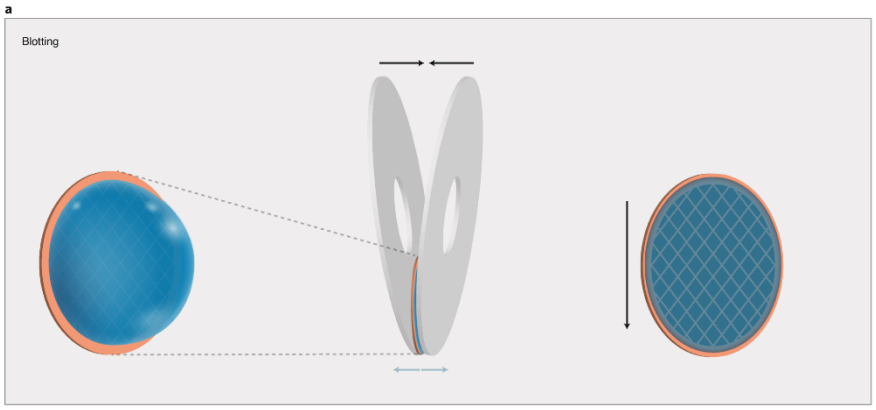

Fig. 2.4: Illustration of the blotting process. A small quantity of protein (3 µl) is put on the grid, and the excess protein is blotted for an optimized time with the help of filter papers. The blotted grid is then plunged frozen into liquid ethane[133].

The blotted time is optimized according to the sample, as the air-water interface can affect the sample behavior during the exposure. The grids can be blotted once or multiple times depending on the protein concentration and quality. In this study, we have used double blotting for $PANX1_{R217H}$.

For double blotting of dilute samples, the grids were blotted sequentially. The first blot was done for 2 seconds, and the second blot was done for 3.5 seconds. The wait time in both cases was 10 seconds. The grids were flash-frozen in liquid ethane and were stored in liquid nitrogen till further use.

For PANX3 grid freezing, ATP (final concentration 1 mM) was added 30 minutes before grid freezing.

Data acquisition was performed on Titan Krios 300 keV (Thermofisher) equipped with K2 or Falcon3 direct electron detectors. $PANX1_{WT}$ and $PANX1_{DM}$ data acquisition were done with Falcon 3 detector at a magnification of 75,000x and a pixel size of 1.07 Å. For $PANX1_{R217H}$ and PANX3 constructs, data was acquired on the K2 detector in EFTEM mode with a Bioquantum energy filter and a slit width of 20 eV at a magnification of 130,000x and pixel size of 1.07 for $PANX1_{R217H}$ and1.065 for PANX3. The total electron dose and the number of movies and frames for different constructs are mentioned in the table (Table 3.3, 4.3, 4.4, 5.1)

2.11 Single Particle Cryo-EM data processing

Multiple PANXs structures in this thesis were determined using the CryoSPARC version (3.20)[134]. Single particle Cryo-EM data processing involves multiple steps. This section includes a brief introduction for every step involved in the data processing.

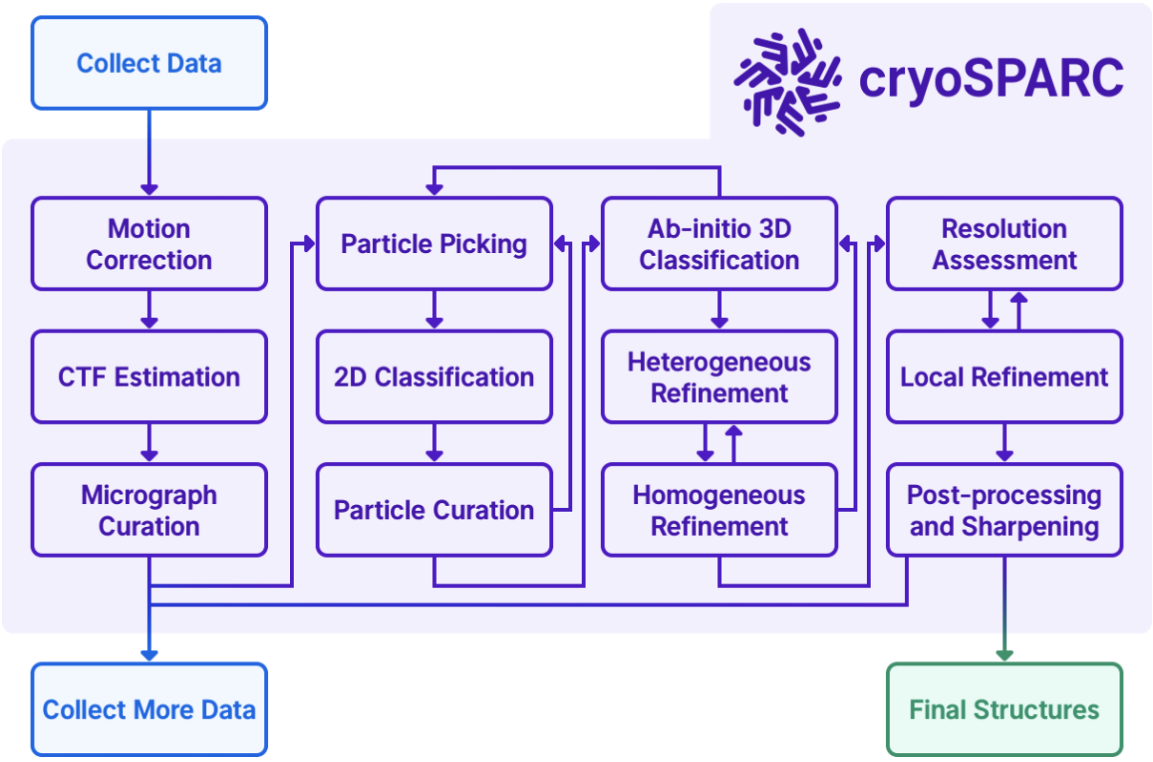

Fig. 2.5: Cryo-EM data processing workflow in CryoSPARC consists of multiple iterative processes to obtain a higher resolution structure[135].

2.11.1 Step1: Create a project and a workspace

The first step is to create a project for data processing. A project can have multiple workspaces. A separate project was created for every construct.

2.11.2 Step2: Import Movies

Once the project and the workspace were created, the movies were imported into the workspace through the job builder. Job builder displays all the available jobs that can be performed on a particular dataset. A few parameters, such as pixel size, total electron dose, accelerating voltage, and spherical aberration of the microscope, are required.

2.11.3 Step3: Motion correction

Once the movies are imported, they are converted into a single-frame micrograph. During ing the data collection, the movement in the sample can occur due to the movement of the stage (stage drift) or because of the electron beam(anisotropic deformation). In this study, we used patch motion correction, which corrects for stage drift and anisotropic deformation. The imported movies in the previous job can serve as the input for the motion correction job.

2.11.4 Step4: CTF (Contrast Transfer Function) Estimation

Contrast Transfer Function (CTF) can be defined as the relationship between the lens aberrations and the contrast in an image. It is the Fourier Transform function of the point spread function of an objective lens and causes signal delocalization in real space[136]. The samples are frozen in ice during Cryo-EM grid freezing. The electrons are passed through the sample, but the sample is not more opaque than its surrounding, leading to very low contrast. To circumvent this issue, the microscope is operated in phase contrast mode by defocusing it, where electrons interacting with the molecule/sample change their path, thus creating the contrast. When the electrons interact with the sample, they can scatter elastically (the electrons have their initial energy intact) or inelastically (A part of the energy of the electron is dissipated). Only the elastically scattered electrons are useful for generating phase contrast and particle images.

The electrons can scatter at different angles depending on how they interact with the sample. Due to this, the electrons follow different paths while reaching the electron detector. The interaction between the scattered and un-scattered electrons can be destructive, constructive, or inverting, resulting in some spatial frequencies showing up more strongly than others.

The CTF model used in CryoSPARC is given by,

$$\mathrm{CTF} = -\cos\left(\pi \Delta z \lambda_e f^2 - \frac{\pi}{2} C_s \lambda_e^3 f^4 + \phi\right)$$

Where Δz is defocus, λe is the wavelength of the incident electrons, Cs is spherical aberration, f is spatial frequency, and ϕ represents a phase shift factor.

The contrast in an image is mainly affected by the defocus. Thus, It is critical to estimate and correct the contrast transfer function during data processing to achieve higher resolution.

2.11.5 Step5: Manual Curation

The CTF estimated images can now be served as the input for manual curation, which involves the removal of bad micrographs to get high-quality particles. The major factors to look for are ice thickness and CTF estimation resolution, and high-defocus images can be removed at this stage (higher defocus contains low-resolution signal)

2.11.6 Step5: Particle picking (Manual picking/Auto-picking)

Once the manual curation is done, the manually curated set can be used for particle picking. In this study, the particles were picked by a blob picker. This job can be done iteratively to refine the particle data set. An approximate molecule dimension is required for the blob picker to pick particles from the micrograph.

2.11.7 Step6: Particle Extraction

The next step is to extract the particles from the micrograph. The box extraction is required for the job to run. It is recommended that the box size is kept large, as a larger box size captures most of the high-resolution signal, which is spread out spatially because of the defocus of the microscope[137]. Although the larger box size is computationally extensive. Thus, a balance between the computational resource and the signal capture is needed[137].

2.11.8 Step7:2D Classification

The extracted particles can now be grouped based on their 2D views. 2D classification gives an idea of the orientation or views present in the dataset. It can also give some insights into the heterogeneity in the sample.

2.11.9 Step8: Select 2D Classes

The 2D classes that resemble the molecules in different views are selected, and the junk (broken particles) are discarded to generate a 3D model. The selected 2D classes can again be divided into more classes to get a cleaner dataset of 2D classes.

2.11.10 Step10: 3D Ab-initio 3D reconstruction

Ab-initio modeling involves reconstructing one or more 3D reconstructions from the selected particles. Ab-initio reconstruction does not work if 2D views are insufficient to generate the complete model, which can happen if the molecule has an orientation bias.

For the generation of the ab-initio model, CryoSPARC utilizes two algorithms, Stochastic descent gradient (SGD) and branch and bound maximum likelihood optimization algorithm, which enables the reconstruction of a 3D model without the need for an initial model. SGD enables the convergence to a low-resolution model from random initialization, and the branch and bound algorithm accelerate the search for parameters that best align the 2D classes to a 3D map[134].

2.11.11 Step11: Refinement (Non-Uniform refinement) of selected ab-initio reconstruction

To achieve a higher resolution structure, selected low-resolution ab-initio 3D reconstruction is refined through non-uniform refinement[138]. Non-uniform refinement is an algorithm specially designed to account for the molecule's variability, such as membrane proteins. Membrane proteins are isolated as a detergent/membrane protein complex or nanodisc/membrane protein complex.

The detergents and lipids are locally disordered, which does not allow the membrane proteins to achieve higher resolution through traditional refinement processes (homogenous/heterogenous refinement). The existing refinement methods assume rigidity in the molecule. In contrast, non-uniform refinement is based on a cross-validation optimization algorithm that removes the variable region's noise while keeping the signal required for the particle alignment, thus increasing the resolution.

The high-resolution 3D reconstruction can now be used for model building.

2.12 Model building and refinement

$PANX1_{WT}$ was modeled using a previously determined structure (PDB-ID-6WBF) and refined in Phenix. For PANX1 mutants, the mutation was introduced in $PANX1_{WT}$ (PDB-ID-6WBF) in Coot, and the resulting mutant model was refined in Phenix using Cryo-EM 3D reconstruction.

For modeling PANX3, an Alphafold2[139,140] monomer was fitted in the map in Chimera[141] to form a heptamer. The fitted model and the 3D Cryo-EM map were aligned using autodock in Phenix[142]. The docked model was then fitted in the density in coot[143] and was refined in Phenix. In PANX3, POPE lipids were modeled using a three-letter code in coot and fitted manually in the density. The lipids were refined with the PANX3 model in Phenix. All the structures were refined using PHENIX real-space refinement, and the default refinement settings were used. Cryo-EM comprehensive validation in Phenix was used to validate the model.

2.13 Binding studies using ATP-γS (Microscale Thermophoresis (MST)

Microscale thermophoresis (MST) was used for binding studies. MST is a powerful technique for measuring biomolecular interaction without immobilizing the molecule. MST has two significant components, IR laser and excitation light. The IR laser creates a microscopic temperature gradient, whereas the fluorescent-tagged molecule is excited by the excitation light[144].

The movement of the molecules by the temperature is detected and quantified by a change in the fluorescence of the tagged molecule. MST can detect the changes in molecular hydration shell, size, or charge.

For the binding studies of ATP-γS with PANX wild type and the mutants, the protein concentration of 10 nM (calculated for the heptamer) was kept constant. The protein was labeled Tris Pico dye in a 1:1 ratio (protein: dye). Monolith standard capillaries were used for the binding studies. A non-hydrolyzable ATP analog, ATP-γS, dissolved in SEC buffer (25mM Tris pH 8.0, 100mM KCl, 100 µM GDN,1% glycerol) was used as a ligand for the binding studies.

The ligand concentration was diluted over 16 serial dilutions, keeping 2 mM (final concentration) of the ligand as the highest concentration. The ligand and the protein were mixed in a 1:1 volume ratio. The final protein concentration was calculated to be 10 nM. All the experiments were done in triplicates. The protein was purified once, and three independent MST runs were done.

2.14 Electrophysiology

For the electrophysiology recordings, HEK293 cells were maintained in DMEM F-12 Ham medium, and the media was supplemented with 10% FBS (Foetal Bovine serum) and 1% antibiotic-antimycotic solution in the incubator. The incubator settings were kept constant at 5% CO_2 and 37℃. The cells were maintained in a healthy state by passaging them twice a week. For the experiments, cells were seeded at a density of 0.4-0.6*10^6 cells in a 35 mm cell culture dish.

All PANXs were transiently co-transfected in HEK293 cells with an enhanced green fluorescent protein(eGFP) using Lipofectamine 2000 transfection reagent. The transfection was performed according to the manufacturer's protocol. After 24-36 hours post-transfection, the cells were visualized under a fluorescent microscope, and the green cells(cells expressing GFP) were selected for patch clamp electrophysiological recordings. PANX currents were recorded in whole-cell mode using an EPC 800 amplifier (HEKA Elektronik), Digidata 1440A digitizer (Molecular Devices), and pClamp 10 software.

To elicit the currents, 400 ms voltage clamp steps were applied from a holding potential of - 60 mV to test potentials of -120 to +120 mV in 10 mV increments. The currents were sampled at 20 kHz, and digitally low pass (Bessel) was filtered at 3 kHz. The patch electrodes used for electrophysiology experiments were fabricated using borosilicate glass capillaries and had a resistance of 3-5 MΩ when filled with an internal solution.

The pipette solution(internal solution) contained in mM) 150 Cesium gluconate, 2 MgCl2.6H2O, and 10 HEPES (pH adjusted to 7.4 with NaOH). The extracellular solution contained (in mM) 147 NaCl, 2 KCl, 1 MgCl2.6H2O, 2 CaCl2.2H2O, 10 HEPES, 13 Glucose (pH adjusted to 7.4 with CsOH)15. Carbenoxolone (Sigma) was used as a blocker. Its effects were evaluated at a final bath concentration of 100 µM by adding a bolus from a stock solution prepared by dissolving it in milli-Q water. The experiments were performed at room temperature (23°C). Electrophysiological data were analyzed using Clampfit, Microsoft Excel, and Graphpad Prism. The current-voltage relationships were plotted as normalized steady-state current values at the end of the pulse step (at 400 ms) versus the respective voltage step (mV). Current densities (pA/pF) were obtained by dividing the steady-state current values(pA) by the

cell membrane capacitance (pF). The conductance voltage relationship was plotted to analyze the voltage dependence of channel activation.

The conductance (G) was calculated using I=G(Vt-Vrev), where I is the steady state current value at the test potential Vt, and Vrev is the reversal potential. The conductance voltage plot was fitted to a Boltzmann equation: I=Imax/1+exp((Vt-Vh)/k)) where Imax is the maximum steady state current amplitude, Vh is half maximal voltage for activation(V50), and k is the slope factor. A two-tailed unpaired t-test is used for calculating the significance, ***$p < 0.001$; n.s., not significant.

CHAPTER 3

Structural and functional characterization of human $PANX1_{WT}$

3.1 Introduction

Pannexins (PANXs) are large-pore vertebrate channels identified through limited sequence similarity with invertebrate gap junctions, innexins[7]. PANX family constitutes of three members, with PANX1 being ubiquitously expressed and the more extensively studied isoform[7,8]. PANX1 channel is involved in many cellular and physiological processes, including apoptosis, viral replication, and cell migration, primarily through its ATP release activity[64,145].

PANX1 has been observed to elicit currents at positive voltages[53]. Although PANX1 can be activated by voltage, it is not a predominant mechanism of channel opening. Cleavage of PANX1 C-terminal tail by caspase, high extracellular potassium, and mechanical stress has been reported to activate PANX1 channels[77,146].

In this study, we determined the structure of full-length $PANX1_{WT}$ through Cryo-EM at a resolution of 3.75 Å. We also delved into its activation through positive voltages by whole cell patch clamp recordings and presented the experimental evidence of ATP binding.

3.2 Ortholog screening of $PANX1_{WT}$

hPANX1(human PANX1) and rPANX1(rat PANX1) genes were synthesized by Geneart (Invitrogen) and were cloned into the pEGBacmam vector with a TEV protease site and C-terminal GFP fusion. The quality of the heterologously expressed protein was assessed by FSEC by monitoring GFP fluorescence.

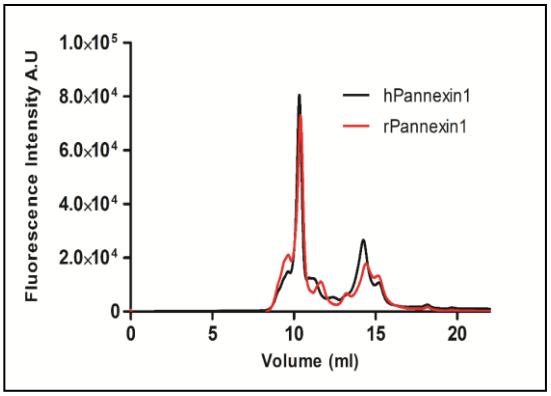

Fig. 3.1: Fluorescence size exclusion chromatography (FSEC) profile for PANX1 orthologs (human PANX1 and rat PANX1). The FSEC profile shows a similar quality of protein in both human and rat PANX1.

The cells were solubilized in Tris buffer (pH 8.0) containing 20 mM DDM detergent. The elution volume and the protein quality were similar for both human and rat PANX1. Thus, human PANX1 was used for further studies (Fig. 3.1).

3.3 Initial Cryo-EM trials with DDM

PANX1 was solubilized in Tris pH 8.0, 100 mM KCl, 1% glycerol, and 25 mM DDM detergent (solubilization buffer). The protein was purified by Ni-NTA affinity chromatography and eluted with 250 mM imidazole supplemented buffer. The protein was further purified with size exclusion chromatography. The eluted protein was run on a superose 6 column in SEC buffer (25mM Tris pH 8.0, 100mM KCl, 1% glycerol, and 1.2 mM DDM).

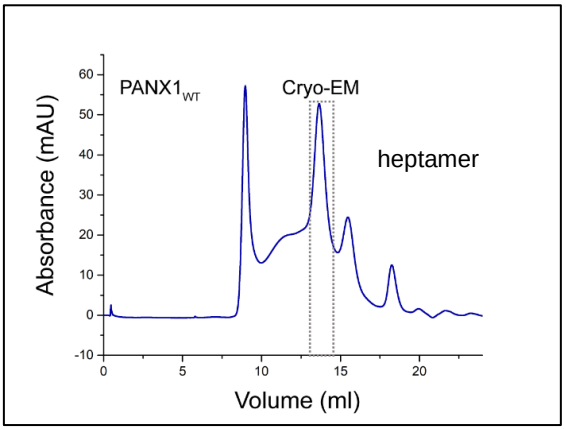

Fig. 3.2: Size exclusion chromatography profile for $PANX1_{WT}$ run on superose 6 10/300 column. A small peak at ~16 ml suggests that the protein is not completely stable in DDM.

The main peak fraction was concentrated to ~2 mg/ml and was used for grid freezing (Fig. 3.2). The data was collected on Titan Krios equipped with Falcon 3 direct electron detector.

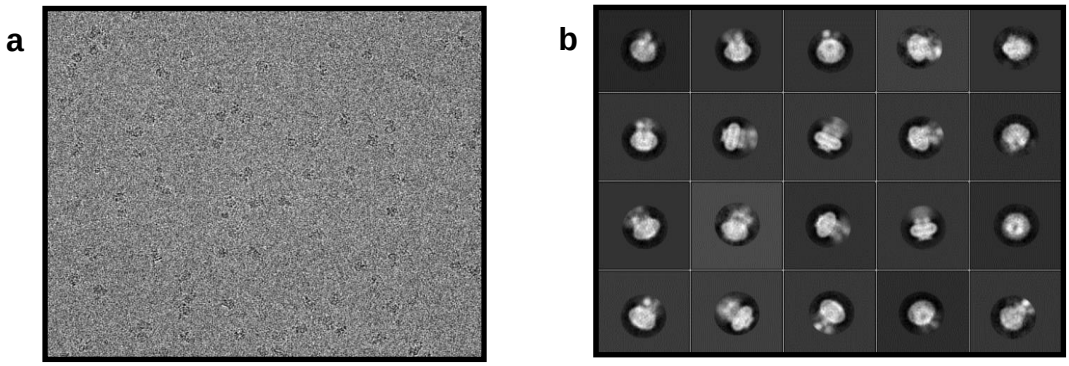

Fig. 3.3: a) Representative micrograph collected on Falcon 3 electron detector **b)** Representative 2D class averages showing side views of the $PANX1_{WT}$ channel.

As observed in the representative image of the grids, it did not have enough particles per micrograph, and no direct top/bottom views of the channel could be seen during 2D classification (Fig. 3.3 a-b). We performed detergent screening to eliminate the preferred orientation and get a more homogenous and stable protein.

3.4 Detergent screening

Membrane proteins are solubilized in detergent from their native membranes to retain their structural and functional properties. It is crucial to screen different detergents as they can affect a membrane protein's stability[147]. Detergents are amphipathic molecules and contain a hydrophobic head group and a hydrophilic tail. At a particular concentration, referred to as critical micellar concentration (CMC), the non-polar tails group together through a hydrophobic effect and form the core of the micelle. In contrast, the polar head groups align themselves with interacting with water. The CMC varies according to the detergent and depends upon the alkyl chain length of the detergent[123].

To extract the protein from the membranes, the detergent concentration is kept above the CMC for the detergent to form micelles around the protein, thereby stabilizing it as a detergent-protein complex. Although we could get a significant fraction as a higher oligomer, one more peak at 16 ml suggested the breakdown of PANX1 into lower oligomeric species (Fig. 3.1, 3.2). We used detergent screening to screen for a suitable detergent to improve the stability of PANX1. We screened non-ionic detergents with varying alkyl chains and CMCs, and we also screened a zwitterionic detergent, LDAO. We used small-scale transfections to screen multiple detergents simultaneously and solubilized the cells in different detergent solutions.

Higher alkyl chain non-ionic detergents such as DM, UDM, and DDM are milder towards the membrane proteins than shorter alkyl chain detergents such as β-OG or detergents with ionic head groups[148]. We observed two peaks corresponding to higher and lower oligomers of PANX1 when solubilized with DM, UDM, DDM, β-OG, and Cymal 6, suggesting that these detergents were unable to stabilize the PANX1 channel completely. Glycodiosgenin (GDN) is an amphiphile with a hydrophobic sterol group and a hydrophilic di-maltose head group and has a CMC of 17 μM. It is a synthetic derivative of digitonin[149]. It is a very mild detergent, and the extraction efficiency is lower than a non-ionic detergent, DDM.

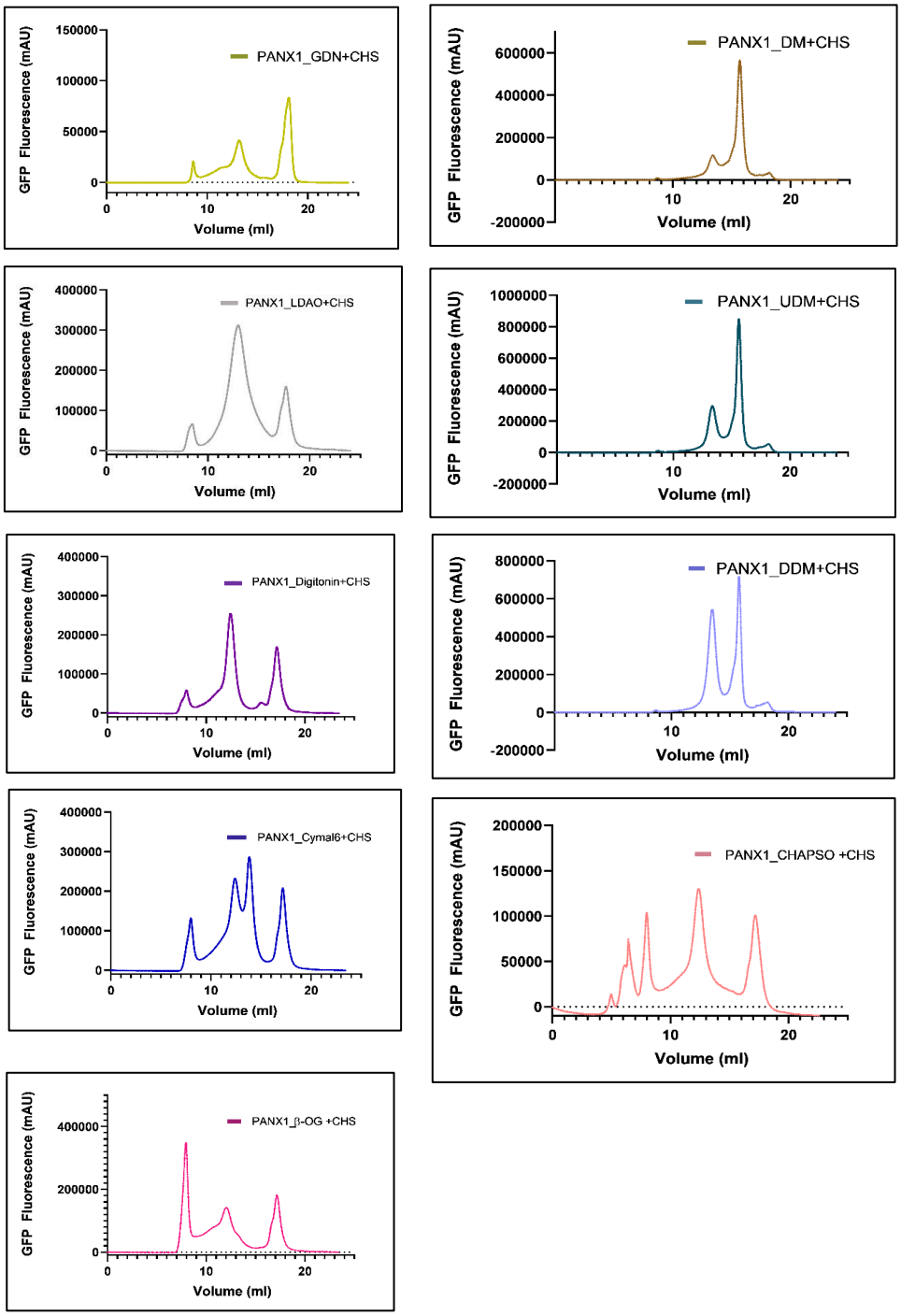

Fig. 3.4: FSEC profiles for PANX1 solubilized in different detergents run on a superose 6 column. The FSEC profiles suggest that although GDN (yellow) has low extractibility compared to other detergents, the PANX1 forms a stable heptamer in GDN.

Nonetheless, we were successful in getting intact PANX1 channels extracted in GDN. We used 10 mM of GDN as the detergent for solubilization of the membrane in subsequent protein extraction. The detergent concentration was decreased to 100 µM for eluting the protein, and the protein was further purified by SEC in 50 µM of GDN

(Fig. 3.4).

3.5 Sterol aids in oligomerization in PANX1

Cholesterol is the major component of the eukaryotic plasma membrane and modulates the fluidity of the membrane. Membrne proteins such as transporters and channels have been observed to be affected by the presence of cholesterol either directly or indirectly[150]. Moreover, cholesterol is one of the most frequently observed lipids with eukaryotic membrane proteins during crystallization or Cryo-EM structural determination[150].

To understand the effect of cholesterol on PANX1 channels, we transfected the cells and solubilized the cells with and without CHS (Cholesteryl Hemisuccinate tris salt). We analyzed the stability of the protein using FSEC. Although the protein was stable in the presence of cholesterol, the PANX1 channel was completely broken down into a lower oligomeric form in the absence of CHS, suggesting the need for cholesterol to help stabilize the channel (Fig.3.5-a).

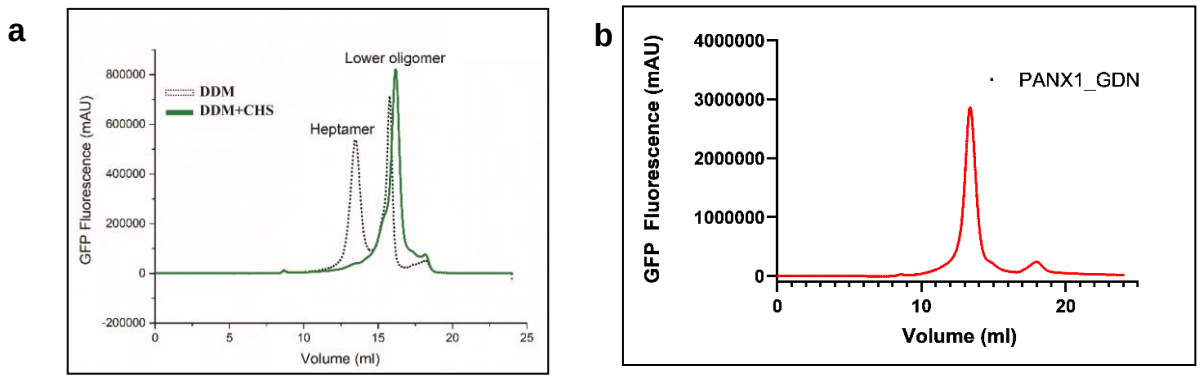

Fig. 3.5: a) FSEC profile for PANX1 with and without CHS, **b)** FSEC profile for PANX1 in GDN. GDN compensates for the need for cholesterol to stabilize the protein.

Glycodiosgenin (GDN) has a steroid group that DDM lacks, and we wanted to see if the steroid head group in GDN can compensate for CHS. We transfected the cells and solubilized them in GDN detergent in the absence of CHS. Interestingly, we observed that the PANX1 channel was stable in GDN, which suggests that PANX1 needs a sterol lipid to form a stable oligomer. (Fig.3.5-b).

3.6 Large-scale purification with GDN

PANX1 was purified on a large scale (3 litres of culture volume) using the Bacmam

system described in the methods section. Briefly, the membranes were solubilized in resuspension buffer (25 mM Tris pH 8.0, 100 mM KCl, 1 % glycerol,0.1 % PMSF) containing 10 mM GDN. The protein was eluted in a resuspension buffer with 100 µM GDN and 250 mM imidazole. The eluted protein was incubated for GFP cleavage using Tev protease for 16-20 hours at 18 ℃ in a ratio of 1:10 by weight (protein: tev protease). The protein was further purified by SEC using a superose 6 column, and the GDN concentration was reduced to 50 µM in SEC buffer.

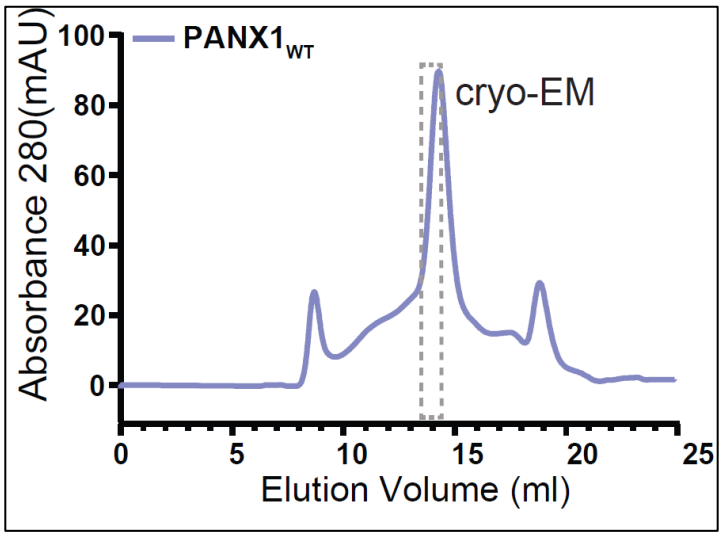

Fig. 3.6: Size exclusion chromatography (SEC) for GFP cleaved PANX1. The $PANX1_{WT}$ forms a stable heptamer in GDN and elutes at ~14-15 ml in a superose 6 column.

PAXN1 protein was purified to homogeneity, and the SEC fraction containing PANX1 was concentrated before grid freezing (Fig. 3.6).

3.7 PANX1 is a heptamer

After the discovery of PANX1, it was proposed that they would form hexamers akin to connexin hemichannels. Multiple groups gave experimental evidence to validate this hypothesis. Boassa *et al*. performed cross-linking experiments with PANX1 using DSP (dithiobis(succinimidyl propionate)), an amino reactive reagent. At a higher concentration of DSP, they could observe a band at ~290 KDa corresponding to a hexamer[15]. As we could not get any top views during the 2D classification, we assumed PANX1 to be a hexamer suggested by multiple groups.

After purifying PANX1 in GDN, we froze the Quantifoil gold holey carbon 1.2/1.3 grids with a blot time of 3.0 and 3.5 s. The data was acquired on Titan Krios equipped with a Falcon 3 direct electron detector at a magnification of 75,000x. The data was collected from the grid with a 3.5 s blot time as the ice thickness and particle distribution was optimal at this blotting time. We processed the collected data using Cryo-EM data processing software, Relion 2.0[151,152]. During 2D classification, all the views, top, bottom, side, and helices could be visualized in the 2D classes. The top and bottom view 2D classes of PANX1 revealed that PANX1 forms heptamer and not hexamers as previously thought. Moreover, heptameric oligomerization is not present in connexins and innexins and is unique to PANX1[104,153–155].

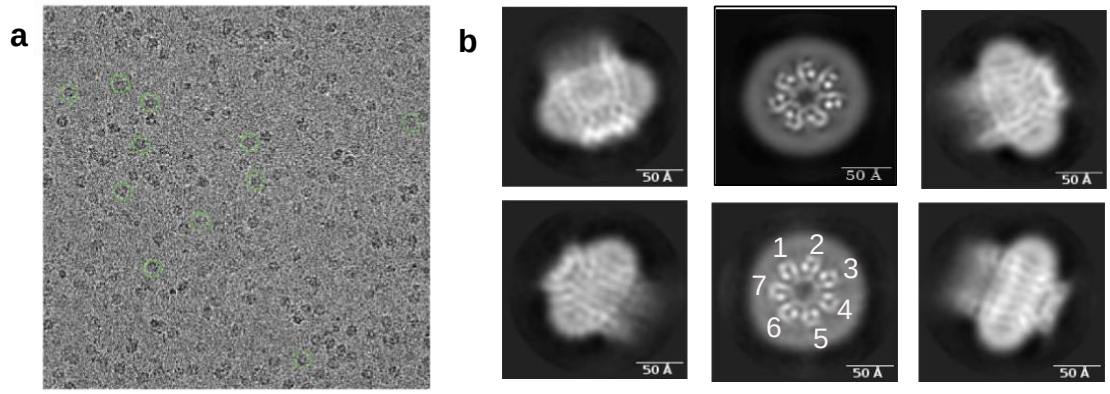

Fig. 3.7: a) Representative micrograph, the data was collected on a Falcon 3 direct electron detector, and green circles represent the picked particles **b)** Representative 2D classes exhibiting top, bottom, and side views processed in Relion 2.0 Cryo-EM software.

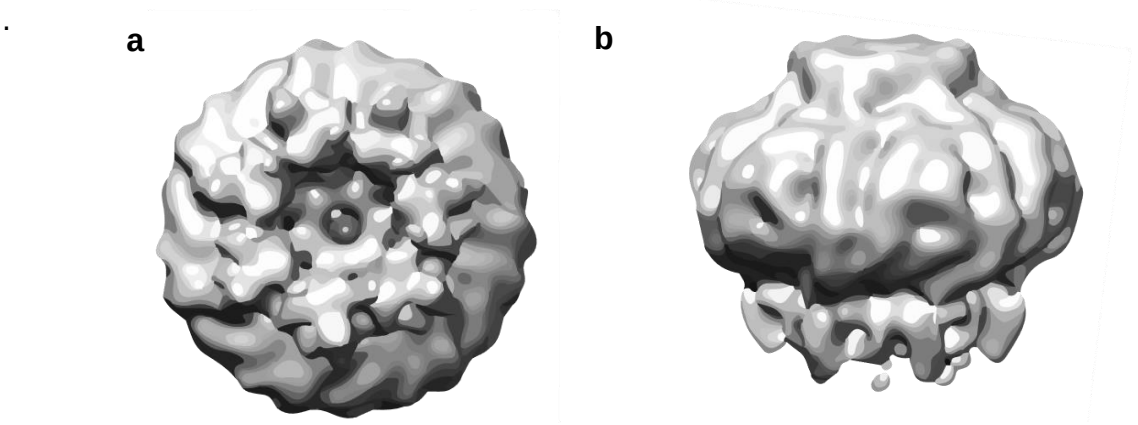

Fig. 3.8: Low-resolution Cryo-EM 3D reconstruction of PANX1 channel processed in RELION 2.0 Cryo-EM software. **a)** bottom view, **b)** side view.

Although we could get all the orientations of PANX1 molecules and 2D classes were

of high quality (Fig. 3.7). However, we were not successful in getting a proper 3D reconstruction. The micelles covered the entire channel completely. Even after several futile attempts, we failed to remove the micelles from the channel (Fig. 3.8). We performed the ab-initio with and without applying C7 symmetry and got similar results in both cases.

We also observed that PANX1 had a preferred orientation in GDN detergent. In a typical dataset, ~ 70% of views in the selected 2D classes were top and bottom. Although these views were important to have an idea about the oligomerization state of PANX1, they do not add any information to improve the resolution. We performed 3D classification with and without top views. The 3D reconstruction without top and bottom views yielded a better resolution.

It has been observed that adding detergents like CHAPSO can help circumvent preferred orientation during grid freezing by reducing denaturation and modifying the air-water interface[156]. However, it did not give us satisfactory results as the number of particles in ice was sub-optimal after adding CHAPSO to the sample during grid freezing. However, we screened the grids but did not proceed to collect the data.

In a study by Sensen Zhang *et al.,* the authors observed the preferred orientation of their molecule when the grids were frozen at a low concentration (2.5- 3.0 mg/ml), but when the grids were frozen at a higher protein concentration (5-6 mg/ml), the particles were present in all the orientations[56]. We used the same strategy for PANX1 and could get a decent number (50%) of side-view particles used for 3D reconstruction.

3.8 Low-resolution structural determination of PANX1

To remove the micelles, we again purified the PANX1 protein in GDN and froze the grids in liquid ethane. After multiple trials of purification, grid freezing, and data collection, we could get a better-quality grid and reached a nominal resolution of ~5.0 Å. However, there was no change in the parameters for grid freezing. However, for every round of grid freezing, we purified fresh PANX1 protein and batch-to-batch variation in terms of detergent, and the sample quality was inevitable.

The data was processed in both Relion and CryoSPARC with default parameters. As

we had multiple datasets for PANX1, we combined the datasets with the same magnification and Å/pixel value, but the resolution of the final 3D reconstruction did not improve. For the single dataset (Fig. 3.9), the number of particles contributing to 3D reconstruction was ~41K. The number of particles in the combined dataset was 224K and was divided into three 3D ab-initio classes. The ab-initio class containing the highest number of particles(70K) had a lower resolution than 3D reconstructed from 41K particles from a single dataset.

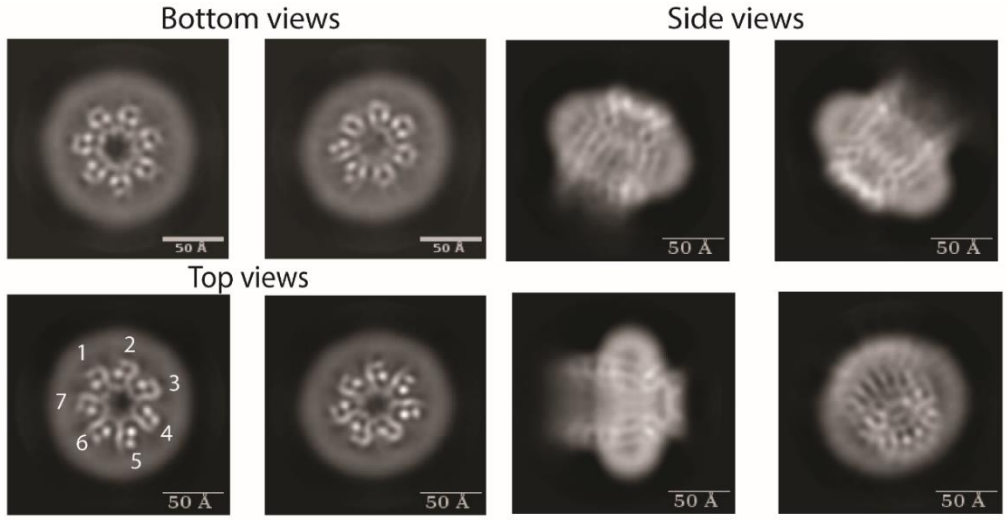

Fig. 3.9: Representative selected 2D classes exhibiting top, bottom, and side views. A total number of 224,000 particles was used for the 2D classification.

In conclusion, increasing the number of particles by combining multiple datasets did not improve the resolution of our 3D reconstruction.

3.9 Cryo-EM data processing optimization

The PANX1 channel is a heptamer with minimal extracellular and intracellular domains. The entire transmembrane domain is embedded within micelles that are disordered in nature. To obtain a higher resolution, we optimized parameters during the data processing. The optimization was done in CryoSPARC, as it gives more freedom to the user to manipulate the parameters according to the protein's behavior and is faster than Relion in terms of computing time[134].

As evident from the 2D classes, we had sufficient side views, and the particle quality was also good, as helices could be seen in the 2D classes. It has been observed that micelles give the strongest signal at ~6 Å and become harder to remove if the signal-

to-noise ratio is not good. To overcome this, we optimized the initial and final aligning resolution to 12 Å and 8 Å from 35 Å and 12 Å respectively. We also increased the minibatch size from 300 to 1000, which increases the number of particles in a batch and thus has more signal from the particles at each iteration during classification and can yield a higher resolution.

Table. 3.1 Parameter optimization for Ab-initio 3D reconstruction

Parameter	Default	Optimized
Maximum resolution (Å)	12	8
Initial resolution (Å)	35	12
Final minibatch size	300	1000

The changes in these few parameters led to the generation of a low-resolution map which was used to get a higher-resolution structure through non-uniform refinement. For non-uniform refinement, we optimized a few parameters to get a higher-resolution structure[138].

Table. 3.2: Parameter optimization for Non-uniform refinement

Parameter	Default	Optimized
Initial lowpass resolution (Å)	30	12
GSFSC split resolution (Å)	20	12
Initial batch size	300	1000
Batch size	0.01	0.5
Dynamic mask far (Å)	14	12
Dynamic mask start resolution (Å)	12	7
Minimum Fit Res (Å)	20	8
Defocus Search Range (Å +/-)	2000	200

In non-uniform refinement, we changed the defocus search range from 2000 to 200, and the batch size was increased to 1000 from 300. The initial and final dynamic mask resolution was also changed to 7 Å and 12 Å from 12 Å and 14 Å respectively. These optimized parameters helped us to get a better resolution structure in a small dataset.

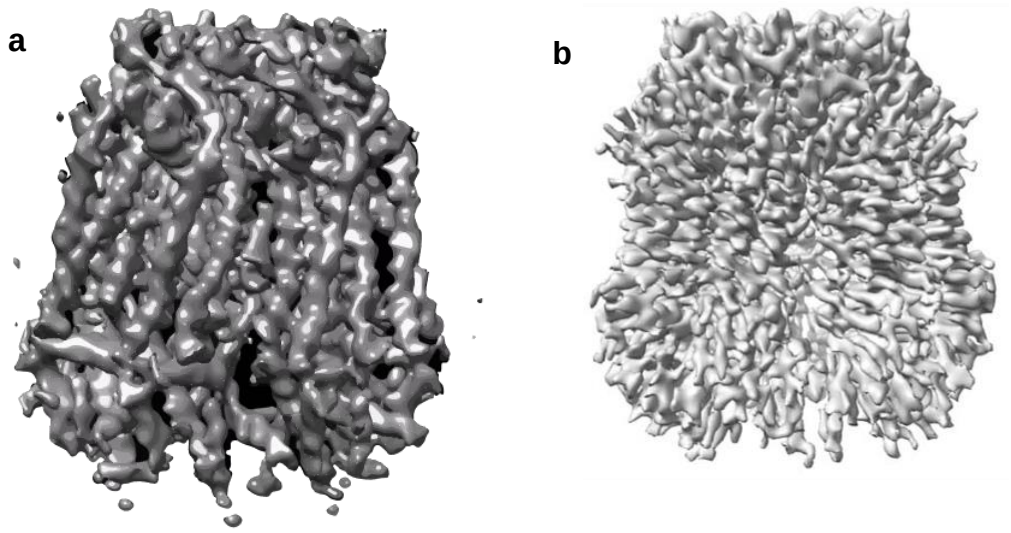

Fig. 3.10: Final 3D reconstruction for PANX1 **a)** with default parameters at 5.0 Å **b)** with optimized parameters at 3.75 Å. The data was processed in CryoSPARC 3.2. A total number of 41,000 particles were used for the 3D classification.

A workflow of the data processing with optimized parameters is given below (Fig. 3.11)

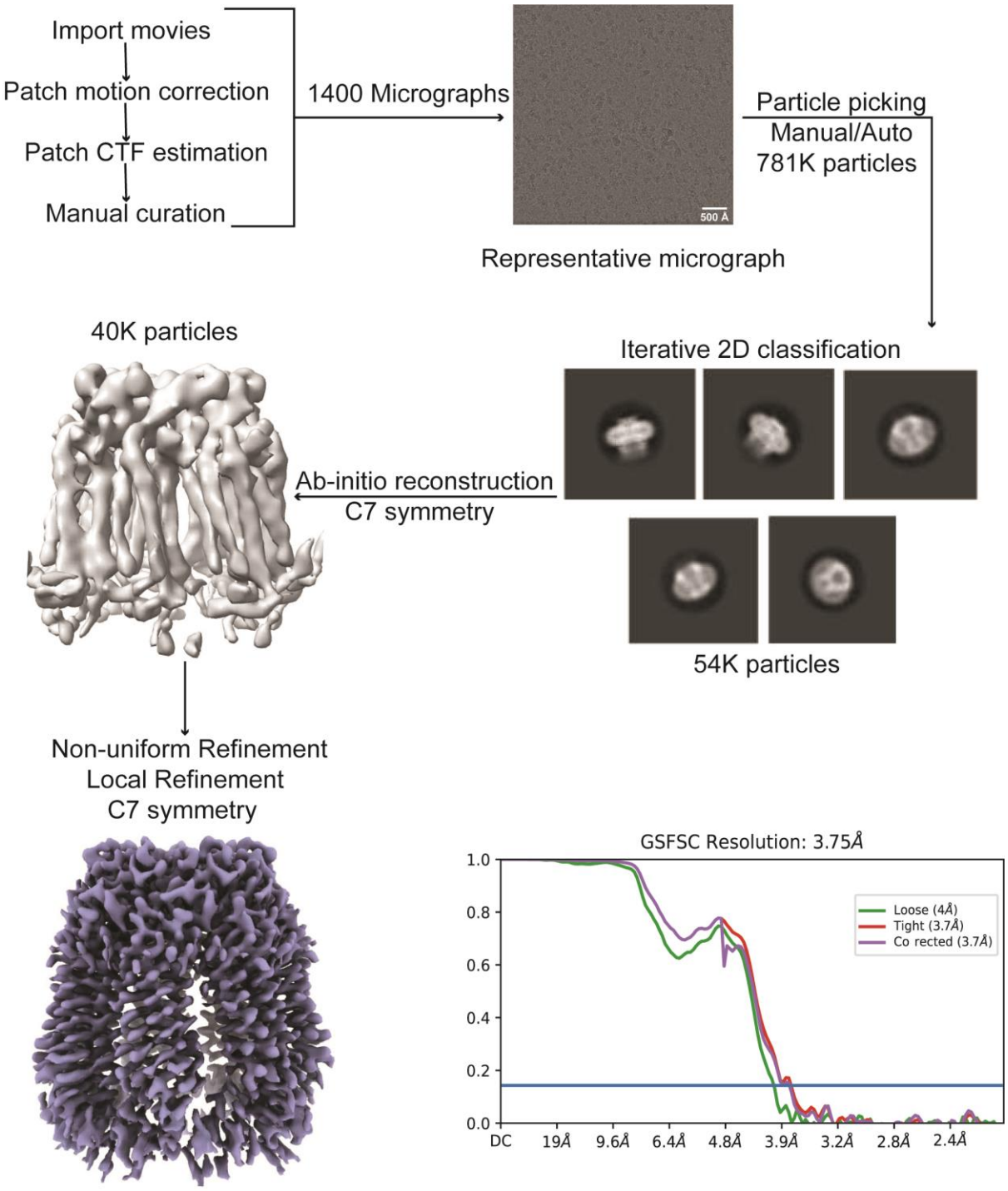

Fig. 3.11: Cryo-EM workflow for $PANX1_{WT}$.

Table: 3.3 Cryo-EM data collection, refinement, and validation statistic

Construct Name	PANX1 (EMD-34268)
Data collection and processing	
Magnification (x) Mode	75000 TEM
Voltage (kV) Detector Slit width (eV)	300 Falcon III -
Electron exposure (e^{-}/Å^2)	29.5
Defocus range (μm)	-1.8 to -3.3
Pixel size (Å)	1.07
Symmetry imposed	C7
Initial particle images (no.)	399706
Final particle images (no.)	41483
Map resolution (Å) FSC threshold	3.75 0.143
Refinement	
Initial model used (PDB code)	6WBF
Model resolution (Å) @ FSC 0.5	4.0
Map sharpening *B* factor (Å^2)	-179.6
Model composition Non-hydrogen atoms Protein residues Ligands B-factor (Å^2)	 17507 2310 0
Total Protein Ligands	50.10 50.10
R.m.s. deviations Bond lengths (Å) Bond angles (°)	 0.005(0) 1.087(0)
Validation MolProbity score Clashscore Poor rotamers (%)	 1.73 7.89
Ramachandran plot Favored (%) Allowed (%) Disallowed (%)	 95.68 4.32 0.00

3.10 $PANX1_{WT}$ structure and its comparison with the existing $PANX1_{WT}$ structures

Although we determined the PANX1 structure at 3.75 Å resolution, multiple groups worldwide determined the structure of $PANX1_{WT}$ in 2020. In this section, we compared our PANX1 structure to a much higher resolution structure (2.9Å) to understand its structural features.

PANX1 is a heptamer channel, and its Cryo-EM structure was determined at a resolution of 3.75 Å. The side chain in most of the regions was sufficient for model building. The $PANX1_{WT}$ model was built using the previously determined structure from Ruan *et al*. (PDB-ID 6WBF)[17]. A part of the N-terminus (11-24 residues), the intracellular region (160-190 residues), and the C-terminus were not modeled due to the lack of density in the regions.

3.10.1 Structural features of PANX1

PANX1 is divided into three domains, extracellular domain (ECD), intracellular domain (ICD), and transmembrane domain (TMD) (Fig. 3.12-a). The intracellular domain is wider than the extracellular domain, and the transmembrane domains contain a bundle of four helices that lines the exterior wall. The N-terminus lies in the pore in the space between two transmembrane domains.

Although we could not model the complete N-terminus, Ruan *et al*. suggest the role of the N-terminus in maintaining a rigid TMD as the removal of the N-terminal helix led to a TMD in a truncated elliptical cone shape[17]. (Fig. 3.12-b)

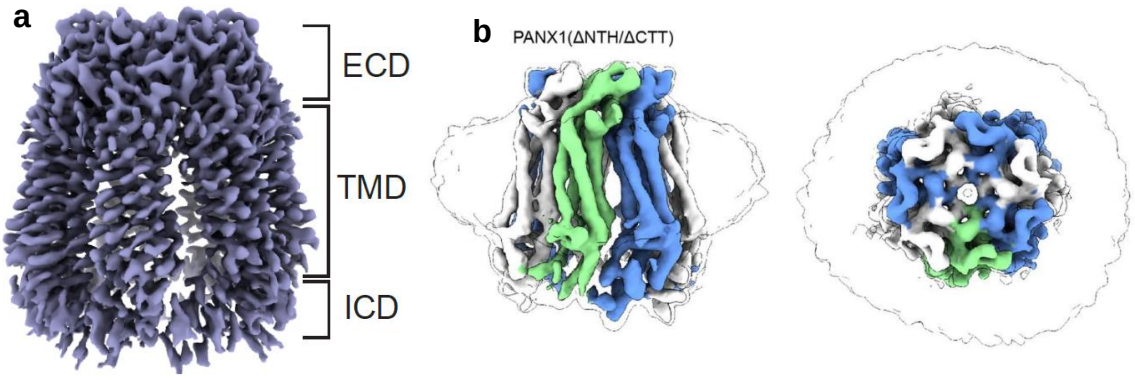

Fig. 3.12: a) Overview of PANX1 structure, PANX1 is partitioned into ECD (Extracellular domain), TMD (Transmembrane domain), and ICD (Intracellular domain) **b)** A study by Ruan *et al*. suggests the role of N-terminus in maintaining the rigid TMD[17].

The authors observed that the gap between the TMDs was filled with lipids. However, the gap in our structure lacked lipid-like densities, possibly because of the lower resolution. We also did not observe glycosylation density at N255, as observed by Ruan *et al.* [17].

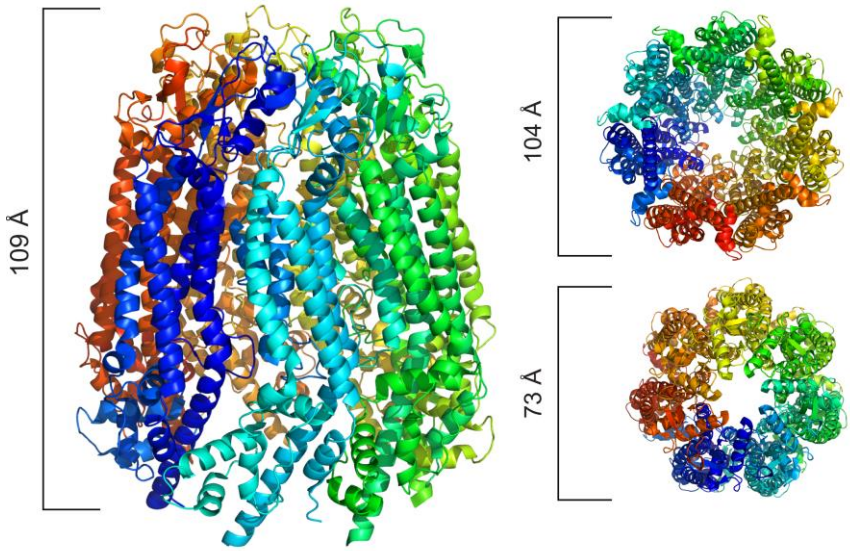

Fig. 3.13: $PANX1_{WT}$ exhibiting side, top, and bottom view. The $PANX1_{WT}$ is 109 Å in length. The cytoplasmic side of $PANX1_{WT}$ has a width of 104 Å and is broader than the intracellular side (73 Å).

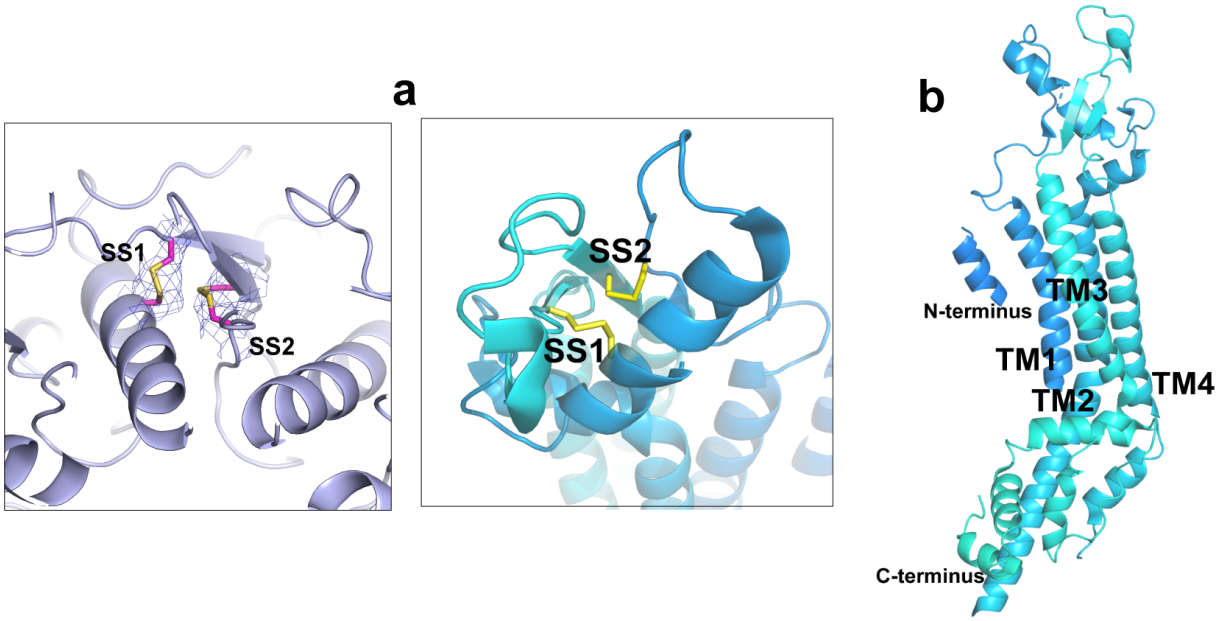

Fig. 3.14: a) Position of disulfide bonds (SS1, SS2) in a single subunit of PANX1, density for two disulfide bonds at 5.0 σ, **b)** Single subunit of $PANX1_{WT}$ with four transmembrane helices, two extracellular loops, and N-terminus. The intracellular loop and C-terminus were not

modeled due to the lack of density in these regions.

The PANX1 is 109 Å long, the extracellular domain is 70 Å wide, and the cytoplasmic/ intracellular domain is 26 Å wider than the extracellular domain (Fig. 3.13).

In a single subunit of PANX1, the ECD consists of two extracellular loops, EL1 and EL2, and two disulfide bonds are present between EL1 and EL2 (Cys84-Cys246(SS1), Cys66-Cys265(SS2)).

The SS1 lies between a β sheet and a helix, and SS2 lies between the β sheet and a loop. (Fig. 3.14a-b) The extracellular domain consists of three antiparallel β sheets and is strengthened by these disulfide bonds.

The PANX1 permeation pathway is along the entire length of the channel, and constrictions are created by W74 (first constriction) and I58 (second constriction).

The smallest constriction in PANX1 is formed by W74, which forms a ring (Fig. 3.15-a). It interacts with R75 of the adjacent subunit, possibly through cation-pi interaction[17,28]. The R75 interacts with D81 of another subunit through a salt bridge (Fig. 3.15-b). These inter-subunit interactions are required for the stability of PANX1 heptamer. Moreover, R75 is implicated in anion selectivity in PANX1 channels[28].

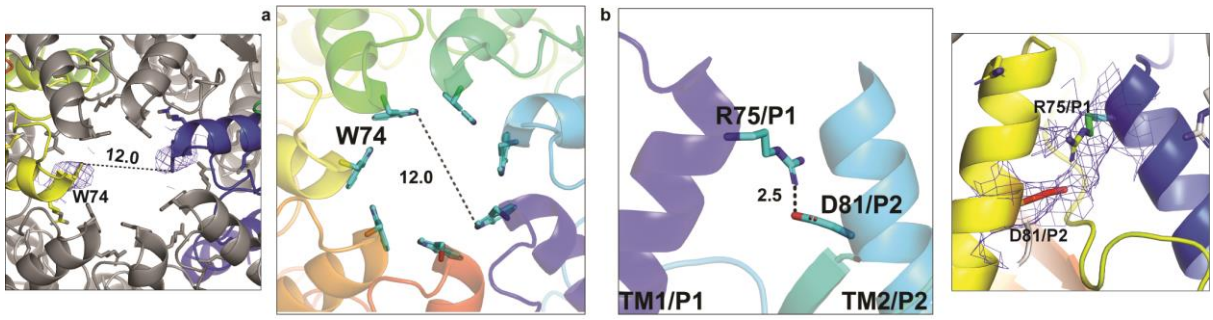

Fig. 3.15: a) W74 forms the smallest constriction in PANX1, density for W74 in two protomers is shown, contoured at 5.0 σ **b)** Interaction between R75 of one protomer(P1) with D81 of second protomer(P2) in PANX1, density for R75 and D81 is shown at 5.0 σ.

The smallest distance between the two tryptophan in PANX1 is 12 Å and is considered the primary binding site for carbenoxolone, a PANX1 inhibitor. The C-terminus of PANX1 is believed to be inside the pore and acts as a blocker[157]. However, no structural validation has been observed till now for the hypothesis.

3.11 PANX1 elicits current at the positive voltage

PANX1 has been observed to elicit currents at positive voltages by multiple groups[13,51,53]. We performed electrophysiology patch clamp recordings in whole cell mode in $PANX1_{WT}$ transfected HEK293 cells to gain insight into the voltage activation of PANX1. Whole-cell recordings of un-transfected HEK293 cells were kept as a control. Carbenoxolone (100 µM) was used to block the PANX1-generated currents (Fig. 3.16). The PANX1 channel exhibited a small current from -60 to 0 mV, and the current amplitude increased from 0 to +120 mV, suggesting the opening of PANX1 channels at positive voltages (Fig. 3.17-a, 3.17-b)

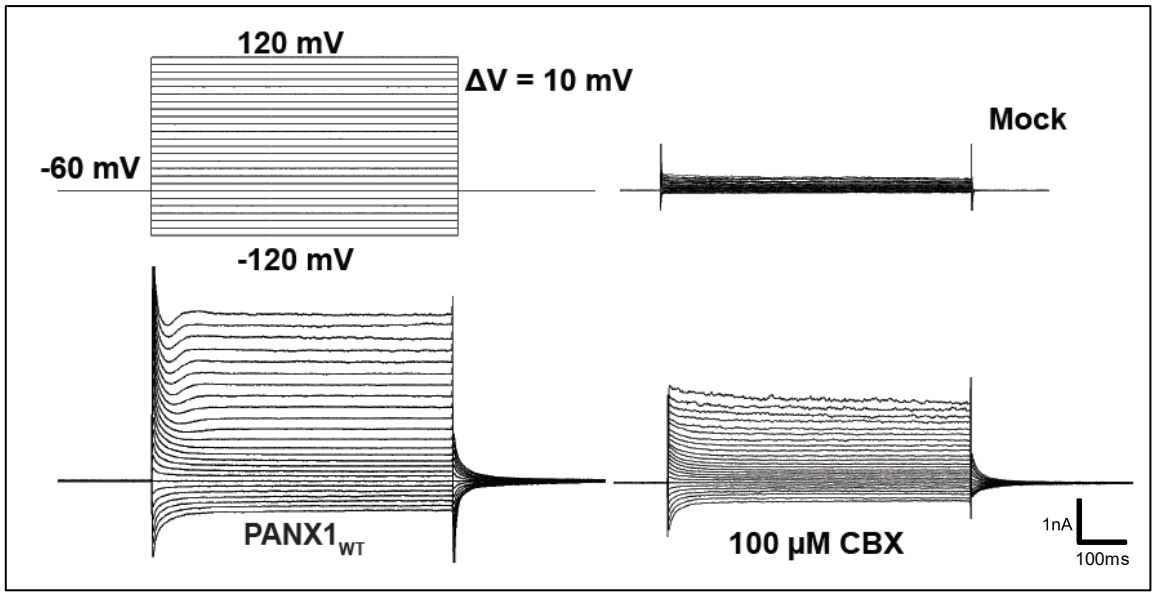

.

Fig. 3.16: The protocol used for patch clamp is shown; the voltage steps of 10mV were applied from -120 to +120, mock recordings (un-transfected HEK293 cells) were done prior to the $PANX1_{WT}$ experiments; Representative traces for whole-cell current for HEK293 cells expressing $PANX1_{WT}$ is displayed, 100µM CBX was applied in a bolus mode to study the effect of the inhibitor on $PANX1_{WT}$ channels.

A decrease of 60% in current amplitude was observed when the CBX, a PANX1 blocker, was applied (Fig. 3.16-b). A reversal potential of -60 mV was observed in PANX1. The PANX1 exhibited outward rectification at voltages > 20 mV.

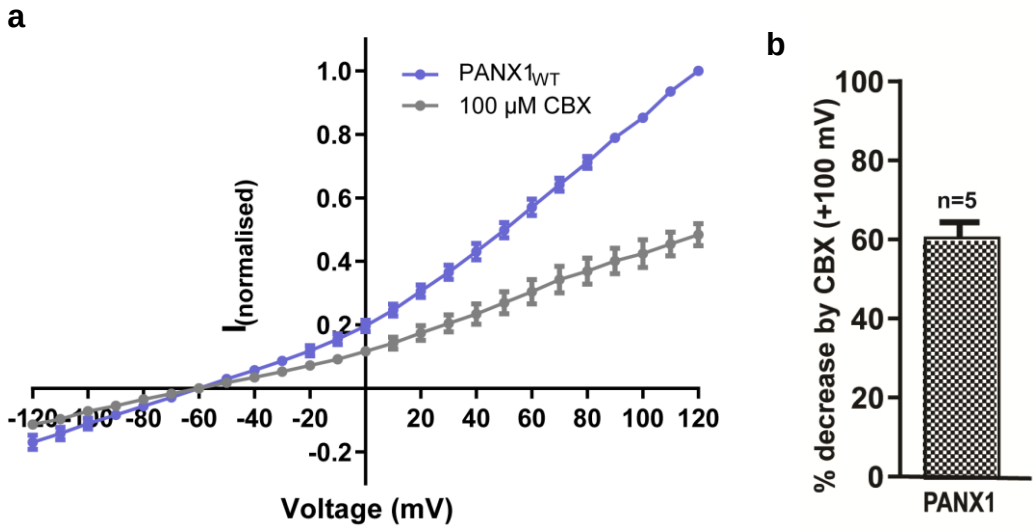

Fig. 3.17: Patch clamp studies of $PANX1_{WT}$ **a)** Current-voltage (IV) plot for $PANX1_{WT}$ in the presence(grey) and absence of CBX (blue). Each point represents the mean of 5 individual recordings, and the error bar represents SEM **b)** Percentage inhibition by a PANX1 inhibitor, CBX plotted at +100mV.

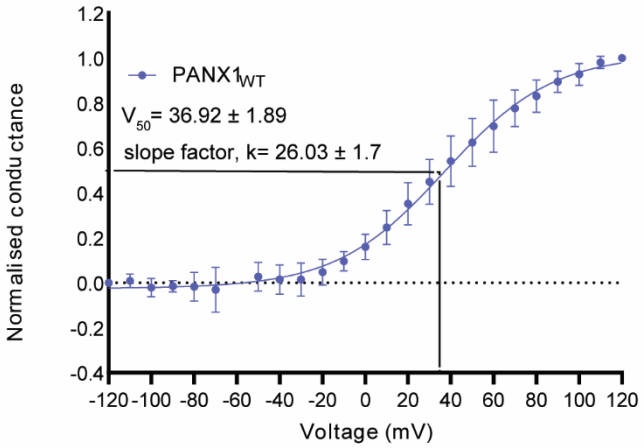

Fig. 3.18: The normalized G-V values were fitted with the Boltzmann equation, and the voltage at which the half-maximal activation, V_{50}, occurred along with a slope factor, k, was calculated for $PANX1_{WT}$ (n=8).

As seen through the rectification pattern, the activation of $PANX1_{WT}$ seems to be

dependent on voltage. To understand the voltage dependence of $PANX1_{WT}$, we plotted the conductance-voltage (G-V) curve (Fig. 3.18)

$PANX1_{WT}$ shows an increasing conductance from -20 to +80, reaching a plateau above +80, and the maximal voltage activation was present at +100 mV. Although it would be relevant to increase the voltage to more than +120, the HEK293 cells did not survive such high voltages to perform whole-cell recordings. The G-V curve was fitted using the Boltzmann equation, described in the method section. For $PANX1_{WT}$, $V_{0.5}$, the half-maximal activation voltage was calculated as 36.92 ± 1.89 with a slope factor(k) of 26.03 ± 1.7. The slope factor for $PANX1_{WT}$ is large compared to the voltage-dependent potassium channels, suggesting weak dependence of $PANX1_{WT}$ on voltage.

3.12 ATP-γS interaction with PANX1

PANX1 has been observed to involve in many physiological and pathological states through its ATP release activity. The ATP release activity of PANX1 channels has been explored by many groups in different cell lines, such as Hela, HEK293, and MDCK[158,159,160]. Although considerable data on PANX1 ATP release activity is present in the literature, noreports on the binding affinity of ATP to PANX1 channels are currently available.

To fill this gap in the literature, we used microscale thermophoresis (MST) to calculate the binding affinity of PANX1 with ATP-γS.

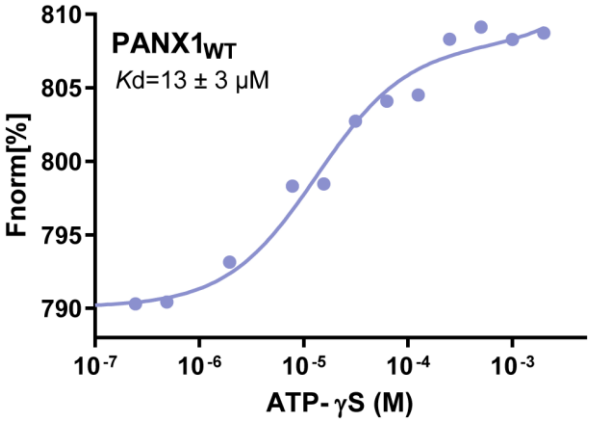

Fig. 3.19: Binding affinity with ATP-γS, a non-hydrolyzable analog of ATP. The binding affinity

for PANX1 was determined as 13±3 μM.

We used a non-hydrolyzable ATP analog, ATP-γS, to measure the binding affinity of PANX1 with ATP. The binding affinity was calculated as 13±3 μM (Fig. 3.19). The data was fitted in GraphPad Prism using one site-total binding equation.

3.13 Summary

Pannexins (PANXs) are large-pore vertebrate channels related to invertebrate innexins[7]. PANX1 is ubiquitously present and is the most studied isoform. PANX1 participates in numerous processes, including apoptosis, viral replication, and cell migration[64,77].

In this chapter, we have optimized protein purification by optimizing a detergent that stabilizes PANX1 in detergent micelles. We also discuss our attempts to optimize Cryo-EM parameters in length. These trials were required to get a moderate resolution structure from a small particle dataset. After optimizing the parameters, we determined the structure of $PANX1_{WT}$ at 3.75 Å resolution.

$PANX1_{WT}$ is a heptamer with the smallest constriction formed by W74. The protomer consists of four helices with N-terminus towards the pore. Although the location of the C-terminus is suggested to be inside the pore[161], we could not model C-terminus due to the lack of density in that region. Interestingly, PANX1's transmembrane helices are arranged like LRRC8, Connexins, and Innexins[103,162,163].

In order to better understand the functional role of PANX1, we examined the voltage dependence of PANX1 and found that PANX1 has a weak dependence on positive voltages. We also provided proof of concept for its ATP release activity by directly measuring PANX1's ATP- -γS binding affinity using microscale thermophoresis (MST).

In conclusion, we optimized the biochemical isolation and Cryo-EM structure determination strategy and applied it to get a better resolution structure. We also delved into the voltage dependence of the $PANX1_{WT}$ channel and estimated its binding affinity with ATP-γS. We used these optimized experimental parameters to understand the implications of mutations in the PANX1 channel on its structure and function in the next chapter.

CHAPTER 4

Structural insights into pore dynamics in PANX1 mutants

4.1 Introduction

PANX1 is an ATP-release channel involved in paracrine signaling. Given its ubiquitous expression and involvement in many physiological processes, PANX1 pathologies are expected to affect multiple organs.

In a study by Qing Shao *et al*., the authors reported the first germline variant in PANX1, which leads to reduced channel function and is associated with multiple organ dysfunction[164]. The authors observed the substitution of arginine to histidine at the 217 position. The mutant is not dominant negative as observed by co-expressing PANX1 wild type and showed normal N-glycosylation and trafficking when transfected in N2A, HEK293, Hela, and Ad293 cell lines[164].

A loss of function was observed in the $PANX1_{R217H}$ mutant by performing ATP release, dye uptake, and electrophysiology analysis[164].

4.2 Germline mutation in PANX1

The arginine at the 217 position is highly conserved in vertebrates (Fig. 4.1-a). It is present in TM3 (Fig. 4.1-b) and forms an H-bond network with its surrounding residues, and mutating arginine with histidine is observed to have reduced channel activity.

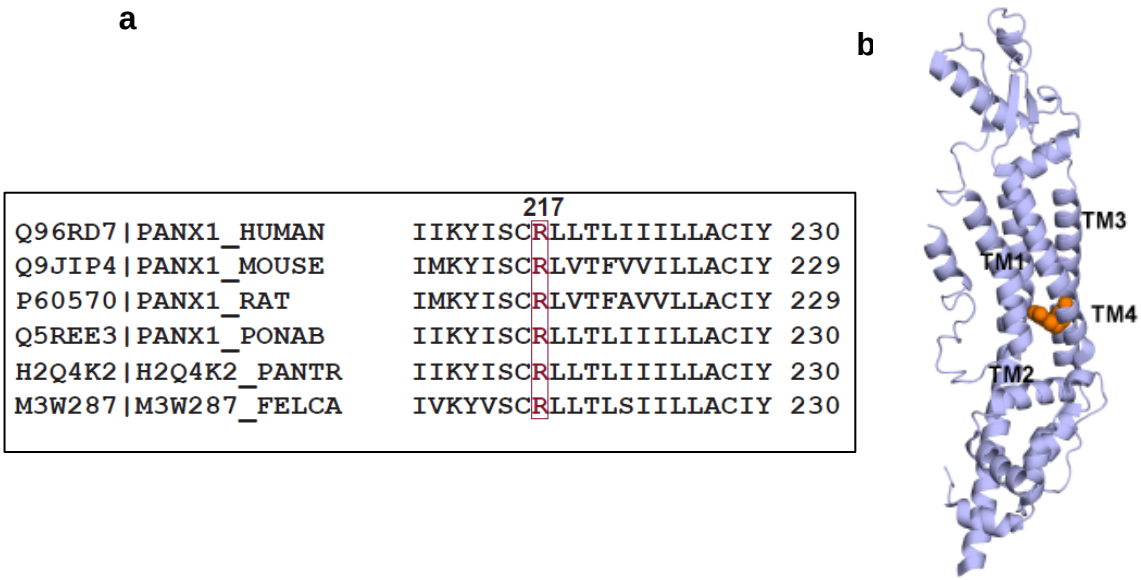

Fig. 4.1: a) R217 is conserved in vertebrates, for clarity, we have shown only a few species, **b)** R217 is located at TM3 and interacts with TM1, as shown in PANX1 protomer.

4.3 Expression and Purification of PANX1$_{R217H}$

To investigate whether the observed reduced channel activity in the PANX1 mutant is because of the compromised expression of PANX1$_{R217H}$, we employed FSEC to compare the expression of the PANX1$_{WT}$ and PANX1$_{R217H}$.

For FSEC, HEK293 GNTI^{-} cells at a density of 1*10^{6} were transfected with an equal amount of DNA (1 µg) for both constructs. Cells were harvested 36 hours post-transfection and solubilized in 10 mM GDN (200 µl), and the crude lysate was run on a superose 6 column.

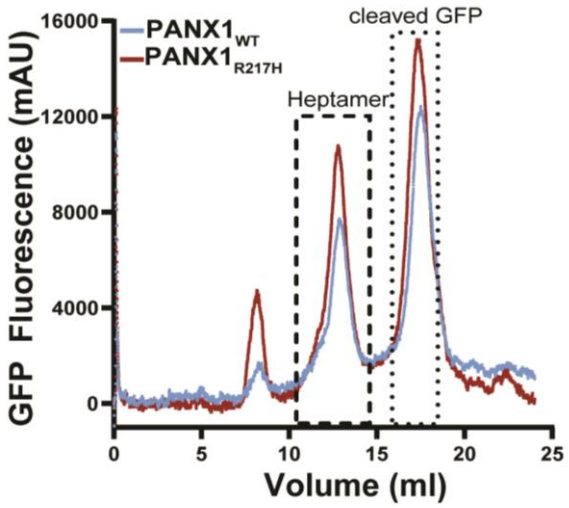

Fig. 4.2: FSEC profile for PANX1$_{WT}$ (blue) and PANX1$_{R217H}$ (red) run on a superose 6 10/300 GL column. The PANX1$_{WT}$ and PANX1$_{R217H}$ elute at the same volume (~14 ml).

As seen in the FSEC profile (Fig. 4.2), the expression of the mutant channel is similar to the PANX1$_{WT}$, thereby suggesting that the reduced functional activity of the mutant channel is not a consequence of compromised protein expression.

To understand the impact of the mutation on the channel's structure, we purified PANX1$_{R217H}$ on a large scale using the Bacmam system described in the methods.

The Ni-NTA purified sample was subjected to GFP cleavage using tev protease for 16 hours at 16 ℃. The cleaved sample was run on a superose 6 column to separate the cleaved GFP.

The main peak of the SEC profile was concentrated to 2.5 mg/ml. It was used for grid freezing (Fig. 4.3). The data was collected from the double-blotted grids (mentioned in the method section).

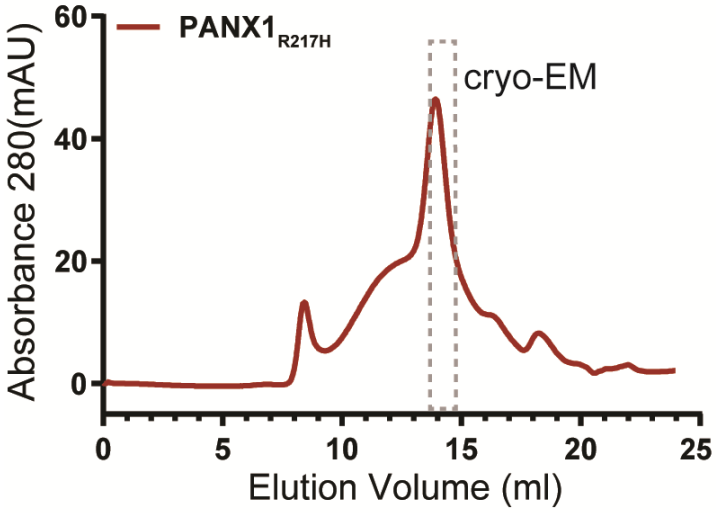

Fig. 4.3 Size exclusion chromatography (SEC) profile for $PANX1_{R217H}$ on a superose 6 10/300 GL column. The elution volume for the mutant channel PANX1R217H is ~14 ml, consistent with the wild type (Fig. 4.2)

4.4 $PANX1_{R217H}$ structure determination by CryoEM

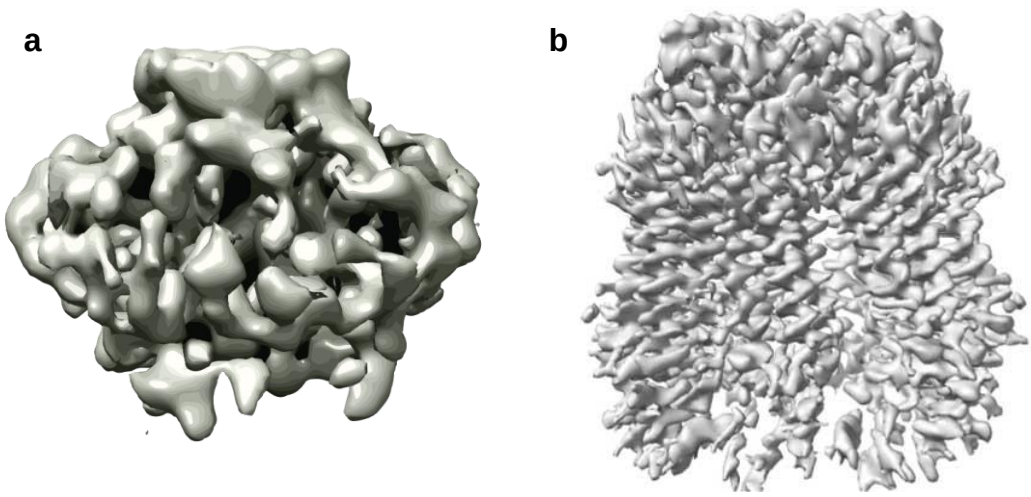

Fig. 4.4: The grids were double-blotted with the diluted sample(~1.5 mg/ml). The data was collected on a K2 direct electron detector and processed in CryoSPARC software. 3D reconstruction of $PANX1_{R217H}$. **a)** with default parameters, **b)** with optimized parameters.

As observed for $PANX1_{WT}$ (Chapter 3), the default parameters in CryoSPARC during data processing did not yield a high-resolution reconstruction. For the R217H mutant, after multiple attempts, we could not eliminate the micelle's signal from the mutant channel (Fig. 4.4-a).

The parameters were optimized for the mutant, and the optimized parameters could give us a moderate resolution 3D reconstruction at 3.9Å (Fig. 4.4-b).

Table 4.1: Ab-initio reconstruction optimized parameters

Parameter	Default	Optimized
Maximum resolution (Å)	12	6
Initial resolution (Å)	35	12
Final minibatch size	300	1000

Table 4.2: Non-uniform refinement optimized parameters

Parameter	Default	Optimized
Initial lowpass resolution (Å)	30	12
GSFSC split resolution (Å)	20	10
Initial batch size	300	1000
Batch size	0.01	0.5
Dynamic mask far (Å)	14	12
Dynamic mask start resolution (Å)	12	7
Minimum Fit Res (Å)	20	6
Defocus Search Range (Å +/-)	2000	200

The Cryo-EM data was collected on Titan Krios (300 KeV) equipped with a K2 direct electron detector in EFTEM mode with a Bio-quantum energy filter and a slit width of 20 eV. The data was processed in CryoSPARC (Fig. 4.5).

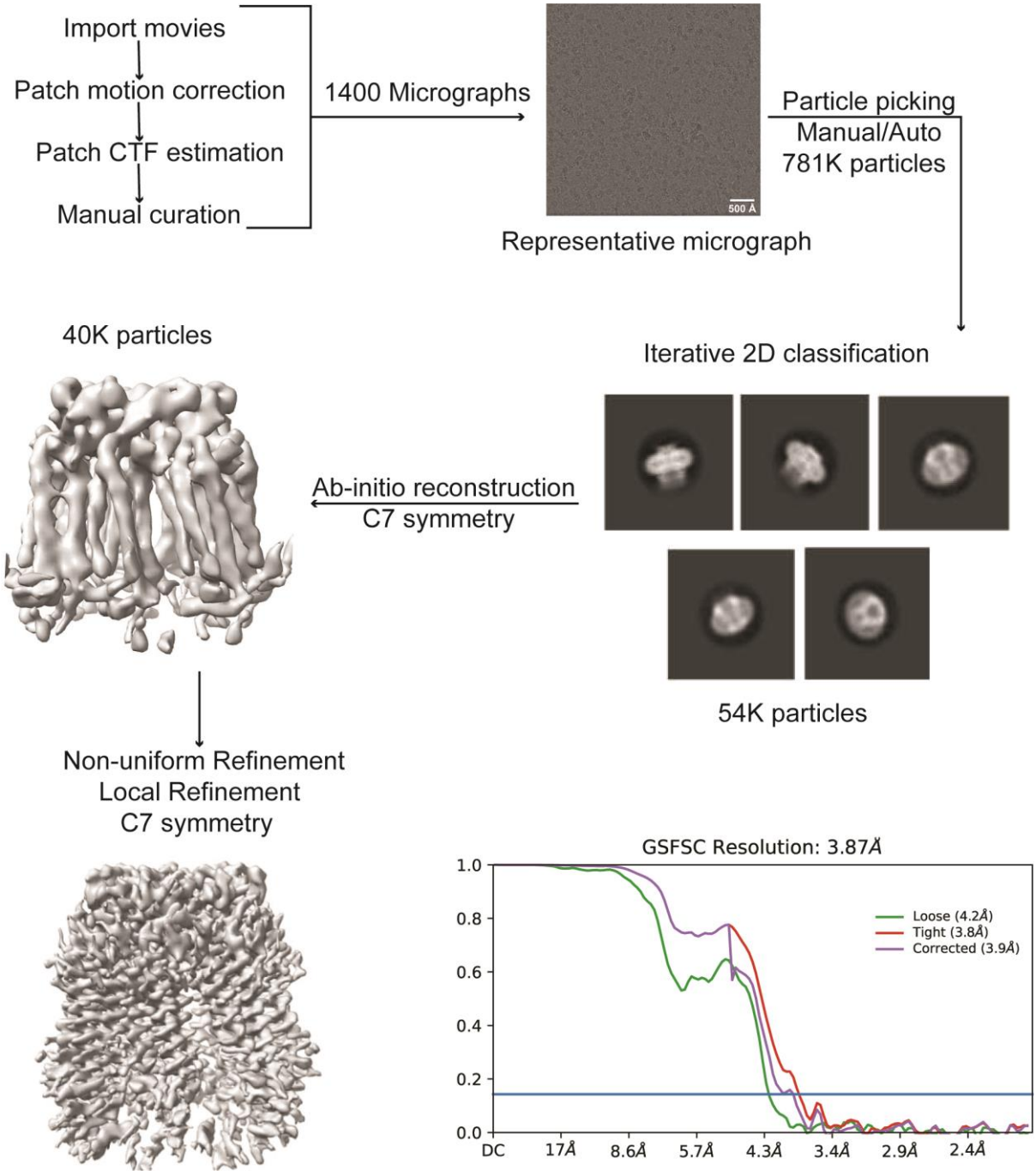

Fig. 4.5: Cryo-EM workflow for $PANX1_{R217H}$ mutant

Table 4.3: Cryo-EM data collection, refinement, and validation statistics

Construct Name	$PANX1_{R217H}$ (EMD-34268)
Data collection and processing	
Magnification Mode	130000 EFTEM
Voltage (kV) Detector Slit width (eV)	300 K2 20
Electron exposure (e^{-}/Å^2)	41.12
Defocus range (μm)	-1.8 to -3.3
Pixel size (Å)	1.07
Symmetry imposed	C7
Initial particle images (no.)	781859
Final particle images (no.)	40873
Map resolution (Å) FSC threshold	3.87 0.143
Refinement	
Initial model used (PDB code)	6WBF
Model resolution (Å) @ FSC 0.5	4.2
Map sharpening *B* factor (Å^2)	-156.0
Model composition Non-hydrogen atoms Protein residues Ligands	 15470 2016 -
B-factor (Å^2) Total Protein Ligands	 102.2 102.2 -
R.m.s. deviations Bond lengths (Å) Bond angles (°)	 0.004 1.057
Validation MolProbity score Clashscore Poor rotamers (%)	 1.65 10.7 0
Ramachandran plot Favored (%) Allowed (%) Disallowed (%)	 97.4 2.6 0

4.5 Congenital mutant of PANX1 (R217H) influences channel properties

The superposition of the wild type and the mutant structure yielded an rmsd of 1.2 Å for 288 Cα aligned. We generated the electrostatic potential for $PANX1_{WT}$ and $PANX1_{R217H}$ structures using APBS in Pymol and compared the electrostatic surface potential of the permeation pathway (Fig. 4.6).

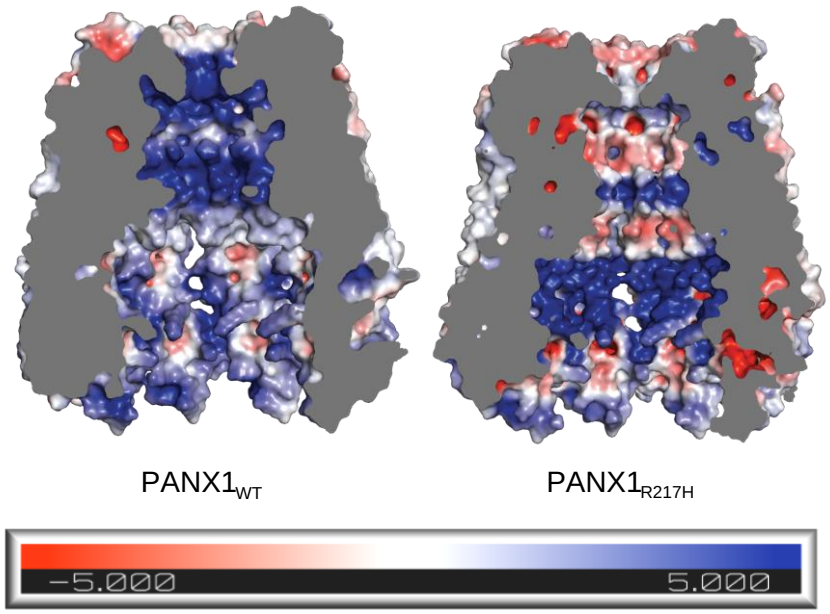

Fig. 4.6: Surface representation of $PANX1_{WT}$ and $PANX1_{R217H}$ according to the electrostatic surface potential from -5(red) to +5(blue) (k_BTec^{-1}) viewed parallel to the membrane plane. The PANX1 channel shows surface charge alteration owing to an R217H mutation.

The $PANX1_{WT}$ was trimmed to mimic the $PANX1_{R217H}$ channel's density for the modeled region for a better assessment of the electrostatic potential. Since $PANX1_{R217H}$ lacked N-terminus density (residue 11-24), the region was deleted from the $PANX1_{WT}$ model to compare the differences in the electrostatics potential owing to the similar residues.

The $PANX1_{WT}$ exhibits a positive charge between the first and second constrictions. In contrast, the R217H mutant has a negative patch at the same location, suggesting that the alteration of the electrostatic potential is a consequence of the mutation.

The mutant channel resembles the wild type globally. The superposition of $PANX1_{R217H}$ and $PANX1_{WT}$ reveals an outward shift of extracellular domains (ECD) by

1.5-2 Å and an inward shift of ~2 Å in intracellular domains (ICD), leading to the elongation of the transmembrane domain (TMD) in the mutant channel.

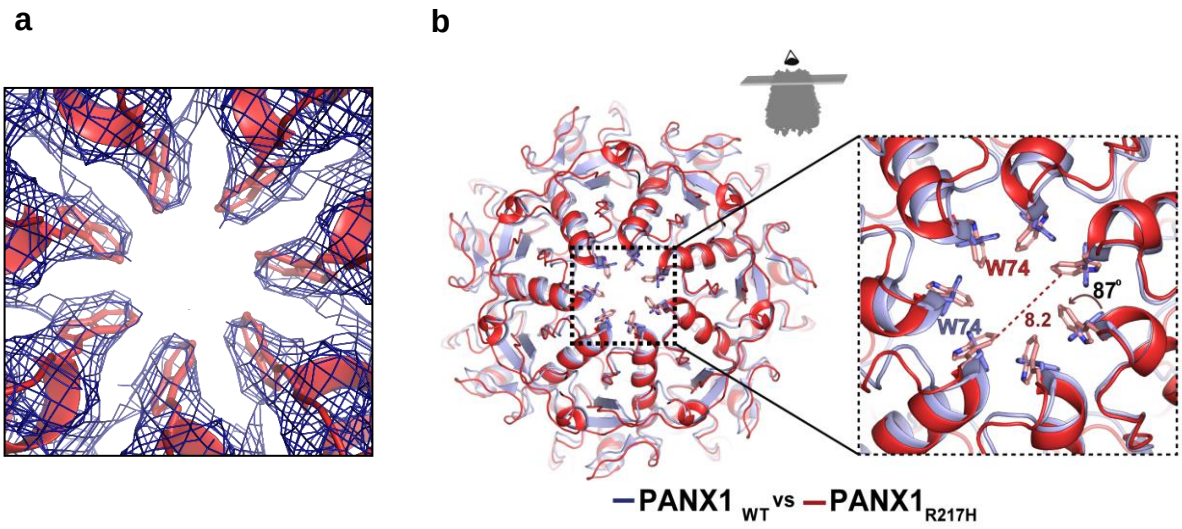

Fig. 4.7: a) The density for Trp74 in PANX1$_{R217H}$, **b)** A crosssection of superposed PANX1$_{WT}$ (blue) and PANX1$_{R217H}$ (red); the inset shows the residue (W74) involved in the formation of the extracellular entrance of the pore. The dashed line represents the reduced pore distance in Å in PANX1$_{R217H}$. (red).

Although the overall structure fold of the R217H mutant remains similar to PANX1$_{WT}$, the PANX1$_{WT}$ appears to exist in a constricted state. The mutation leads to the straightening of the TMD and makes the channel more elongated/relaxed.

The most prominent structural change in the mutant channel is the constriction of the pore diameter. The smallest constriction in the wild type is formed by W74 (12 Å). However, the R217H mutation in TM3 makes it more constricted to 7.6-8.2 Å (Fig. 4.7). The superposition of PANX1$_{WT}$ to PANX1$_{R217H}$ reveals the shift of W74 by χ1 torsion angle of ~87° towards the pore, thereby shortening the pore radius by ~4 Å. The movement of W74 does not alter the H-bond interaction between R75 and D81 in adjacent protomers in the mutant channel, consistent with the PANX1$_{WT}$ (Fig. 4.8 a-b).

As the mutation is in TM3, we also investigated the structural changes locally and inspected the interaction network of R217 within a distance of 4 Å. The D35 in TM1 interacts with R217 in PANX1$_{WT}$ (3.6 Å) and forms an H-bond. Additionally, R217 interacts with the T220 in TM3 and T39 in TM1. The substitution of arginine to histidine in the congenital mutant leads to the disruption of the local network (Fig.4.8-b).

The G44 in TM1 acts as a hinge point, and the displacement in the TM1 due to the disruption of the local network is propagated, leading to the partial closure of the pore.

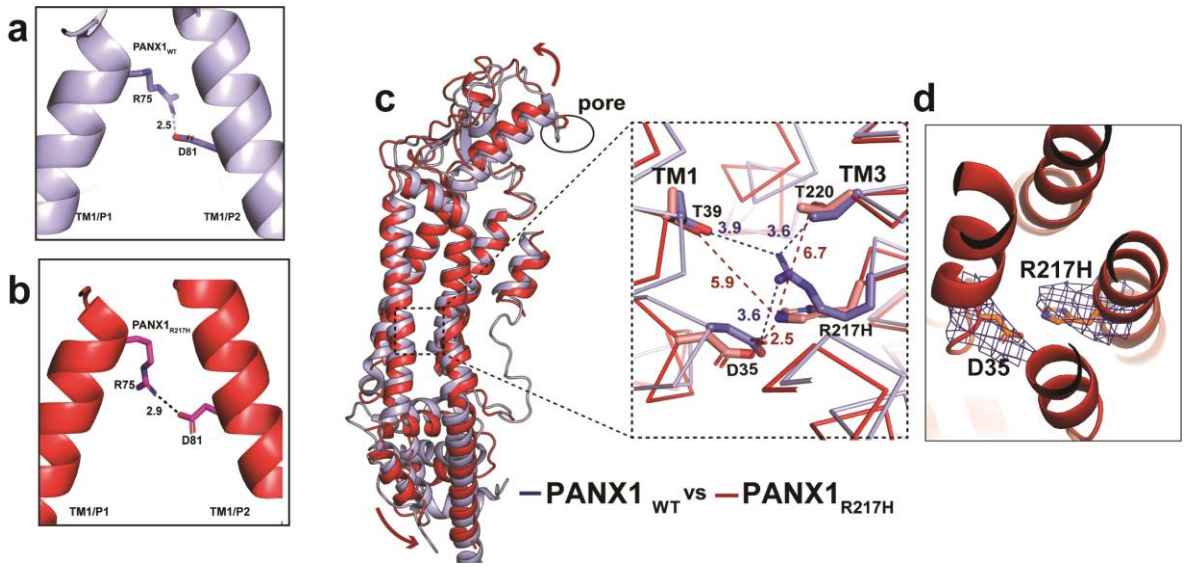

Fig. 4.8: a-b) R75 of one protomer (P1) interacts with D81 of another protomer (P2) **c)** The structural superposition of $PANX1_{WT}$ and $PANX1_{R217H}$ (Cα RMSD =1.2 Å for 288 atoms aligned) exhibits a disrupted hydrogen network, owing to the mutation, displayed in the inset; for clarity, only one subunit is shown, and arrows indicate the direction of the movement of the mutant in comparison to $PANX1_{WT}$. d) Density for interacting residues in $PANX1_{R217H}$ mutant (D35 and R217H) contoured at a 9.0 σ.

4.6 A mimic of Pannexin2 (PANX2) pore residues in PANX1

To understand the effect of extracellular gating residues on the channel structure and function, we intended to create charge reversal mutants of extracellular gate residues W74 and R75. Interestingly, a study by Ruan *et al*. showed PANX1 charge reversal mutants do not form correctly assembled PANX1(Fig.4.9)

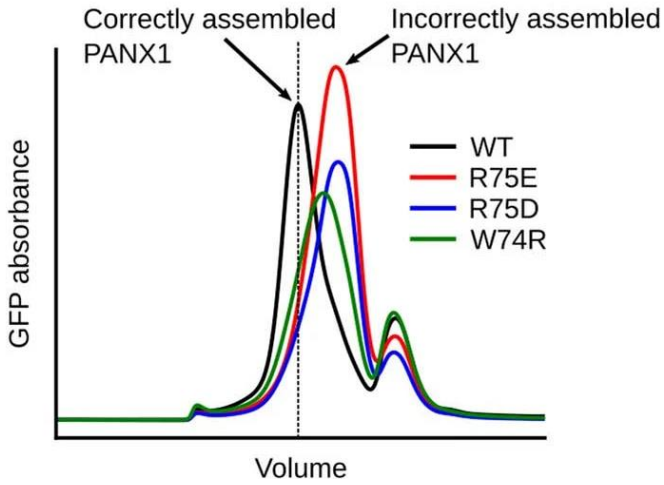

Fig. 4.9: FSEC profiles showing correct and incorrect PANX1 assemblies. The charge reversal mutant leads to the incorrectly assembled PANX1 compared to the $PANX1_{WT}$.[17].

.

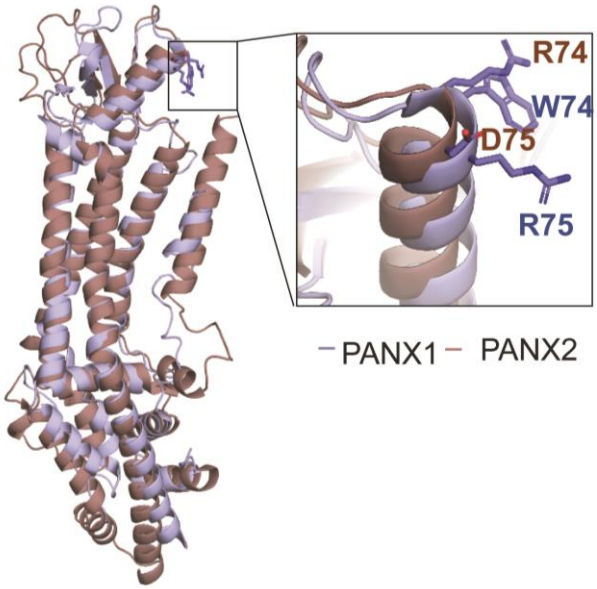

Fig. 4.10: Superposition of PANX2 (alphafold2 model)[139] and PANX1 (Cα RMSD =1.6 Å for 226 atoms aligned) suggests R74 and D75 are extracellular gating residues in PANX2, whereas the W74 and R75 are the pore gating residues in PANX1.

Comparing PANX2(Pannexin2) Alphafold2[139,140] model with PANX1 reveals R74 and D75 as the extracellular gating residues in PANX2 (Fig. 4.10)

4.7 Purification and structural determination of PANX1$_{DM}$.

Therefore, we generated a double mutant in PANX1 to mimic the extracellular gating residues of PANX2, W74R, and R75D. The PANX1 double mutant (PANX1$_{DM}$) was purified on a large scale using the Bacmam system described in the method section (Chapter 2). As seen in the SEC profile, mutating the extracellular residues leads to the destabilization of the protein. (Fig. 4.11)

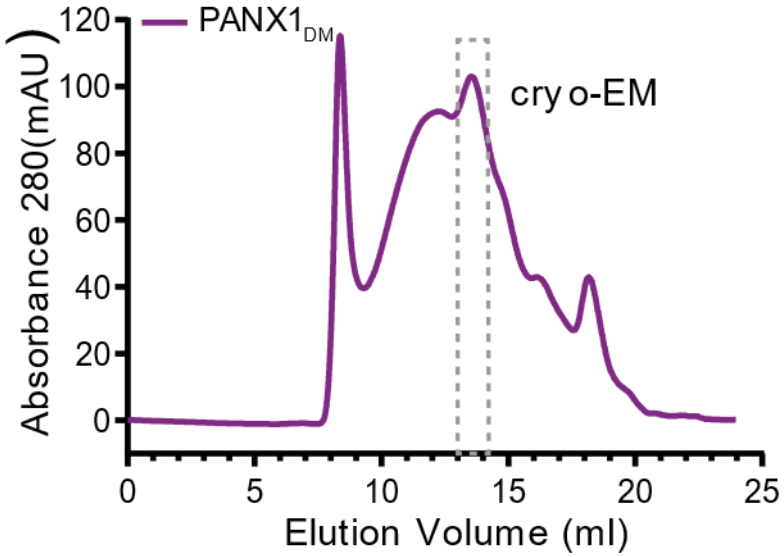

Fig. 4.11: SEC profile for PANX1 double mutant (PANX1$_{DM}$). The dashed line represents the fraction of the protein used for grid freezing.

Nonetheless, the peak corresponding to PANX1 was taken and concentrated to 5 mg/ml before grid freezing. The data was collected on Titan Krios (300 KeV) equipped with a Falcon 3 detector at a magnification of 75,000x. The data was processed in CryoSPARC (Fig. 4.12, Table 4.4)

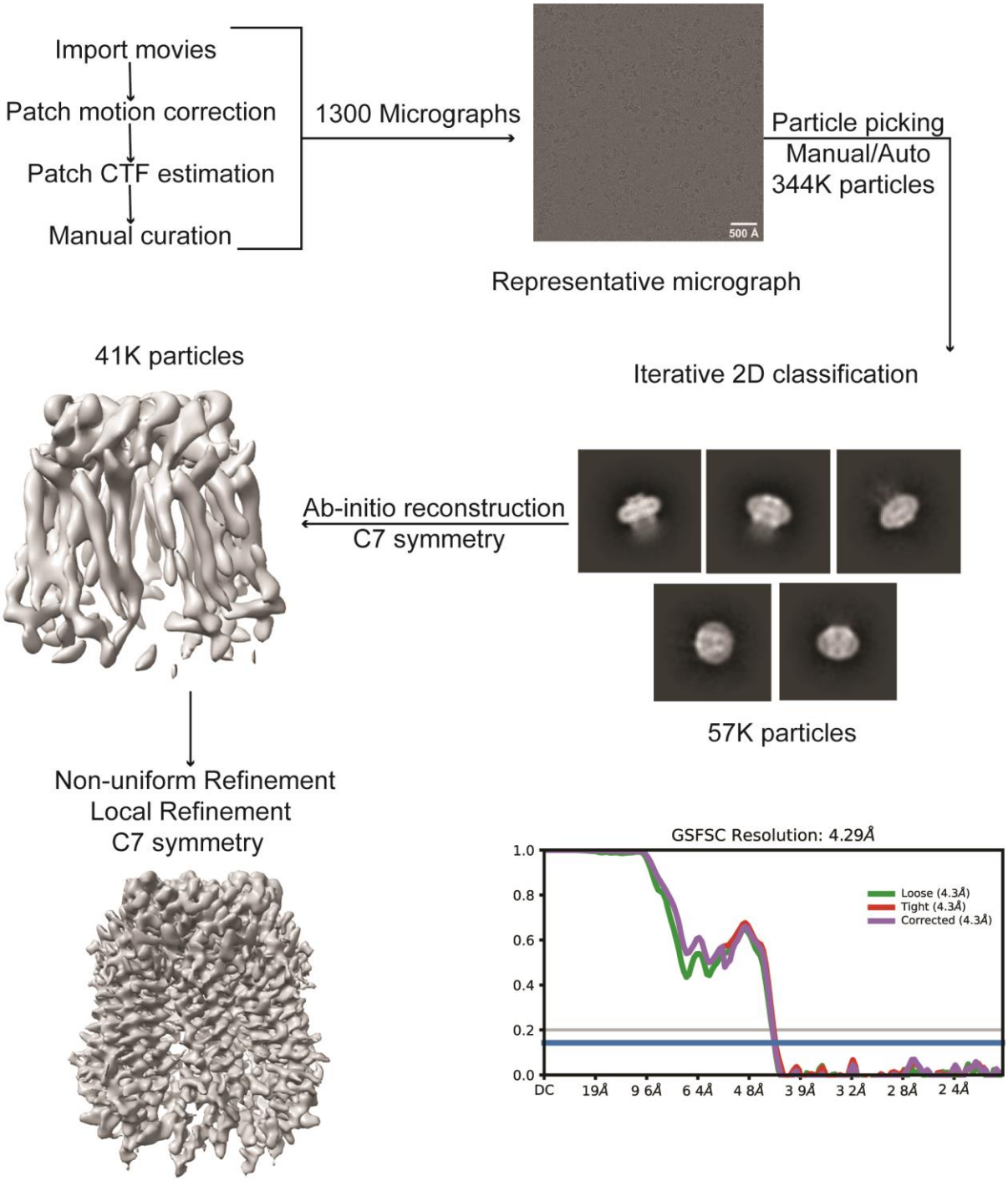

Fig. 4.12: Cryo-EM workflow for $PANX1_{DM}$ mutant.

Table 4.4: Cryo-EM data collection, refinement, and validation statistics

Construct Name	$PANX1_{DM}$ (EMD-34268)
Data collection and processing	
Magnification (x) Mode	75000 TEM
Voltage (kV) Detector Slit width (eV)	300 FalconIII -
Electron exposure (e^{-}/Å^2)	29.87
Defocus range (μm)	-1.8 to -3.3
Pixel size (Å)	1.07
Symmetry imposed	C7
Initial particle images (no.)	344639
Final particle images (no.)	41282
Map resolution (Å) FSC threshold	4.29 0.143
Refinement	
Initial model used (PDB code)	6WBF
Model resolution (Å) @ FSC 0.5	4.4
Map sharpening *B* factor (Å^2)	-141.1
Model composition Non-hydrogen atoms Protein residues Ligands	 16212 2156 -
B-factor (Å^2) Total Protein Ligands	 88.11 88.11 -
R.m.s. deviations Bond lengths (Å) Bond angles (°)	 0.004 1.049
Validation MolProbity score Clashscore Poor rotamers (%)	 1.76 10.64 0
Ramachandran plot Favored (%) Allowed (%) Disallowed (%)	 96.62 3.38 0

The mutants (R217H, DM) were modeled using a previously determined structure (PDB ID- 6WBF).

4.8 Structural features of PANX1$_{DM}$

To inspect the effect of the gating residues on the structure of the channel, we superposed the PANX1$_{WT}$ and PANX1$_{DM}$ (Fig. 4.13-a). The overall structure of PANX1$_{DM}$ is similar to PANX1$_{WT}$. However, a small movement in ECD, ICD, and TMD was observed, similar to the PANX1$_{R217H}$, although the movements were less pronounced.

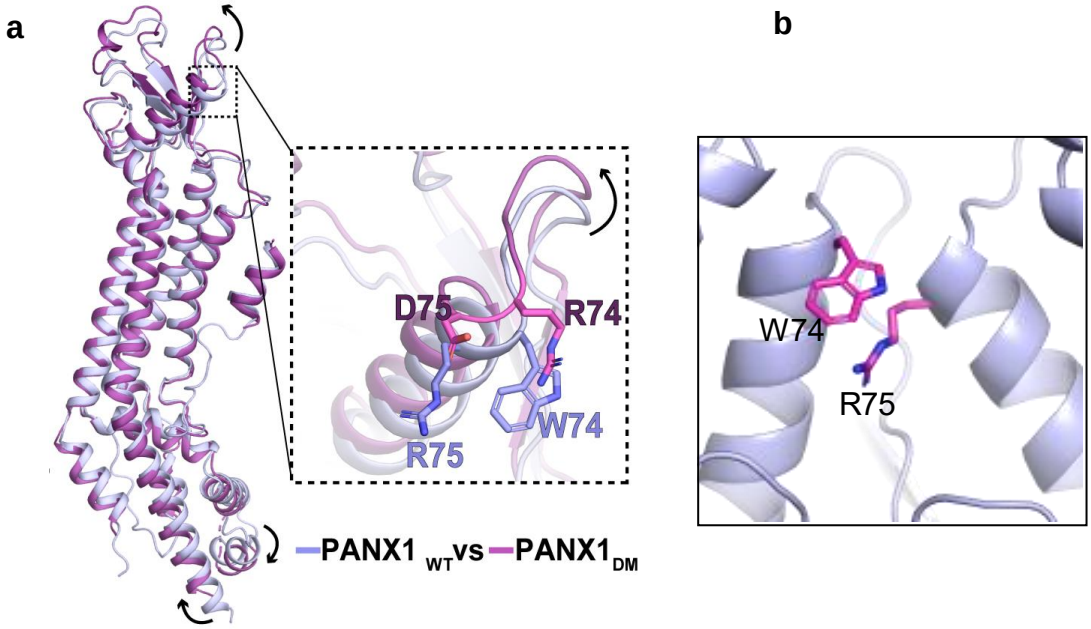

Fig. 4.13: a) Superposition of PANX1$_{WT}$ and PANX1$_{DM}$ (Cα RMSD = 0.9 Å for 282 atoms aligned) exhibiting pore gating residues in PANX1$_{WT}$ (W74, R75) and PANX1$_{DM}$ (R74, D75) **b)** NH-Cation-pi interaction in PANX1$_{WT}$ with a distance of 3.6 Å. NH-Cation-pi interaction in PANX1$_{WT}$ is eliminated in PANX1$_{DM}$ due to the replacement of the pore-gating residues.

The major inter-protomeric interaction in PANX1$_{WT}$ is the cation pi interaction between W74 and R75 and an H-bond between R75 and D81 (Fig. 4.13-b, 4.8-a). These interactions are lost in the PANX1$_{DM}$. However, the heptamer is stabilized by the H-bond interaction between R74 and D75 of adjacent protomers (Fig. 4.14-a). As these residues are present in PANX2 at the primary constriction, interaction between arginine and aspartate likely stabilizes the constriction in the PANX2 channel.

Interestingly, arginines in the $PANX1_{DM}$ form a highly positive charge environment at the first constriction and a narrower pore than $PANX1_{WT.}$ The pore diameter in the $PANX1_{DM}$ is reduced to 7.9 Å compared to 12.0 Å in $PANX1_{WT}$ (Fig. 4.14-b).

Both $PANX1_{R217H}$ and $PANX1_{DM}$ exhibit similar pore constrictions and long-range effects. A mutation in TM3 in $PANX1_{R217H}$ is translated towards closing the pore. Similarly, mutations in the pore affected the movement of ECD, TMD, and ICD in the $PANX1_{DM}$ channel.

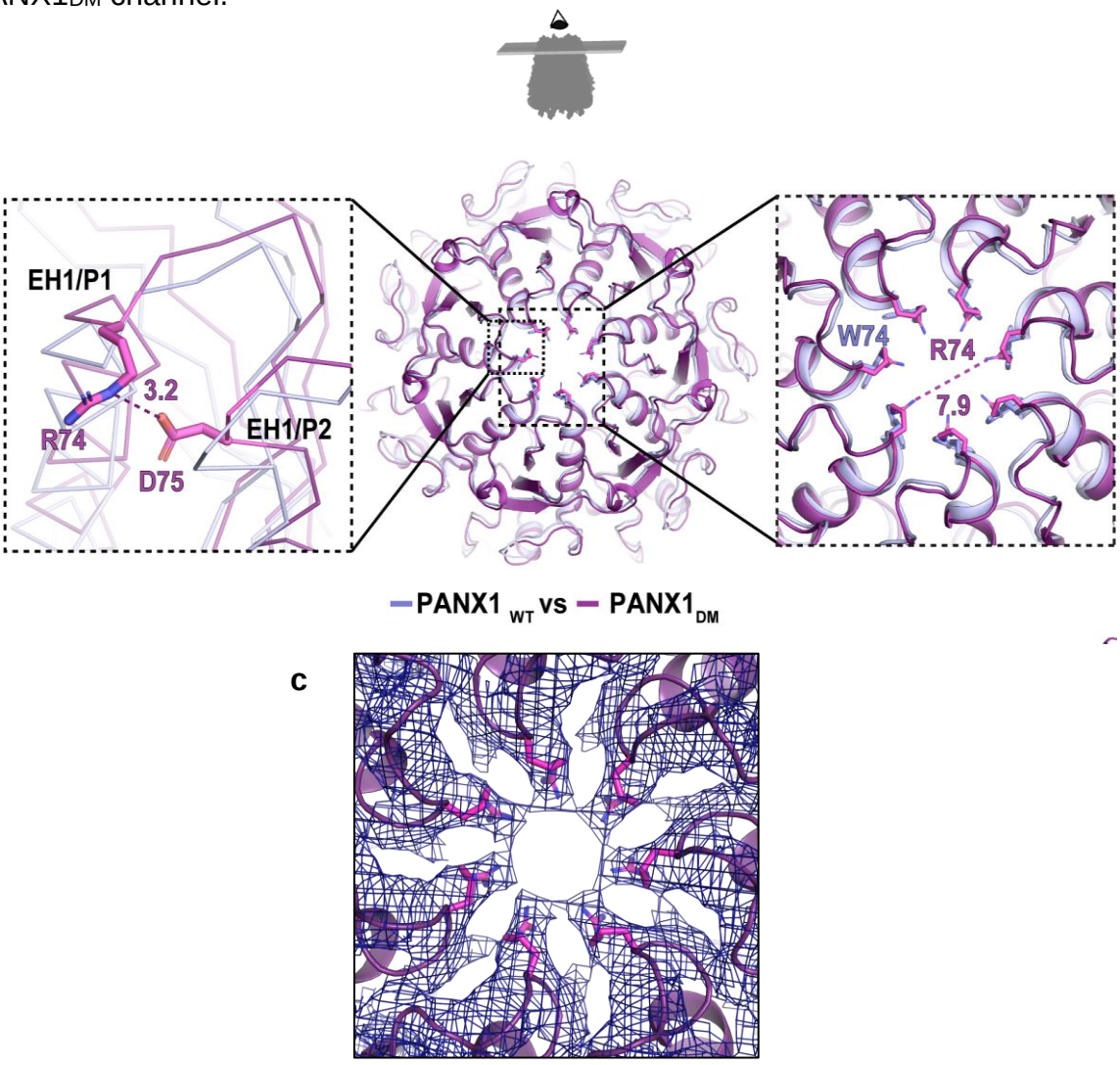

Fig. 4.14: A cross-section of superposed $PANX1_{WT}$ and $PANX1_{DM}$ **a)** the left inset displays the interaction between D75 of one protomer(P1) with R74 of another protomer(P2, **b)** The pore is partially closed (7.9 Å) in $PANX1_{DM}$ compared to $PANX1_{WT}$ (12.0 Å). **c)** The representative density for a pore gating residue R74 in $PANX1_{DM}$, contoured at a σ level of 7.5.

4.9 ATP binding studies of PANX1 mutants

The most common ATP binding motif, the Walker motif, is absent in PANX channels, making it difficult to recognize the residues involved in the binding of ATP. However, ATP release activity has been observed in both PANX1 and PANX3. Moreover, mutagenesis studies on PANX1 have suggested the role of R75 in ATP binding[165]. To map the ATP binding residues in PANX1/3, we identified a few positive charged residues based on the sequence conservation in PANX1 and PANX3 in their permeation pathway (Fig. 4.15 a-b). The mutations were generated in the $PANX1_{WT}$ by site-directed mutagenesis, and the sequence was confirmed through sanger sequencing.

a

List of mutants	Abbreviation
R75	$PANX1_{R75A}$
W74/R75	$PANX1_{DM}$/ W74R,R75D
R128	$PANX1_{R128A}$
K24	$PANX1_{K24A}$
R217	$PANX1_{R127H}$
PANX1	$PANX1_{WT}$

b

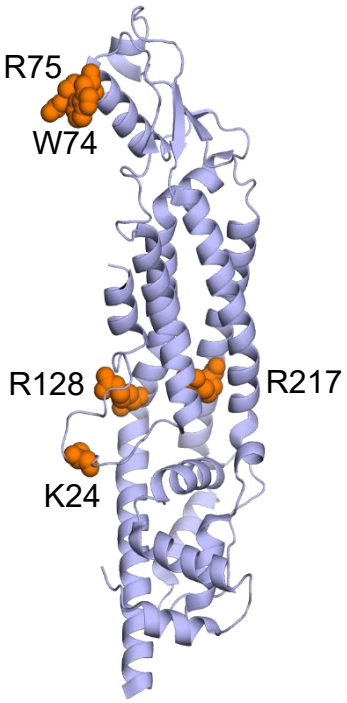

Fig. 4.15: a) List of mutants used for ATP binding in this study, **b)** Position of mutants in $PANX1_{WT}$ structure. R75, W74/R75 are located at the pore, R128 is in TM2, R217 is in TM3, and K24 is in N-terminus in $PANX1_{WT}$.

To start with the binding experiments, we used ATP as a ligand and performed MST with the $PANX1_{WT}$. The $PANX1_{WT}$ affinity with ATP was calculated to be 21 µM. However, ATP hydrolysis decreased the pH of the solution at higher concentrations, making it difficult to measure a proper binding affinity. To overcome these issues, we utilized ATP-γS, a non-hydrolyzable ATP analog, to compare the binding affinity between $PANX1_{WT}$ and the mutants. Moreover, the binding affinity calculated with ATP

and ATP- γS was in a similar range, suggesting that the ATP analog behaves similarly to the ATP(Fig. 4.16); thus, we used ATP-γS for our binding studies.

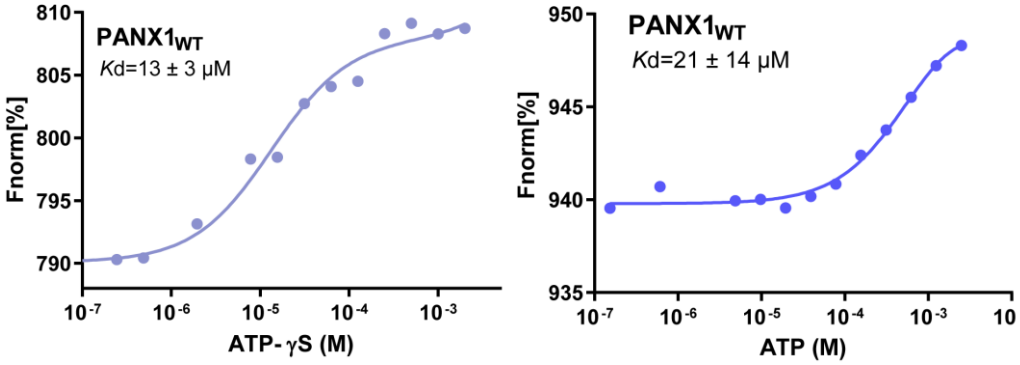

Fig. 4.16: MST studies for $PANX1_{WT}$ with ATP-γS and ATP. The binding affinity for ATP-γS, and ATP was determined as 13 and 21 µM, respectively.

To measure the binding affinity of PANX1 mutants with ATP-γS, we purified the PANX1 mutants on a large scale (Fig. 4.17).

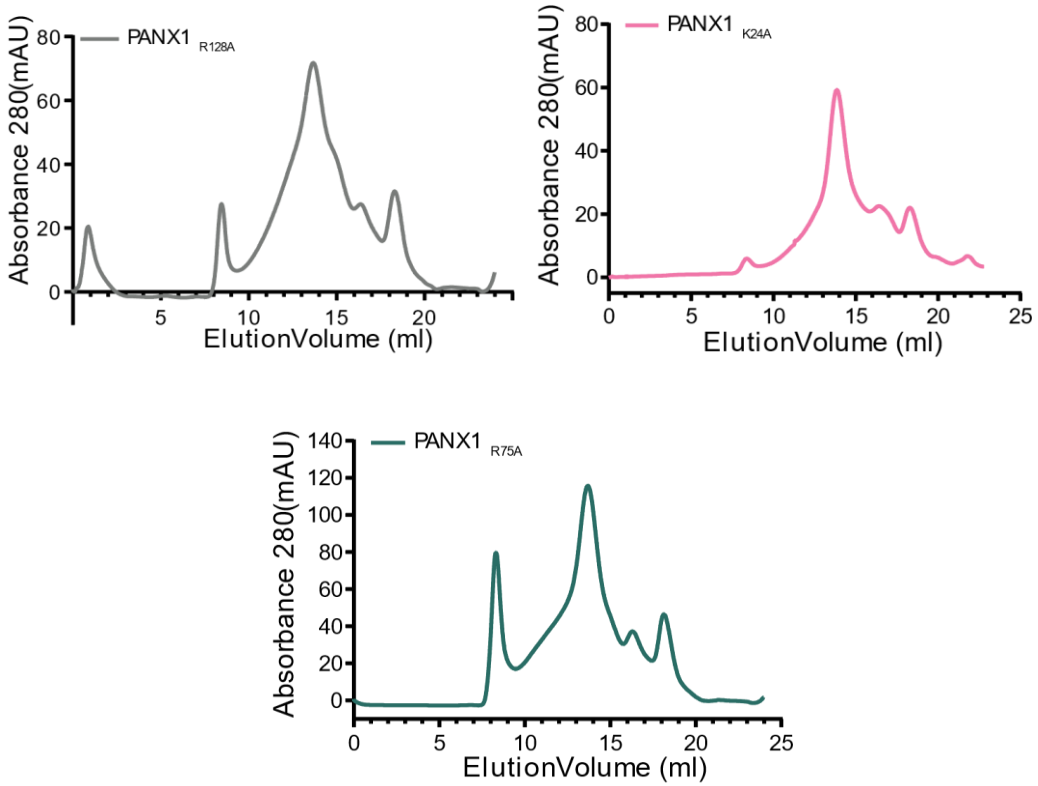

Fig. 4.17: SEC profile for the mutants used for ATP-γS binding studies run on a superose 6 column. The PANX1 channel elutes at 14-15 ml. A fraction (0.5 ml) containing the highest concentration was used for MST studies.

The purified protein was quantified, and the same amount (10 nM as the final concentration) of all the mutants was used for the experiments.

The K24A (N-terminus, Kd of 83 µM) substitution affected the interaction of ATP-γS with PANX1 leading to a lower affinity than the $PANX1_{WT}$ (Kd of 13 µM). Likewise, R75A and W74R/R75D (pore-gate mutants) had a binding affinity of 75 and 78 µM, respectively (Fig. 4.18).

The apparent binding affinity for the congenital mutant R217H (TM3) was calculated as 220 µM. Since a proper saturation was not achieved, an accurate value could not be measured (Fig. 4.18). Nevertheless, altering charged residues in the vestibule can affect the electrostatic surface of the PANX1 vestibule significantly, which can affect the binding of ATP-γS with the channel as observed in $PANX1_{R217H}$ (Fig. 4.6). Furthermore, R128A (TM2) substitution reveals a complete loss of ATP-γS binding, indicating the importance of the transmembrane region for ATP-γS interaction (Fig. 4.18).

Substitutions of positive charges in the TM helices around the vestibule, for instance, R217H and R128A, seem to influence the surface electrostatics within the vestibule.

In conclusion, we observed lower binding affinity for ATP-γS in the mutants studied. Though pore mutants and N-terminus mutants led to a decrease in affinity, residues in the transmembrane region affected the binding of ATP-γS to PANX1 to a greater extent.

However, it is difficult to conclude if these residues are directly involved in ATP binding or mask the ATP binding site by disrupting the local network and altering the charge in the permeation pathway, as observed in $PANX1_{R217H}$ (Fig. 4.8-b, 4.6).

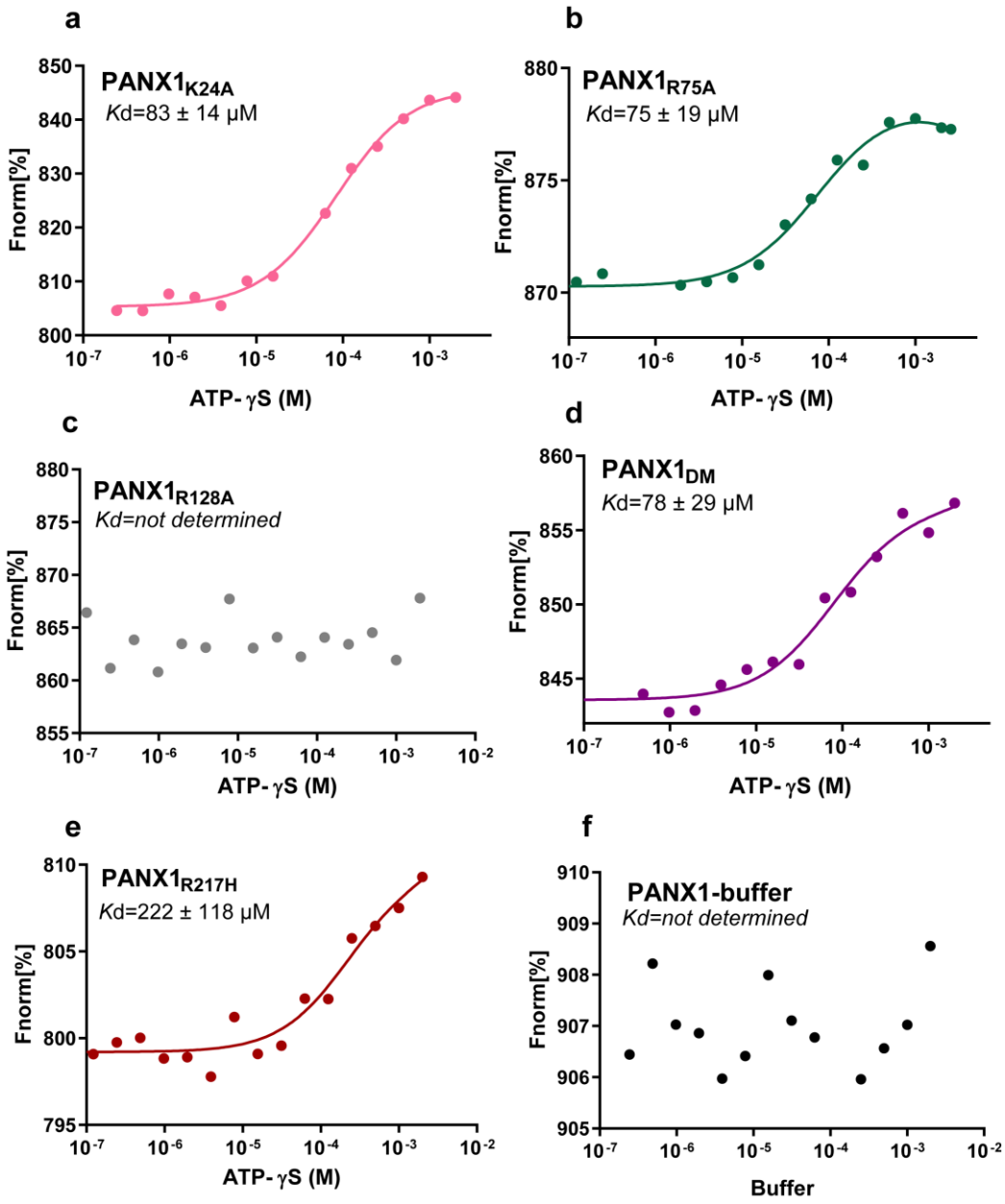

Fig. 4.18: MST studies for PANX1 mutants with ATP-γS**. a)** The N-terminus mutant, K24, shows a 4/5-fold reduction in ATP-γS binding affinity compared to $PANX1_{WT}$ (13 µM). **b-d)** Similarly, the ATP-γS binding affinity for the pore mutants ($PANX1_{R75A}$, $PANX1_{DM}$) was determined as 75 µM and 78 µM, respectively. **c)** The R128A mutant in TM2 exhibits a complete loss of binding. **e)** However, the congenital mutant R217H, located in TM3, did not show a complete saturation at the highest concentration of ATP-γS, suggesting a different behavior of the mutant channel compared to $PANX1_{WT}$. The calculated *K*d for the R217H mutant was 222 µM. However, as we did not get a proper saturation, it may not represent a correct value, making it difficult to compare the binding affinities between $PANX1_{WT}$ and $PANX1_{R217H}$. **f)** Buffer was kept as a negative control.

4.10 PANX1 congenital mutant (R217H) has weak voltage dependence

PANX1 are observed to be weakly voltage-dependent channels and are activated at positive potentials. The PANX1 congenital mutant was observed to have reduced current density compared to the $PANX1_{WT}$[102].

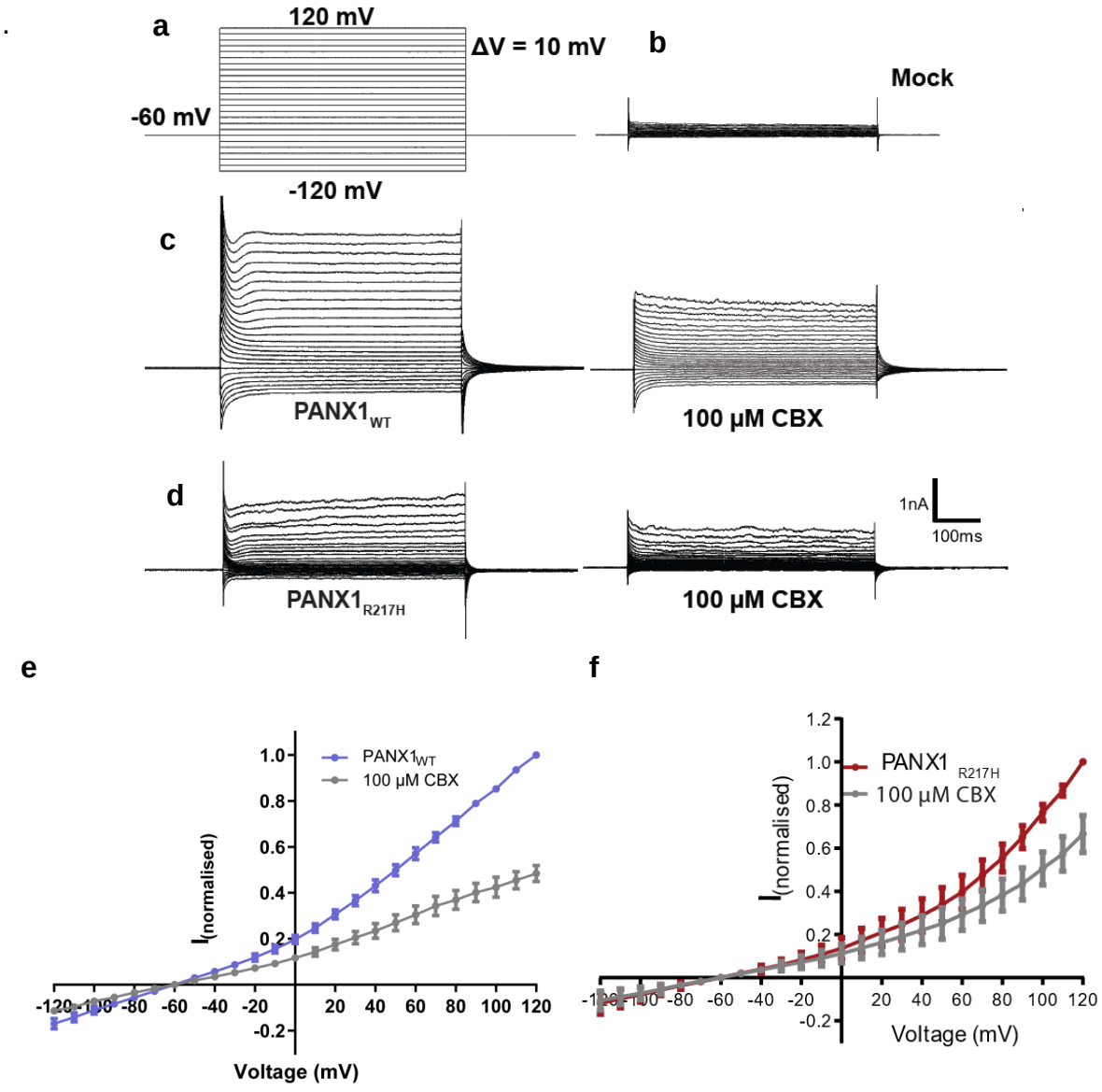

Fig. 4.19: a) The protocol used for patch clamp is shown, **b)** Mock recording with untransfected cells, **c-d)** Representative traces for whole-cell current for $PANX1_{WT}$ and $PANX1_{R217H}$, 100µM CBX was used to study the effect of the inhibitor on PANX channels. **e-f)** Current Voltage curve for $PANX1_{WT}$ and $PANX1_{R217H}$, each point represents the mean of n=6-8 individual recordings, and the error bar represents SEM.

We compared the current-voltage curve for $PANX1_{WT}$ and the mutant, $PANX1_{R217H,}$ and the effect on the carbenoxolone binding in response to the altered tryptophan geometry in $PANX1_{R217H}$.

The $PANX1_{WT}$ and the congenital mutant behaved similarly and were activated at positive potentials (Fig. 4.19 a-f).

Although PANX1 lacks a conventional voltage sensor domain in its structure, it possesses weak voltage dependence. We investigated if the arginine at 217 position can contribute to the weak voltage dependence in PANX channels. A stretch of arginine/lysine residues in voltage-gated channels has been observed to contribute to voltage dependence[27].

We calculated the V_{50} value from the G-V curve for the $PANX1_{WT}$ and the mutant channel. The $PANX1_{WT}$ exhibited half-maximal voltage at 36.92 mV and showed saturation at +120 mV (Table 4.5, Fig. 4.20).

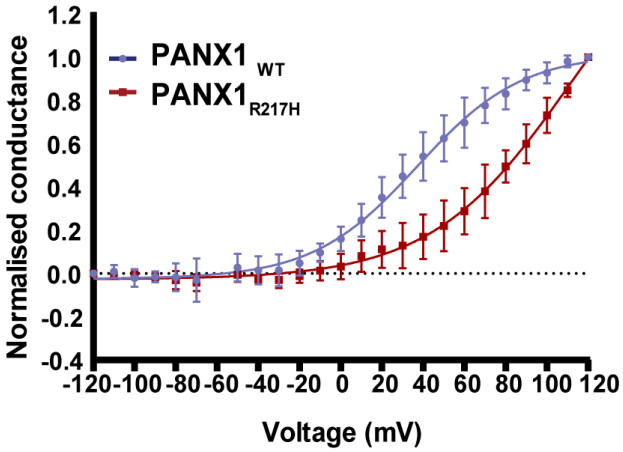

Fig. 4.20: G-V curve for $PANX1_{WT}$ and $PANX1_{R217H}$. Each point represents the mean of n=6-8 individual recordings, and the error bar represents SEM.

However, $PANX1_{R217H}$ did not reach saturation at +120 mV, and the HEK293 cells did not survive beyond +120 mV to accurately calculate the V_{50} for the mutant channel.

Table 4.5: V_{50} Values calculated for $PANX1_{WT}$ and $PANX1_{R217H}$

Constructs	V_{50}(mV)	Slope factor, k
$PANX1_{WT}$	36.92 ± 1.89	26.03 ± 1.7
$PANX1_{R217H}$	115.9 ± 18.55	35.63 ± 5.2

The G-V curve for the wild type and the mutant was fitted using the Boltzmann equation. The V_{50} for the mutant was four times higher than the $PANX1_{WT}$. Although the V_{50} calculated for the R217H mutant does not depict a very accurate value, the curve's values and shape suggest altered voltage dependence in the mutant channel (Fig. 4.20).

4.11 Pore residues do not affect the voltage dependence of the PANX1 channel

We also investigated the role of pore mutants $PANX1_{R75}$, and $PANX1_{DM,}$ in the voltage dependence of the PANX1 channels. We calculated the V_{50} from the G-V curve plotted for the mutants.

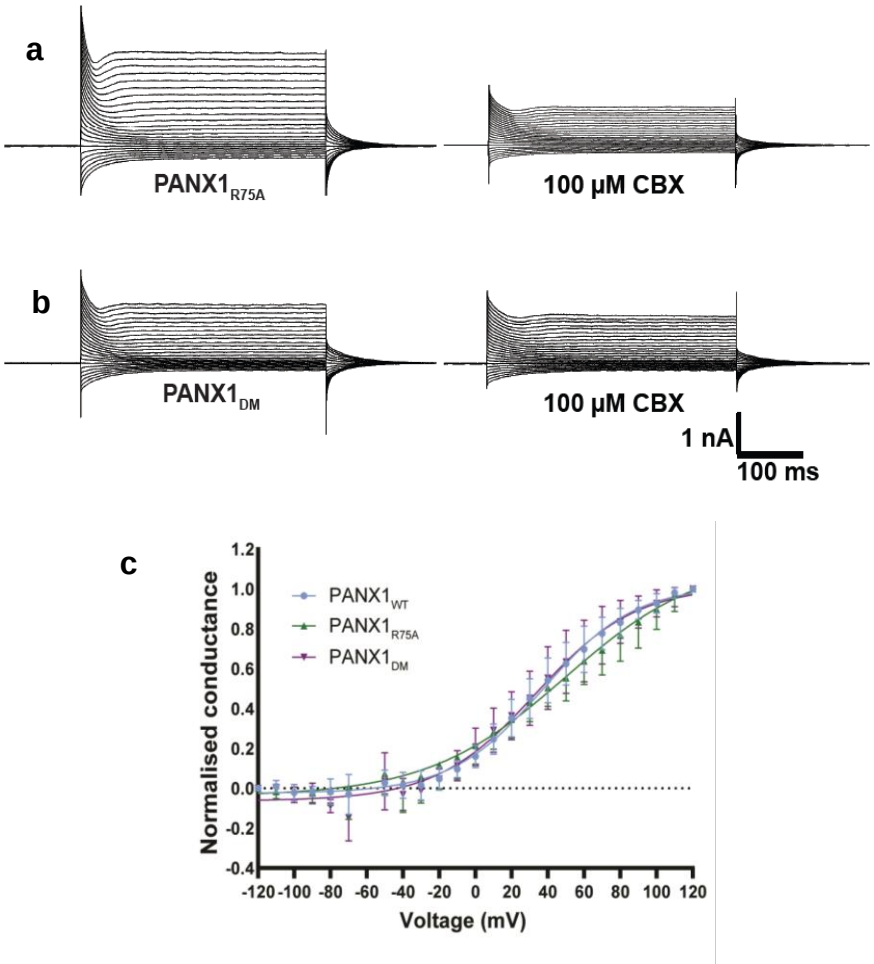

Fig. 4.21: a-b) Representative traces for whole-cell current for $PANX1_{WT}$, $PANX1_{R75A,}$ and $PANX1_{DM,}$ respectively, **c)** G-V curve plotted for pore mutants. Each point represents the mean of n=6-8 individual recordings, and the error bar represents SEM.

The curve was fitted using the Boltzmann equation. A comparison of the mutants revealed a similar range of V_{50} value for the mutants as the $PANX_{WT}$, suggesting that pore residues do not contribute to the voltage dependence observed in the PANX1 channel (Fig. 4.21, Table 4.6).

Table 4.6: V_{50} values calculated for $PANX1_{WT}$ and the mutants.

Constructs	V_{50}	Slope factor, k
$PANX1_{WT}$	36.92 ± 1.89	26.03 ± 1.7
$PANX1_{R75A}$	49.7 ± 6.72	38.17 ± 5.5
$PANX1_{DM}$	32.34 ± 3.96	29.47 ± 3.8

4.12 Current density in PANX1

We used patch-clamp electrophysiology experiments to investigate the effect of the mutation on the function of the channel. The current-voltage (IV) curves plotted for the mutant and the $PANX1_{WT}$ displayed outward rectification and decreased current amplitude in the mutant PANX1. We plotted the current density-voltage curve to understand if the decreased currents result from the mutant and not the expression of the protein. (As bigger cells are more likely to have higher expression)

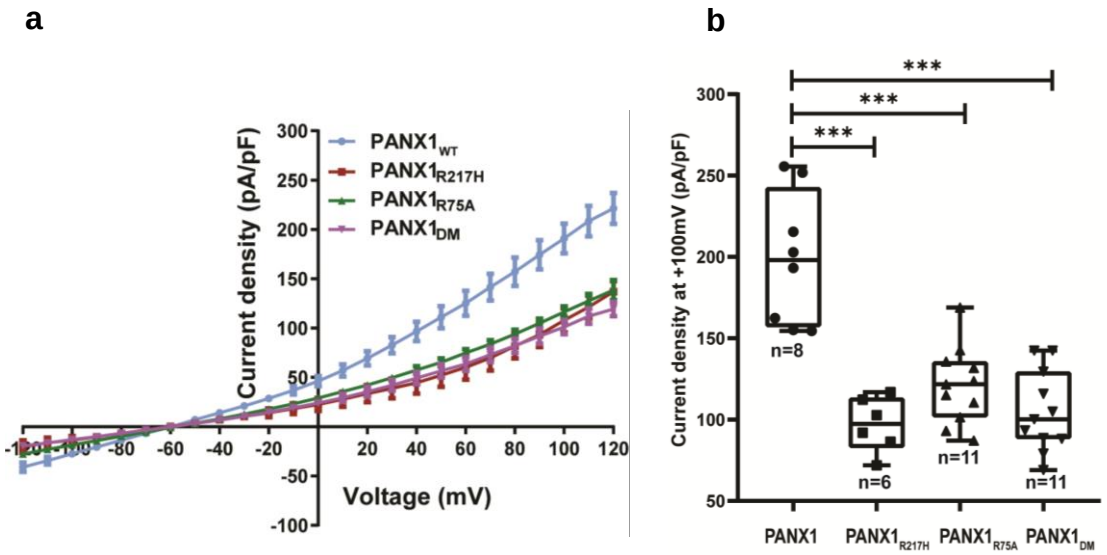

Fig. 4.22: a) Current density is plotted for the $PANX1_{WT}$(n=8), and the mutants, $PANX1_{R75A}$ (n=11), $PANX1_{R217H}$ (n=6), $PANX_{DM}$ (n=11), the error bar represents SEM. **b)**, Current density

box plot at +100mV for $PANX1_{WT}$ and the mutants; each point represents an individual recording.

Current densities (pA/pF) were obtained by dividing the steady-state current values(pA) by the cell membrane capacitance (pF). The current density accounts for cell size, allowing a proper comparison among mutants. The current density for the $PANX1_{WT}$ was twice that of the pore and congenital mutants, which can be a consequence of the reduced pore size as observed in $PANX1_{R217H}$ and $PANX1_{DM}$ (Fig. 4.7, 4.14, 4.22 a-b)

4.13 Inhibition of PANX currents by Carbenoxolone(CBX)

Carbenoxolone is the most commonly used blocker to attenuate PANX1 activity. A detailed study on carbenoxolone binding has been done by Michalski *et al*., where the authors suggested that the PANX1 activity is modulated through the first extracellular loop and revealed the role of W74 in carbenoxolone binding[99].

A study by Ruan *et al*. has shown the density of the carbenoxolone at W74 residue in the $PANX1_{WT}$ channel[17]. However, the density is not clear to fit the carbenoxolone perfectly, and the binding of CBX only at W74 remains controversial[166].

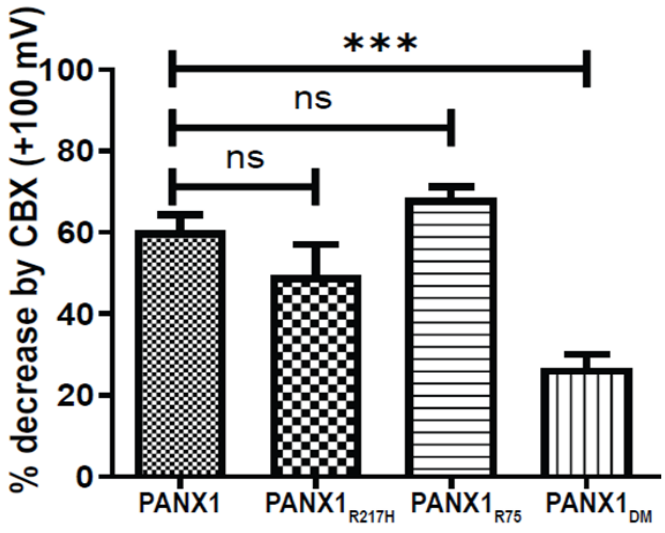

Fig. 4.23: Percentage inhibition by a PANX inhibitor, CBX plotted at +100mV for $PANX1_{WT}$ and the mutants. The number of recordings is mentioned in the parenthesis, error bar represents SEM. A two-tailed unpaired t-test is used for calculating the significance, ***p < 0.001; n.s., not significant.

In our study, we used 100 µM of CBX to attenuate the PANX1-sensitive currents. We did not observe any decrease in the CBX inhibition in $PANX1_{R217H}$ and $PANX1_{R75A}$ (Fig. 4.23). However, a significant decrease in PANX current inhibition was observed in $PANX1_{DM}$, suggesting a role of W74 in the CBX binding consistent with the previous observations[99].

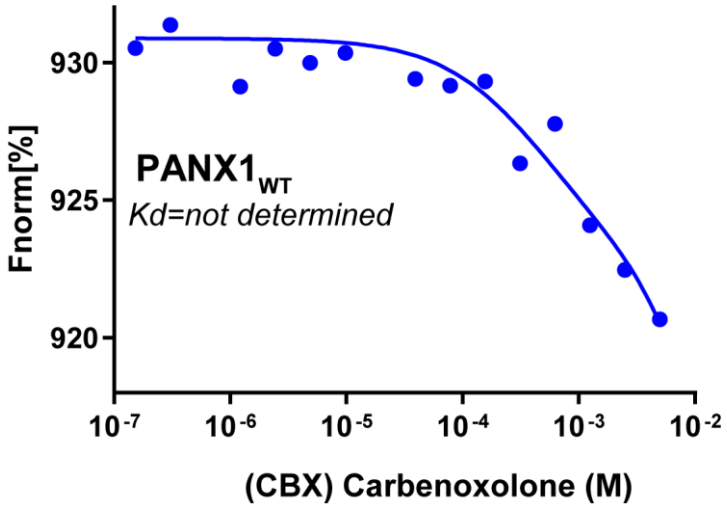

Fig. 4.24: Binding study of $PANX1_{WT}$ with carbenoxolone (CBX). As seen in the graph, saturation was not observed in $PANX1_{WT}$ even at a higher CBX concentration of 5 mM, making it difficult to estimate the binding affinity of $PANX1_{WT}$ with CBX.

Since we observed a decrease in the current inhibition by CBX in the double mutant, $PANX1_{DM}$, we measured the binding affinity of $PANX1_{WT}$ with CBX, which would help us describe a more definitive role of W74 in CBX binding.

As seen from Fig. 4.24, we could not get a saturation even at a higher CBX concentration of 5mM. It is plausible that CBX being a sterol, could interact with the detergent micelles making it unfeasible to measure binding affinity through MST.

4.14 Summary

The ATP-release channel PANX1 is involved in paracrine signaling. The substitution of arginine with histidine reduces channel activity and is associated with dysfunction in multiple organs. We observed that the expression of the R217H mutant channel is comparable to that of $PANX1_{WT}$, indicating that reduced functional activity is not a result of compromised protein expression. We optimized the Cryo-EM data processing parameters for the mutants and determined the structure of $PANX1_{R217H}$ at a moderate

resolution of 3.9 Å. The mutant channel exhibits a 1.5-2 Å outward shift of extracellular domains and an inward shift of intracellular domains. These movements results in an elongation of the transmembrane domain (TMD). The R217H mutation in $PANX1_{WT}$ causes the TMD to become more elongated, resulting in a straightening of the TMD. The most notable structural alteration in the mutant channel is the reduction in pore diameter from 12 to 8.2 Å. To better comprehend the function of the pore residues in PANX1, we generated a double mutant of pore residues in PANX1. The structure of the PANX1 double mutant (W74R, R75D) was determined at resolutions of 4.3 Å. These mutant residues mimic the pore-gating residues of PANX2.

At the first constriction of $PANX1_{DM}$, arginines generate a highly positive charge environment and reduce the pore radius by 4 Å.

Despite the fact that $PANX1_{R217H}$ and $PANX1_{DM}$ have comparable pore constrictions and long-range effects, the interactions in the primary constriction to stabilize the heptamer are significantly different.

In addition to investigating the structural changes caused by the mutations, we wanted to understand the functional effects of these mutations on the channel. We measured the mutants' voltage dependence and ATP-γS binding affinities and compared them to the $PANX1_{WT}$.

The calculated binding affinities of the charged mutants with an ATP analog revealed a decrease in affinity relative to the $PANX1_{WT}$, indicating that these residues are involved in ATP interactions. The pore residues of PANX1 play no role in voltage sensing, as demonstrated by patch clamp experiments. However, the measured conductance of $PANX1_{R217H}$ indicates that arginine plays a role in the channel's voltage dependence.

The results, therefore, provide a rationale for the debilitating effects of PANX1 congenital mutant owing to its inactivation by R217H mutation.

CHAPTER 5

Structural and functional comparison of Pannexin1 and 3 isoforms

5.1 Introduction

Pannexin3 (PANX3) is the smallest isoform, shares 42 % identity with PANX1, and mainly resides in the plasma membrane[26]. It is a major candidate for calcium homeostasis and regulates osteoblast differentiation through its ER calcium channel activity[81,87,115]. PANX3 is involved in many processes, such as the differentiation and proliferation of odontoblast, wound healing, and skin development. PANX3 also plays an important role in skeletal formation and development, odontoblast differentiation, and growth of metatarsals through its ATP and calcium release activity observed in mice models[81,86,87,115,116,167].

Like PANX1, PANX3 is N-glycosylated at the extracellular loop (EL). However, N-glycosylation in PANX3 occurs at EL1 instead of EL2 in PANX1. Although PANX1 and 3 have distinct localizations, they share a similar topology and heptameric organizations and are involved in releasing ATP from the cells. Post-translational modification, such as phosphorylation, has been observed to modulate both isoforms[80,81].

In this chapter, we aim to determine the structure of PANX3 in the presence of high extracellular K^+, speculated to open the channel and ATP release. The structural insights into the channel would aid in highlighting differences in PANX isoforms.

5.2 PANX3 purification optimization

The PANX3 gene was synthesized by Geneart (Invitrogen) and was subcloned into a pEG-Bacmam vector between Not1 and EcoR1 restriction sites. The GFP was cloned at the C-terminus of PANX3, and for the cleavage of GFP, tev protease and thrombin sites were inserted between the PANX3 gene and GFP.

5.2.1 PANX3 detergent screening

To assess the quality of the expressed protein, the Bacmam vector containing PANX3 (2µg) was transfected into HEK293 $GNTI^-$ cells at a density of $1*10^6$ cells/ml.

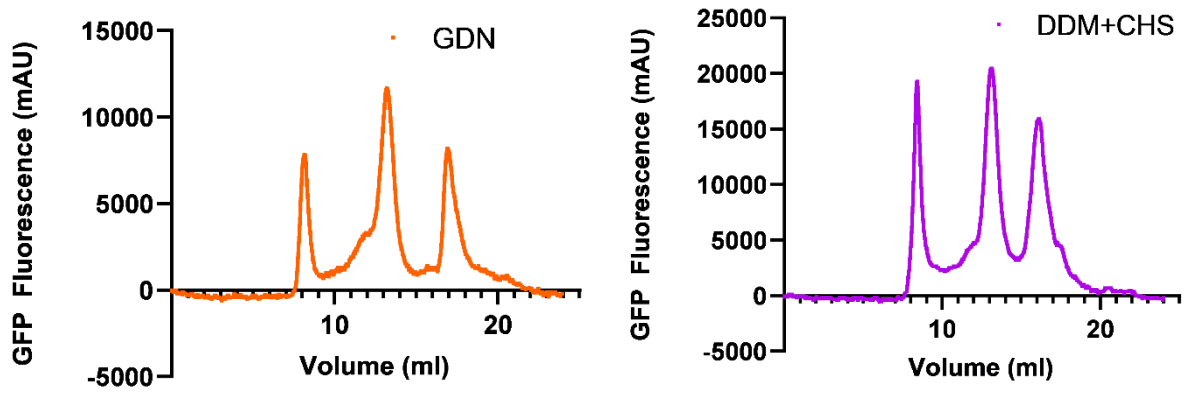

Fig. 5.1: FSEC profile for PANX3 run on superose 6 column solubilized in **a)** 10 mM GDN, **b)** 20 mM DDM. PANX3 shows similar quality in both detergents.

The transfected cells were solubilized in Tris pH 8.0, 100 mM KCl, 0.1 % PMSF, 20 mM DDM, or 10 mM GDN detergent (200 µl). The crude lysate was run on a superose 6 column, and the GFP fluorescence was monitored.

The protein quality (homogeneity) was similar in both the detergents (Fig. 5.1). As mentioned in chapter 3, GDN has low extractability compared to DDM, so we used DDM+CHS for large-scale PANX3 solubilization and purification.

5.2.2 Large-scale purification of PANX3

For large-scale purification, 2.4 liters of HEK293 GnTI$^-$ cells were infected with the virus. After infection, sodium butyrate was added at a final concentration of 5 mM. The cells were harvested 60 hours post-infection and resuspended in resuspension buffer (Tris pH 8.0, 100 mM KCl, 0.1% PMSF). The isolated membranes were solubilized in resuspension buffer containing 1% glycerol, 20 mM DDM, and 2mM CHS (final concentration). The protein was eluted in resuspension buffer, 1% glycerol, 2 mM DDM +0.2 mM CHS and 250 mM imidazole.

The eluted protein was kept for GFP cleavage using thrombin protease in a ratio of 1:50 by weight (thrombin: PANX3). SEC was used to remove the cleaved GFP and to get a clean PANX3 protein (Fig. 5.2). As seen in Fig. 5.2, the protein quality and quantity were not good enough to freeze the grids. Since the protein quality was not good when extracted in the detergent, we tried to use SMALPs

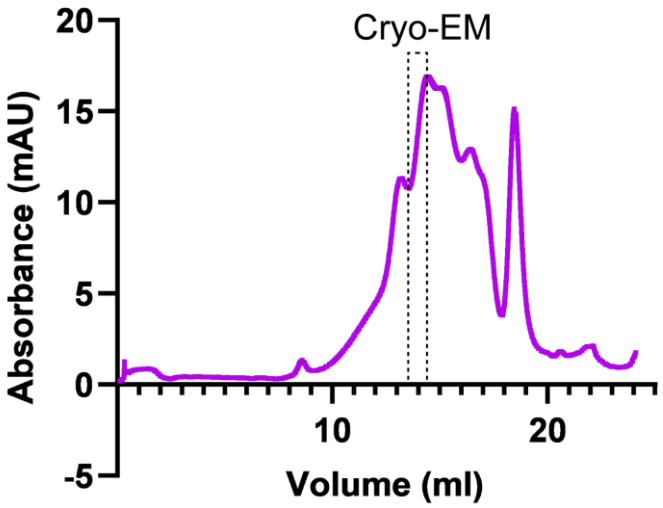

Fig. 5.2: SEC profile for PANX3 purified in DDM +CHS, run on a superose 6 column. The dashed line indicates the fraction used for Cryo-EM.

5.2.3 Purification by SMALPs

The membrane proteins are extracted and purified in detergents to understand their functional and structural properties. Although detergent extraction is a traditional method for the purification of membrane proteins, the detergents can strip off the essential lipids from the membrane protein required for solubilization.

SMALPS are styrene-maleic acid (SMA) *co*-polymers that can directly extract the protein from the membrane, thus eliminating the detrimental effect of the detergent on the membrane proteins[168,169]. Alternatively, SMALPs can be used after extracting the protein in the detergent. In the recent past, SMALP has been used to successfully purify membrane proteins, including small membrane proteins and large pore channels[17,168–171]. As we failed to achieve a good quality protein in detergent, we employed SMALP as it might stabilize the PANX3 channel.

To obtain a better quality protein, we used the previously extracted protein in DDM and exchanged it with 1% SMALPS (SMA30010). The protein was exchanged for 2 hours at 4 ℃ on end-to-end rotation. The protein was then kept on Ni- NTA binding for two hours. Post binding, the protein was eluted in elution buffer (Tris pH 8.0, 100 mM KCl, 1% glycerol, and 250 mM imidazole)

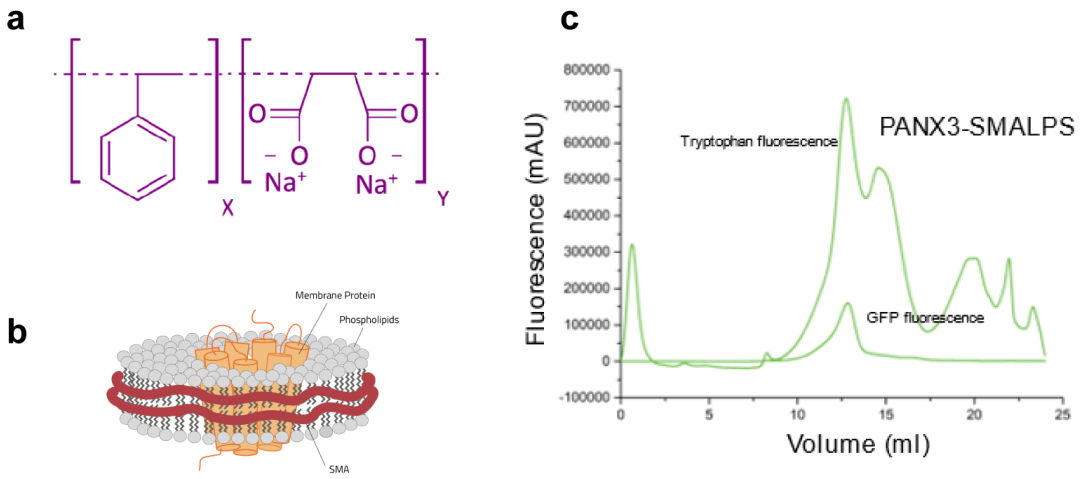

Fig. 5.3: a) Chemical structure of Styrene Maleic Acid copolymer(SMA)[172], **b)** This copolymer stabilizes the membrane protein by providing bicelles wrapped around lipid bilayer to form a disc-like structure[173], **c)** FSEC profile for PANX3 solubilized in SMALP (SMA30010). The PANX3 shows better quality when GDN is exchanged to SMALPS.

The quality of the eluted protein was inspected on FSEC using superose 6 columns (Fig. 5.3). As the protein behaved better in SMALPS than in detergent, we further purified the PANX3 through SEC at a large scale in SMALPS (Fig. 5.4-a)

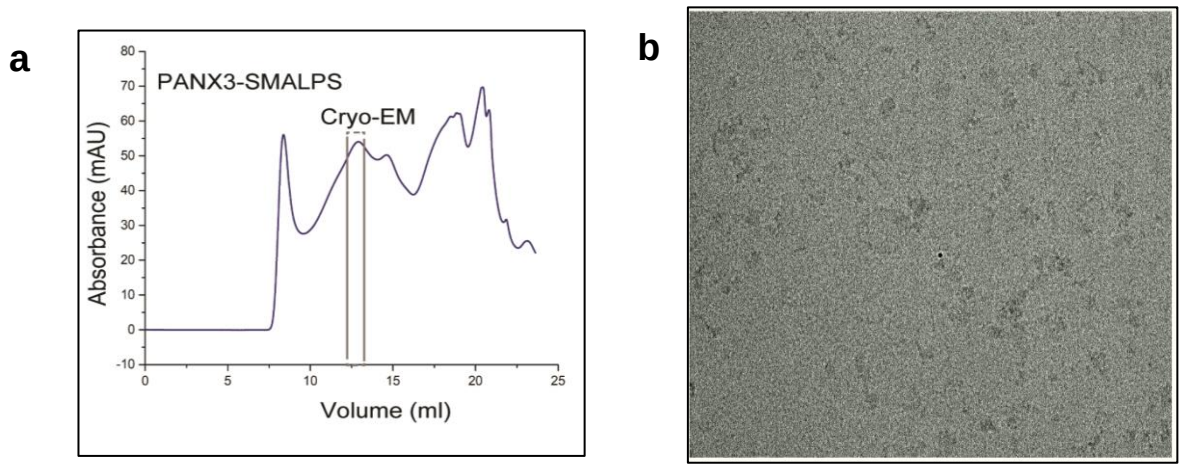

Fig. 5.4: a) SEC profile for PANX3 purified in SMALP (SMA30010). PANX3 is not stable in SMALPS when purified on a large scale. The dashed line indicates the fraction used for the grid freezing, **b)** The representative micrograph shows the denatured PANX3. The data was collected with a K2 direct electron detector.

Although PANX3 behavior was better in SMALPS than DDM detergent on a small scale, PANX3 disintegrated into multiple species during large-scale purification. However, we took the main fraction corresponding to PANX3 for grid freezing. The

1.2/1.3 gold grids were frozen with 3.5 seconds of blotting time, optimized for PANX1. As shown in Fig. 5.4-b, the PANX3 particles are not stable on the grid and are completely denatured. In conclusion, PANX3 is not stable in DDM or SMALPS.

5.2.4 PANX3 purification in GDN

During the small-scale detergent screening, we observed that the PANX3 protein behaved similarly in DDM and GDN (Fig. 5.1). We purified the PANX3 on a large scale using GDN to extract the protein from the membranes.

The cells were harvested 60 hours post-infection and resuspended in resuspension buffer (Tris pH 8.0, 100 mM KCl, 0.1% PMSF). The isolated membranes were solubilized in a resuspension buffer containing 1% glycerol and 10 mM GDN (final concentration). The protein was eluted in resuspension buffer, 1% glycerol, 100 µM GDN, and 250 mM imidazole.

The eluted protein was incubated for GFP cleavage using thrombin protease in a ratio of 1:50 by weight (thrombin: PANX3). The protein was further purified in SEC buffer (25 mM Tris pH 8.0, 100 mM KCl, 1% glycerol, and 50 µM GDN).

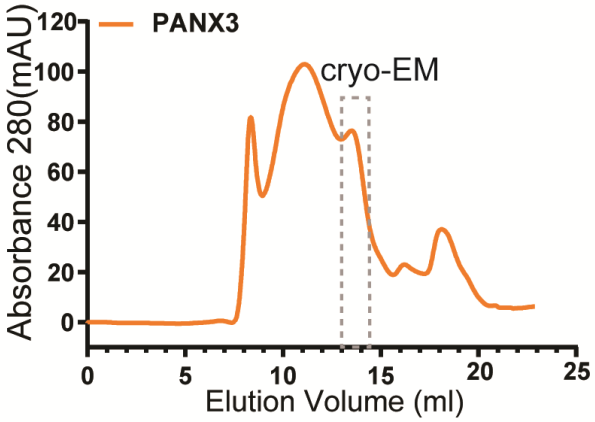

Fig. 5.5: SEC profile for PANX3 solubilized in GDN detergent. The dashed line indicates fractions used for single-particle Cryo-EM analysis.

Although the quality of PANX3 protein is better in GDN than in DDM, we could not get a homogenous protein. Nevertheless, we used the fraction corresponding to the PANX3 for grid freezing. The PANX3 protein was concentrated to 5 mg/ml before freezing in liquid ethane. The grids were kept in liquid nitrogen until further use (Fig.

5.5). The grid parameters optimized for PANX1 were used for freezing PANX3 grids. The data was collected on Titan Krios (300 KeV) equipped with a K2 electron detector at a magnification of 130,000x and a pixel size of 1.065 Å.

5.3 Structure determination

Post manual curation, ~800 micrographs were used for particle picking and 2D classification.

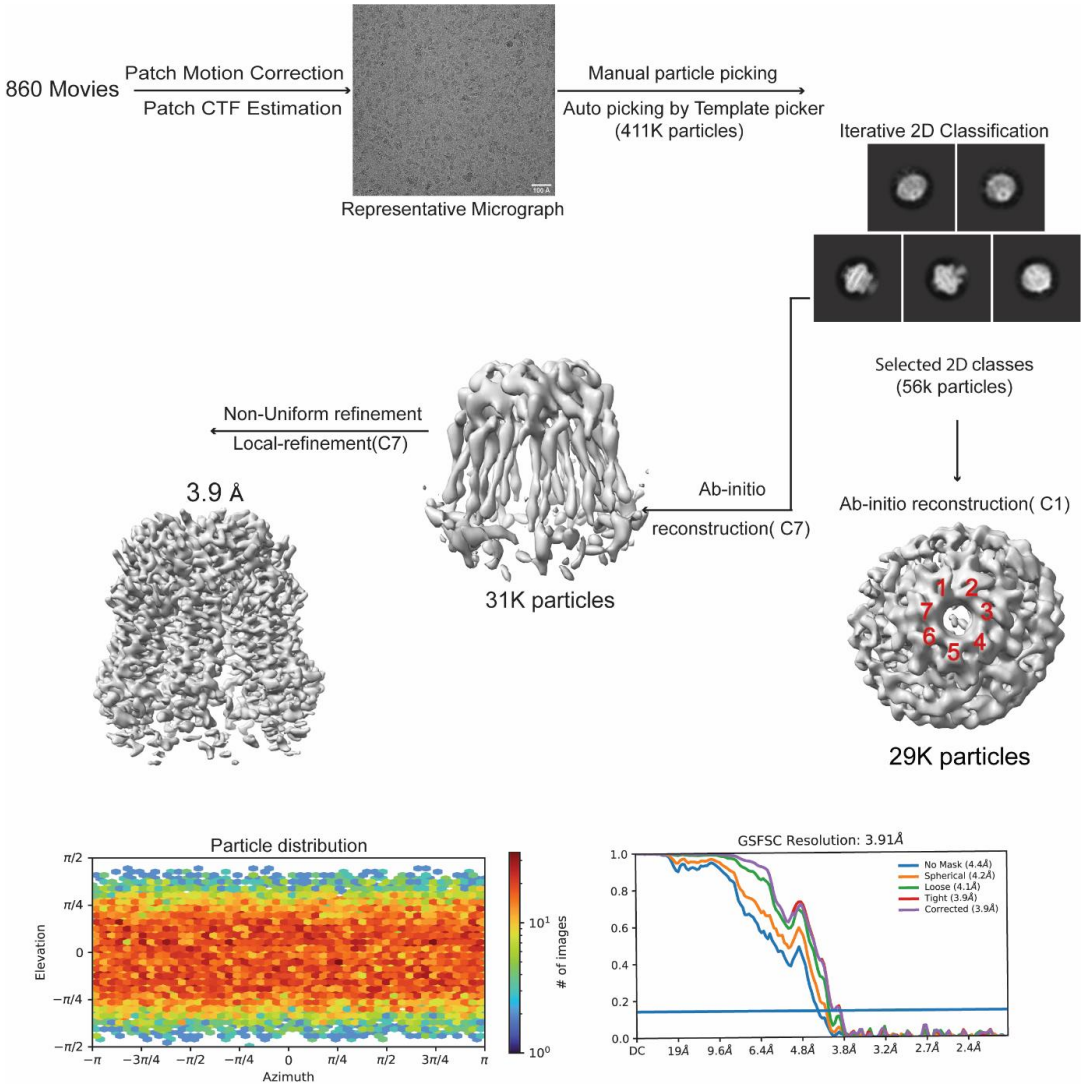

Fig. 5.6: Cryo-EM data processing workflow for PANX3 structure determination.

For the 3D ab-initio reconstruction, C1 symmetry was applied as we did not have any top views depicting the oligomeric composition of PANX3, unlike PANX1, where the

top and bottom views during the 2D classification suggested that PANX1 has a C7 symmetry (Chapter3).

Table 5.1: Cryo-EM data collection, refinement, and validation statistics

Construct Name	PANX3 (EMDB-34265) (PDB 8GTR)
Data collection and processing	
Magnification (x) Mode	130000 EFTEM
Voltage (kV) Detector Slit width (eV)	300 K2 20
Electron exposure (e^{-}/Å^2)	48.8
Defocus range (μm)	-1.8 to -3.3
Pixel size (Å)	1.07
Symmetry imposed	C7
Initial particle images (no.)	411263
Final particle images (no.)	31517
Map resolution (Å) FSC threshold	3.91 0.143
Refinement	
Initial model used (PDB code)	Alphafold2
Model resolution (Å) @ FSC 0.5	4.2
Map sharpening *B* factor (Å^2)	-143.6
Model composition Non-hydrogen atoms Protein residues Ligands B-factor (Å^2)	 16975 2156 7 (NAG) 7 (PTY)
Total Protein Ligands	70.00 70.57 42.92 (NAG) 46.01 (PTY)
R.m.s. deviations Bond lengths (Å) Bond angles (°)	 0.004 1.011
Validation MolProbity score Clashscore Poor rotamers (%)	 1.75 7.7 0
Ramachandran plot Favored (%) Allowed (%) Disallowed (%)	 95.3 4.7 0

3D Ab-initio reconstruction of PANX3 revealed a clear heptameric composition suggesting that, like PANX1, PANX3 also forms a heptamer (Fig. 5.6). To improve the resolution of the 3D reconstruction, we used the PANX3 ab-initio reconstruction and performed non-uniform refinement using C7 symmetry. The final PANX3 structure was determined at a resolution of 3.9 Å. Although we had a moderate resolution to build the side chains in most regions, we collected one more dataset to improve the resolution.

As evident in the SEC profile (Fig. 5.5), PANX3 is not homogeneous, which can affect the quality of particles on the grids and, consequently, the achievable resolution. To circumvent this problem, PANX3 was purified in the presence of calcium using GDN as the detergent. As PANX3 plays a significant role in calcium homeostasis, we hypothesized that calcium could assist us in achieving a more homogeneous PANX3 channel population[115].

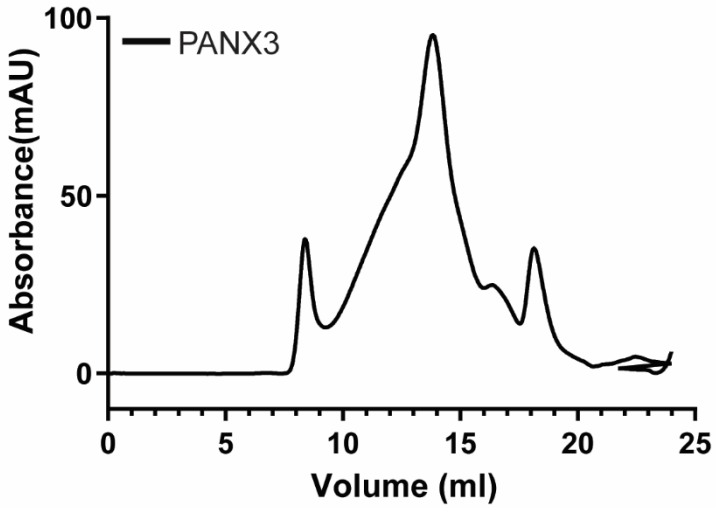

Fig. 5.7: SEC profile for PANX3 solubilized in GDN detergent and purified in the presence of calcium. The PANX3 shows improved quality of SEC profile when purified in the presence of calcium.

As the PANX3 SEC profile improved substantially when purified in the presence of calcium (Fig. 5.7), we froze the grids and collected the data on a Titan Krios (300 KeV) equipped with a K2 electron detector at a magnification of 130,000x. However, we could not achieve a 3D reconstruction at a higher resolution after processing the

dataset. Thus, we utilized the 3.9 Å resolution 3D reconstruction to build the PANX3 model.

5.4 PANX3 has altered structural features

The PANX3 shares 42% sequence identity with PANX1. Despite the high sequence conservation with its isoform, PANX3 displays distinct structural features and localization compared to PANX1.

We determined the structure of PANX3 to an overall resolution of 3.9 Å by Cryo-EM in the presence of ATP. The PANX3 was purified in the presence of K^+, suggesting that the structure modeled into the density is most likely an open conformation of the channel, as high potassium leads to the opening of the channel[51,146,174]. The density at the pore and transmembrane helices allowed the proper modeling of the side chains in these regions. The intracellular helices (160-185) and the C-terminus (373-392) lack clear densities, likely due to inherent flexibility in this region.

The PANX3 protomers retain the heptameric oligomer assembly that can be partitioned into an extracellular domain (ECD), transmembrane domain (TMD), and intracellular domain (ICD), similar to $PANX1_{WT}$ (Fig. 5.8a). Unlike other large-pore ion-channels like CALHMs[175], the PANX isoforms do not display heterogenous oligomeric association.

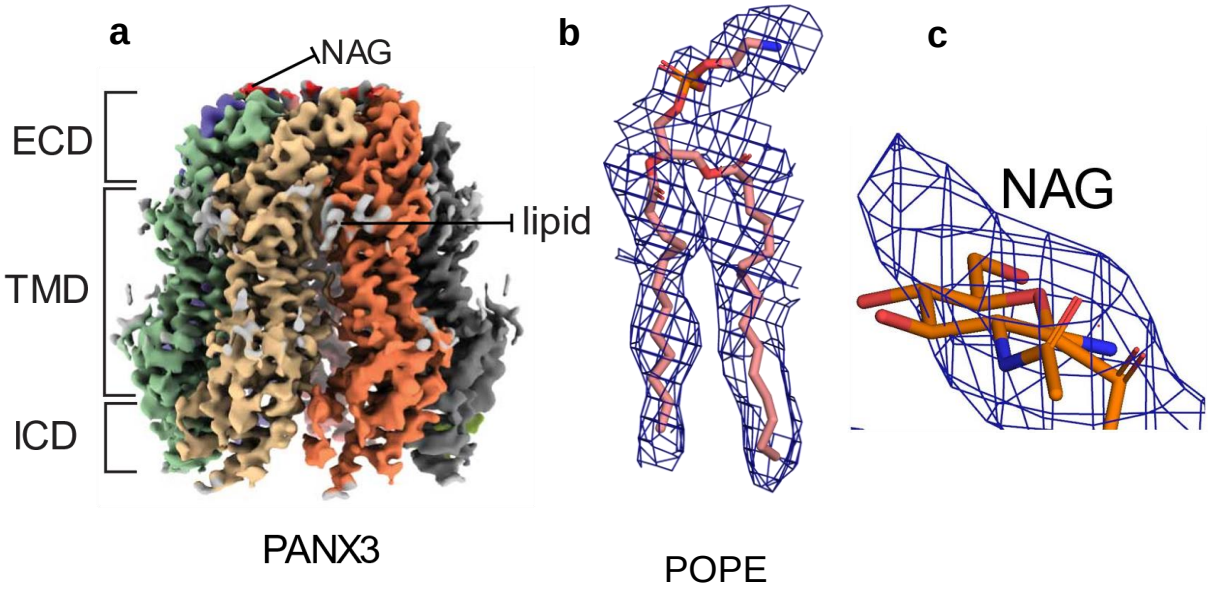

Fig. 5.8: The Cryo-EM map for PANX3 (monomers colored individually) viewed parallel to the membrane plane, the position of lipid-like densities modeled as POPE and glycosylation at N71 is modeled as NAG in PANX3, shown by gray and red, respectively. **a)** 3D

reconstruction for PANX3 at 3.9 Å resolution **b)** The lipid-like density observed in PANX3 was fitted with POPE **c)** Density for NAG at N71, contoured at a σ level of 7.5.

Lipids were present in the gap between the protomers, which we have modeled as POPE (Fig. 5.8b). We also observed the density at the putative glycosylation site, which we modeled as NAG (Fig. 5.8c). The PANX3 channel is 8 Å wider than the PANX1 at the cytosolic face but has a similar transmembrane height as PANX1 (Fig. 5.9a-b). The topology of PANX3 protomers is similar to $PANX1_{WT}$, with differences in the TM1 and C-terminus.

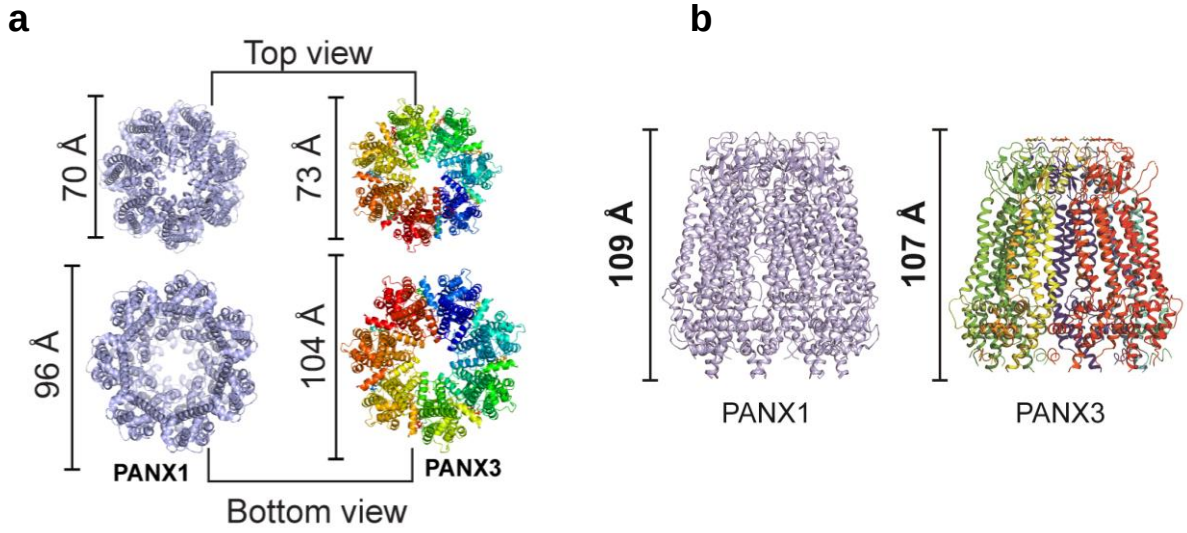

Fig. 5.9: a) The structure of $PANX1_{WT}$ and PANX3; top and bottom view exhibiting differences in the width in PANX channels. **b)** The side view of PANX structures.

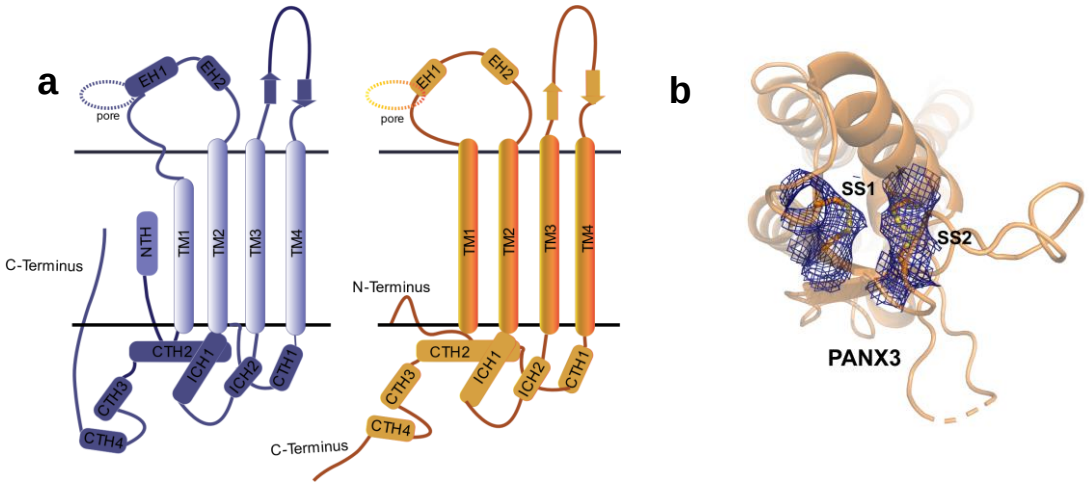

Fig. 5.10: a) PANX1(blue) and PANX3(orange) topology **b)** Two disulfide bonds(SS) in PANX3 stabilize the extracellular loops. Density for two disulfide bonds (SS1, SS2), contoured at a σ level of 7.0.

The topology comprises four transmembrane helices and two extracellular loops. Two disulfide bonds stabilize the extracellular loops, C66-C261(SS1) and C84-C242(SS2), that form between extracellular loop 1(EL1) and extracellular loop 2 (EL2) (Fig. 5.10a-b). The superposition of two protomers (PANX1-PANX3) results in a root mean square deviation (rmsd) of 3.2 Å for the 302 Cα atoms (Fig. 5.11b).

A significant alteration of surface charge was observed in PANX3 compared to $PANX1_{WT}$ near the surface lining the aqueous channel vestibule (Fig. 5.11a). Although $PANX1_{WT}$ has a positive charge at this position, PANX3 possesses a negatively charged environment which could influence the different roles of PANX1 and 3 isoforms.

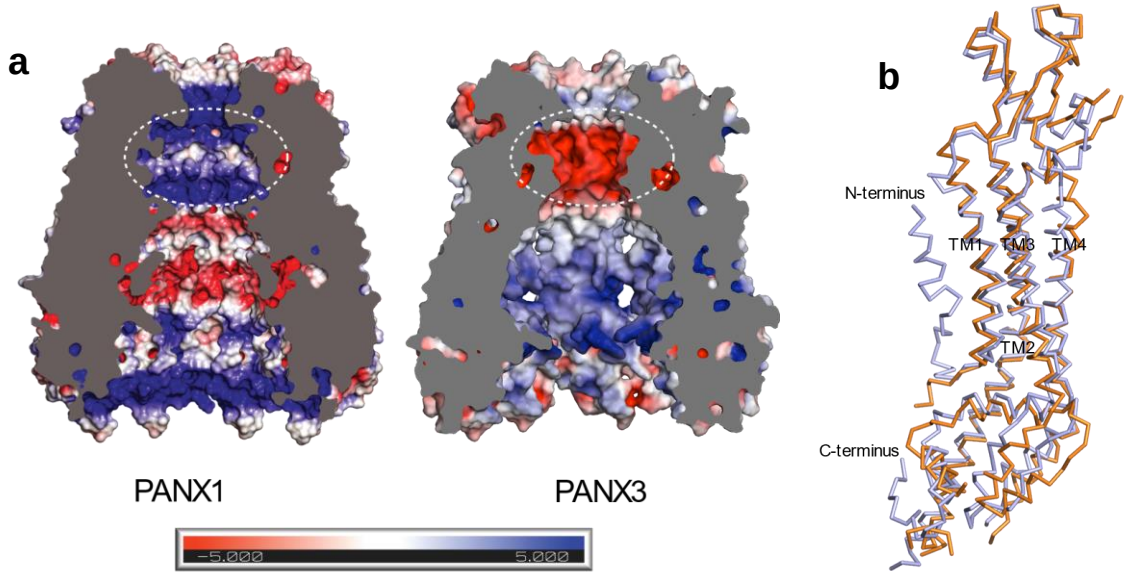

Fig. 5.11: a) Sagittal section of surface electrostatics of PANX1 and PANX3 colored according to potential from -5(red) to +5(blue) ($kBTec^{-1}$) viewed parallel to the membrane plane. b) The superposition of PANX1 and 3 protomer results in a Cα rmsd of 3.2 Å for the 302 atoms aligned.

In PANX1, N-terminus plays a role in maintaining the rigidity of the transmembrane domain[17]. However, we did not observe density for residues 1-24 (N-terminus) in PANX3, making it unfeasible to speculate the role of the N-terminus in PANX3.

Comparing the AlphaFold2 model of PANX3 with the experimental model in this study indicates that the N-terminus faces the cytosol. It constricts the channel from the cytoplasmic side, unlike $PANX1_{WT}$, where the N-terminus lines the pore towards the extracellular gate (Fig. 5.12).

We also could not model the last twenty residues (373-392) in C-terminus due to the lack of density in that region. Interestingly, density for C-terminus has not been observed in the PANX1 structures published so far. Moreover, C-terminus in PANX3 is comparatively shorter than PANX1 and might not serve as a plug to block access to the channel. Unlike PANX1, PANX3 also lacks a caspase cleavage site in the C-terminus, suggesting that PANX3 may have different mechanisms for channel opening.

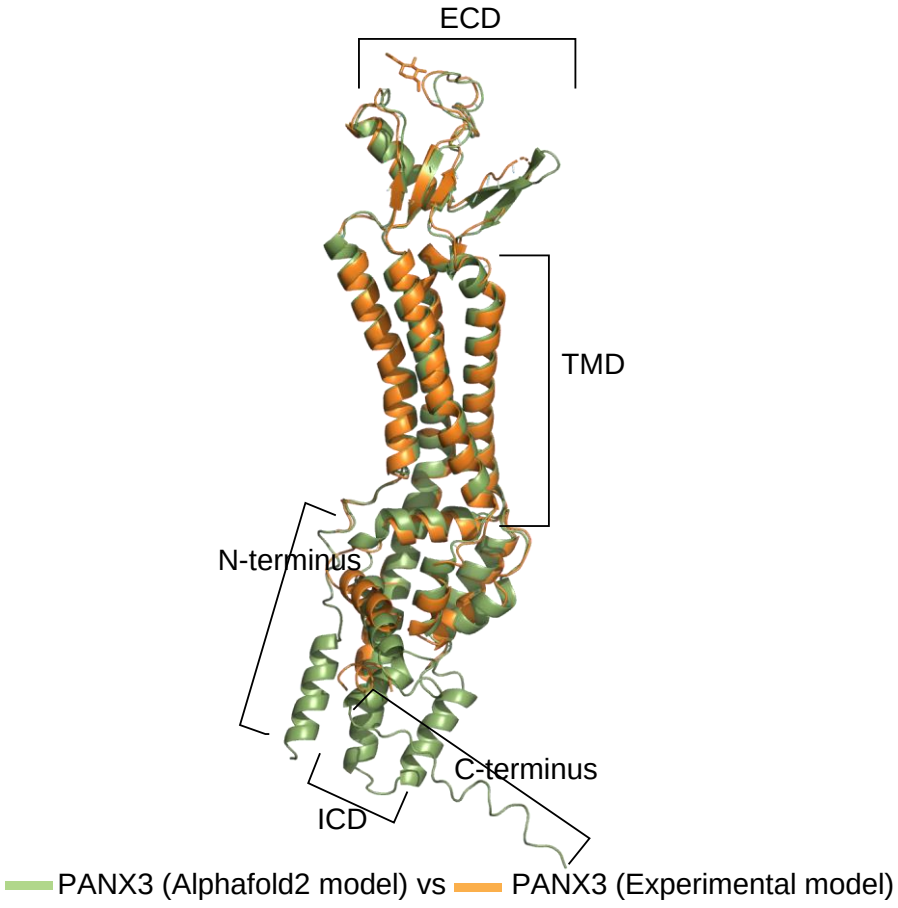

Fig. 5.12: The superposition of the PANX3 Alphafold2 model with the PANX3 experimental model results in a Cα rmsd of 1.1 Å for 266 atoms aligned. The N-terminus in the Alphafold2 model lies towards the cytoplasmic side.

5.4.1 Glycosylation in PANX3

N-linked glycosylation at the N255 position in the extracellular loop two (EL2) of PANX1 was implicated in preventing the formation of gap junctions (Fig. 5.13a). A

study by Ruan *et al*. observed that the substitution at this site (N255A) led to the formation of a mixture of gap junctions and hemichannels which aligns with the earlier hypothesis where different groups suggested that N-glycosylation at the extracellular loop in PANX1 makes them incompatible with forming gap junctions.

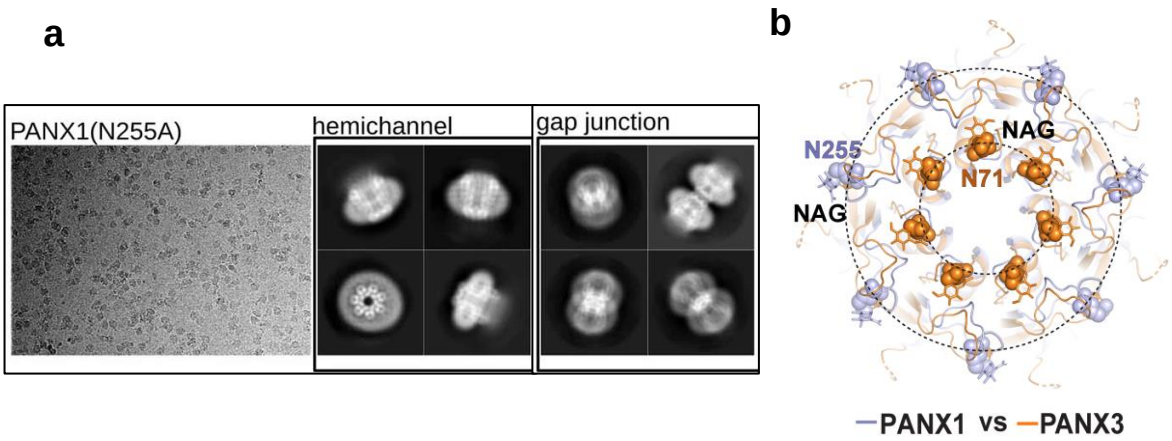

Fig. 5.13: a) PANX1(N255A) mutant exhibits hemichannel and gap junction populations[17], **b)** Position of N-glycosylation in PANX1 at N255 and N71 in PANX3.

In the PANX3 structure, we observed density for N-acetylglucosamine (NAG) at the predicted glycosylation site (N71) in the first extracellular loop (EL1) much closer to the pore gate compared to PANX1 (Fig. 5.13b). We mutated the asparagine 71 to alanine and purified the protein. The purified protein eluted at a higher volume than the expected elution volume for PANX3 hemichannels (Fig. 5.14).

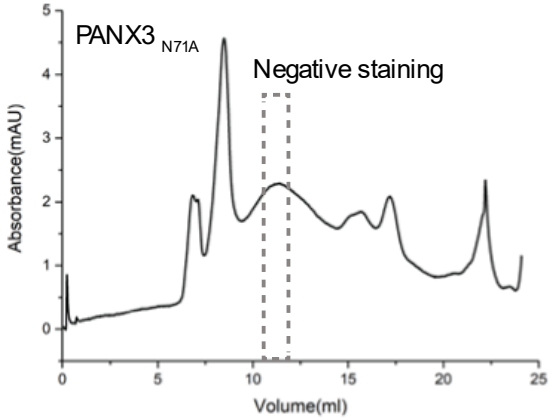

Fig. 5.14: SEC profile for $PANX3_{N71A}$ mutant solubilized and purified in GDN detergent. The elution volume was higher (~11 ml) than the $PANX3_{WT}$ (14 ml). The dashed line represents the fraction used for negative staining.

We used the protein for negative staining electron microscopy to rapidly screen the PANX3 for gap junction formation. PANX3 at a 0.01 mg/ml concentration was used for the negative staining.

Briefly, 3.5 µl of the sample was applied to glow discharged carbon-coated copper grid for 30 seconds, followed by blotting out excess buffer and sample. Negative staining was performed using 2% uranyl acetate for 25 seconds. The negative stained sample was visualized and imaged at room temperature using a Talos L120C electron microscope operated at 120 kV.

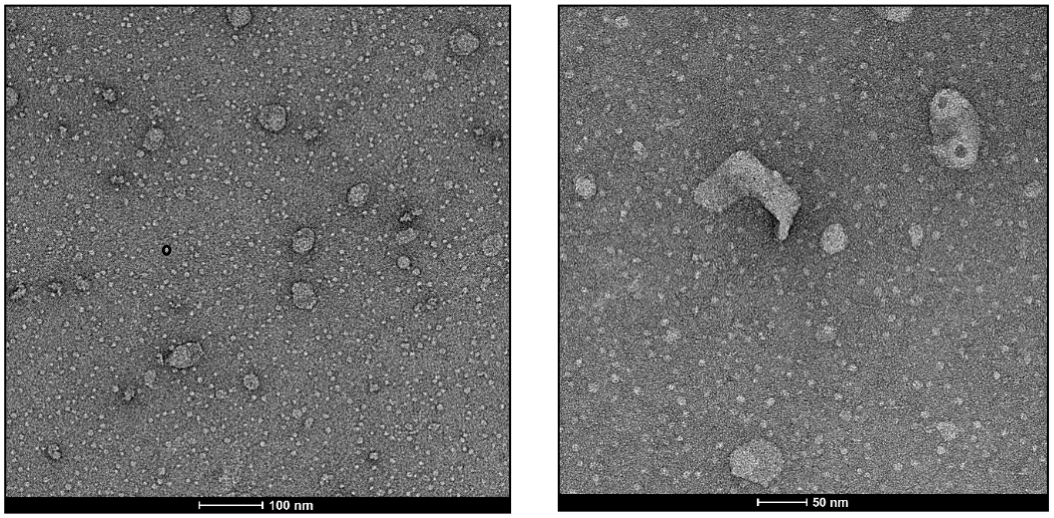

Fig. 5.15: Negative staining images for PANX3 mutant, $PANX3_{N71A}$, scale bar 100 nm (left), 50 nm (right). The micrographs do not show the presence of gap junctions.

However, we could not observe any gap junction population on the micrographs either because of the acidic nature of the stain or because of the incompatibility of PANX3 channels to form gap junctions even after mutating the glycosylation site from the extracellular loop (Fig. 5.15). Nonetheless, as we could not see any gap junction population in the micrographs, we did not perform Cryo-EM analysis as the mutant does not neɑessarily represent the physiological form of PANX3.

5.5 PANX3 displays double sieve organization

The residues W74 and R75 lines the first constriction point in PANX1. The W74 residue creates the smallest constriction in $PANX1_{WT}$, resulting in a pore diameter of 12 Å (Fig. 5.20-a). The tryptophan in PANX1 is replaced by isoleucine or valine in

different orthologues of PANX3 (Fig. 5.16). The human PANX3's pore is lined by two residues, I74 and R75, with a width of 13.2 Å at the narrowest point formed by I74 (Fig. 5.20-b)

```
                                        74
sp|P60570|PANX1_RAT     FSPSSFSWRQA 77
sp|Q9JIP4|PANX1_MOUSE   FSPSSFSWRQA 77
sp|Q96RD7|PANX1_HUMAN   FSPSSFSWRQA 77
sp|Q96QZ0|PANX3_HUMAN   FSPSNFSIRQA 77
sp|P60572|PANX3_RAT     FSPSNFSVRQA 77
sp|Q8CEG0|PANX3_MOUSE   FSPSNFSVRQA 77
```

Fig. 5.16: The pore-lining residue W74 is not conserved in PANX1 and 3 isoforms. For clarity, only a few species have been shown.

The cation-π interaction between W74 and R75 in PANX1$_{WT}$ is eliminated in PANX3 due to the replacement of W74 with I74. However, the interaction between R75 of one protomer and D81 of the other protomer via a salt bridge is consistent with PANX1$_{WT}$ (Fig. 5.17-a).

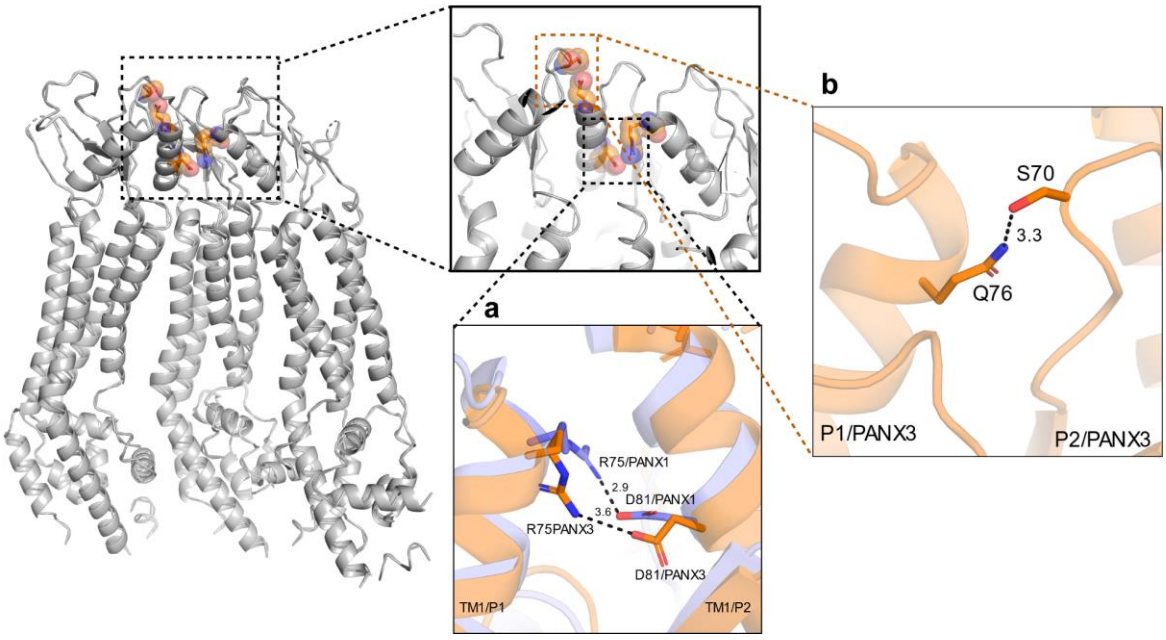

Fig. 5.17: Interactions between residues P1 (protomer1) and P2 (protomer) to form a stable heptamer. For clarity, three protomers are shown **a)** between R75 and D81, **b)** between S70 and Q76.

Similarly, S70 and Q76 between two protomers form a hydrogen bond resulting in interprotomeric interactions and a stable heptamer (Fig.5.17-b).

Apart from these interactions, there seem to be minimal intersubunit interactions across the transmembrane region between the protomers. The gap between the protomers is filled with lipids which we have modeled as POPE. However, we do not have experimental evidence for the presence of POPE, and it is fitted based on the density.

The residues at the end of TM1, 58-60 comprising residues F58, S59, and S60 form a prominent second constriction at the neck region in PANX3 compared to $PANX1_{WT}$. For clarity, only F58 is shown in both PANX1 and 3 (Fig. 5.18).

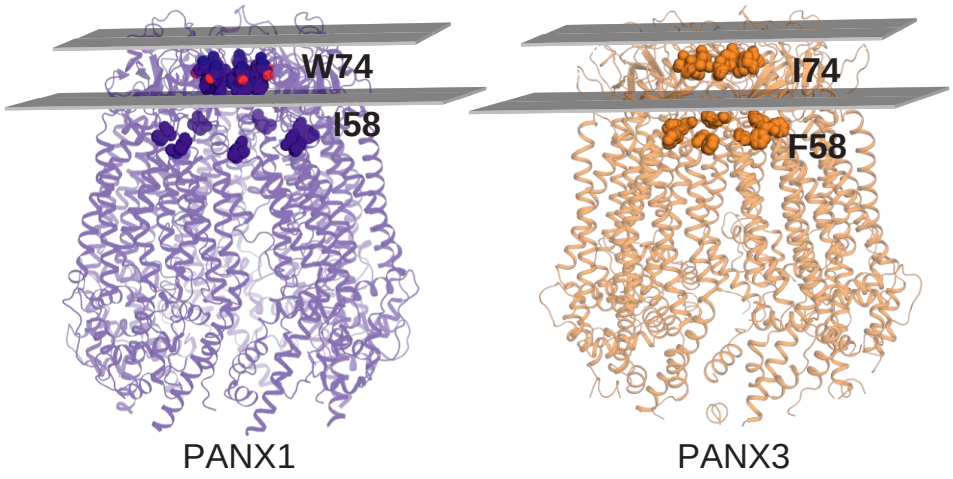

Fig. 5.18: F58 in PANX3 forms a proper second constriction compared to I58 in PANX1. The second constriction in PANX3 forms a ring and demarcates the PANX3 into two distinct compartments.

The residues F58-S59-S60 line the second constriction point facing the pore in PANX3, and these three-residue sequences are highly variable between PANX1, 2, and 3 (Fig. 5.19).

```
sp|Q96RD7|PANX1_HUMAN    LAFAQEISIGTQ 65
sp|Q96RD6|PANX2_HUMAN    LVFTKNFA-EEP 81
sp|Q96QZ0|PANX3_HUMAN    LAFAQEFSSGSP 65
```

Fig. 5.19: F58-F60 stretch of residues are highly variable in PANX isoforms, implicating isoform-specific roles of these residues.

The shortest diameter in PANX3, between the two diagonal F58, is 21 Å (Fig. 5.20-c) compared to 35 Å in PANX1WT formed by I58 (Fig.5.20-d). F58 in PANX3 separates the anionic surface of the upper compartment from the amphiphilic surface of the lower compartment. In contrast, I58 residue in $PANX1_{WT}$ engages in hydrophobic interactions between TMs 1 and 2.

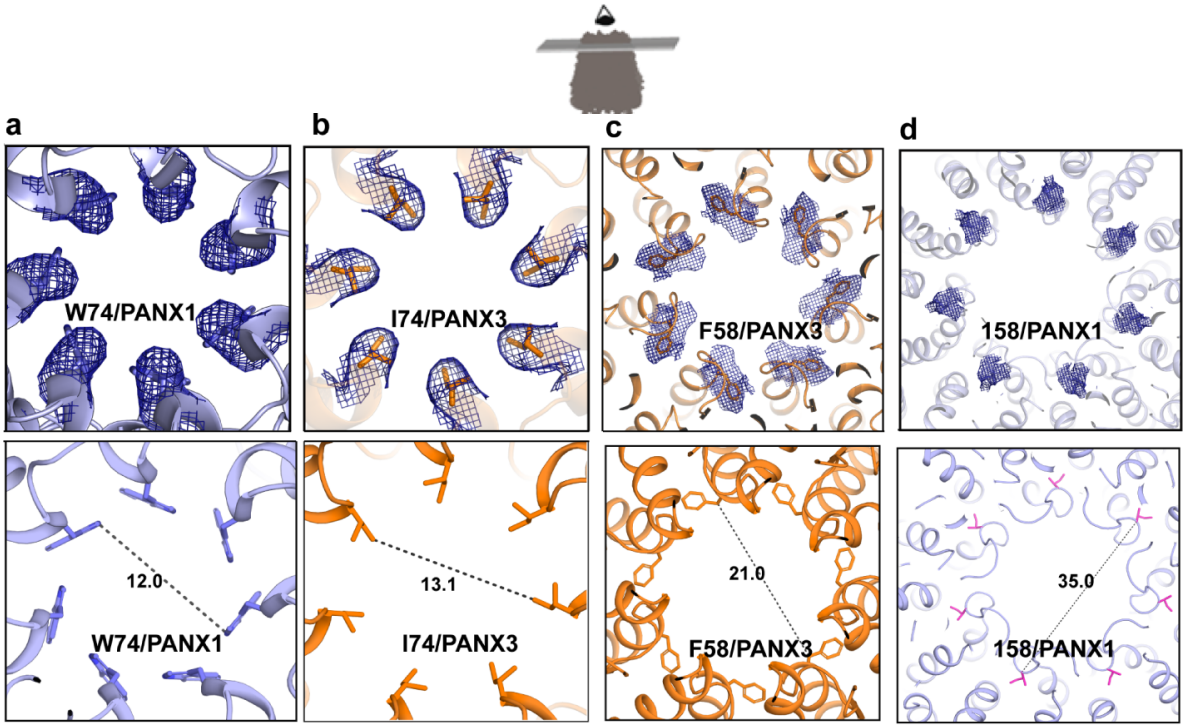

Fig. 5.20: PANX1(blue) and PANX3(orange) displaying the positions of the two constrictions, first constriction is formed by **a)** W74 in PANX1 and **b)** I74 in PANX3, **c)** F58 forms the second constriction in PANX3, **d)** the second constriction formed by 158 in PANX3. Density contoured at 7.5 and 6.0 σ for the residues involved in forming the two constrictions in PANX1 and 3, respectively.

Within the upper portion of the transmembrane domain, the lipid density bridges the space between the two protomers. In contrast, no lipid density was present in the lower portion of the transmembrane domain. A study by Ruan *et al.* suggested the presence

of a side tunnel at this position in PANX1 which can allow the passage of ions even when the C-terminus blocks the channel pore (Fig. 5.21)

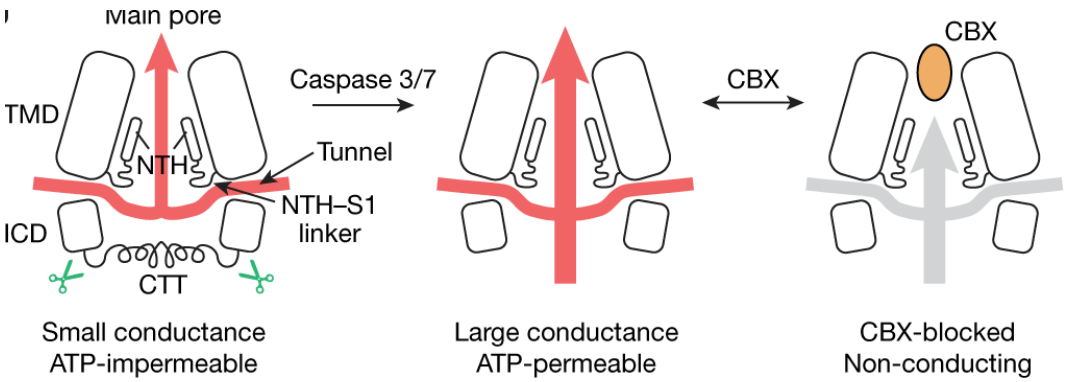

.

Fig. 5.21: The presence of a side tunnel in PANX1[17]. The side tunnel can act as a conduit for the passage of small ions when C-terminus blocks the PANX1 channel.

We could also observe a gap between subunits in PANX3 that is large enough to facilitate the passage of ions. The distance between TM2 and CTH1 is 6.9 Å in PANX3 as opposed to 6.3 Å in $PANX1_{WT}$, indicating that the lateral portal hypothesis may also hold true for PANX3. (Fig. 5.22).

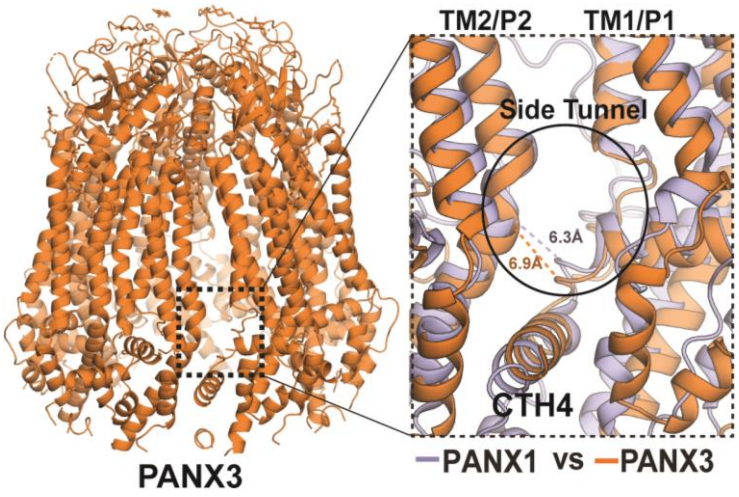

Fig. 5.22: PANX3 displaying a gap between the protomers; the gap is large enough to accommodate ions and can act as a side tunnel; Inset shows the superposition of PANX1 and PANX3 displaying the position of the side tunnel.

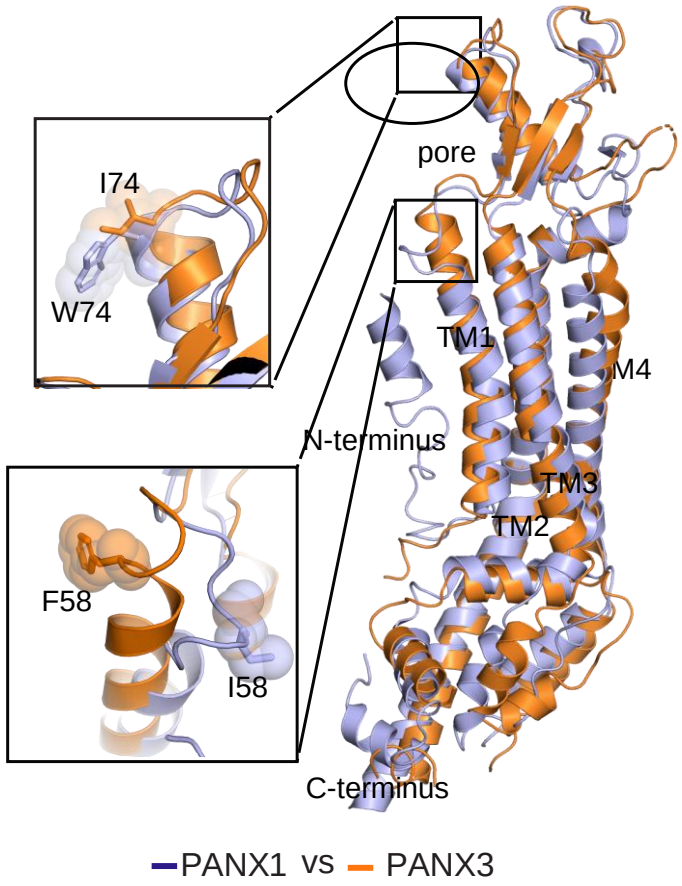

Fig. 5.23: Superposition of PANX1 and PANX3 displaying the position of residue 58 and 74. The superposition of PANX1 and 3 results in Cα rmsd of 1.1 Å for 302 atoms aligned. The pore-gating residues are W74 and I74 in PANX1 and 3, respectively.

The linker between TM1 and TM2 adopts a clear α-helical conformation in PANX3 instead of a loop observed in $PANX1_{WT}$, constricting the vestibule in the region, thus allowing PANX3 to have an additional vestibule beneath the primary constriction (Fig.5.23). In PANX3, the F58 is oriented in the direction of the pore, whereas the I58 in PANX1 is located between TM1 and 2.

5.6 PANX3 elicits current at positive voltages

PANX3 is believed to form gap junctions in a cell-specific manner[13,115]. However, we did not observe any gap junction formation during the purification and structure determination of PANX3. Electrophysiology studies by Sahu *et al*. revealed the formation of PANX3 gap junctions in Hela cells but not in N2A or PC-12 cells[13]. They observed that PANX3 hemichannels in N2A or PC-12 cells do not activate in the

presence of positive voltages. Bruzzone *et al*. also failed to observe any current in PANX3 transfected cells at positive voltages in N2A cells[22]. Moreover, a study by Michalski *et al*. shows that PANX3 does not open in response to positive voltages when expressed in HEK293 cells[99]. Similar contradictions have been observed in earlier studies in PANX1, where Ma *et al*. and Chiu *et al.* observed different voltage responses of PANX1 in HEK293 cells[52,58].

In contradiction to earlier studies, we observed similar current signatures in both PANX1 and PANX3 in HEK293 cells (Fig.5.24). The PANX3 transfected cells generated currents in response to positive voltages and exhibited carbenoxolone sensitivity (Fig.5.24-a). However, carbenoxolone sensitivity was lower in PANX3 than in $PANX1_{WT}$, possibly due to the substitution of W74 with I74 at the suggested main binding site (W74 in PANX1) (Fig.5.25-b).

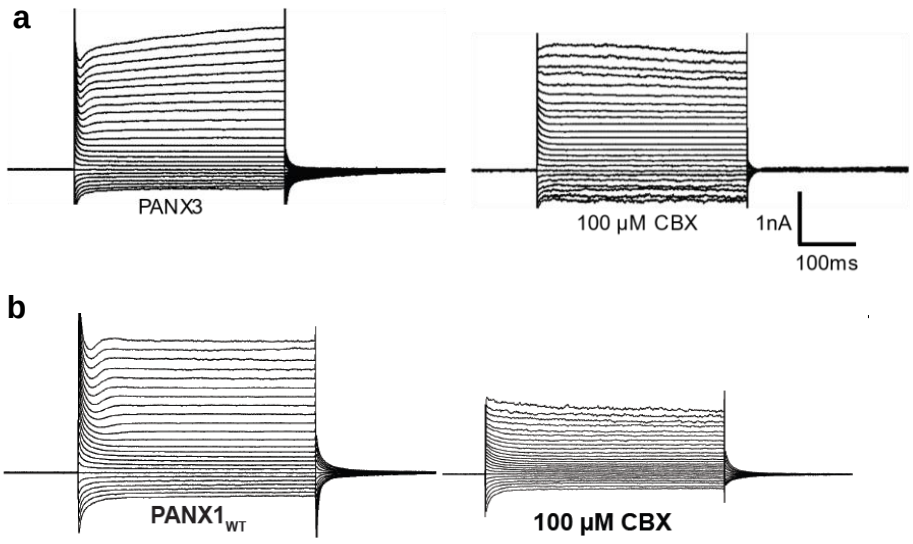

Fig. 5.24: Representative raw trace for patch-clamped PANX1 and PANX3 transfected HEK293 cells with and without the application of CBX. The PANX1 and 3 isoforms show similar current signatures when expressed in HEK293 cells.

Further electrophysiological investigations of PANX3 in HEK293 cells might aid the PANX field in resolving this discrepancy in PANX3 voltage dependence among cell lines.

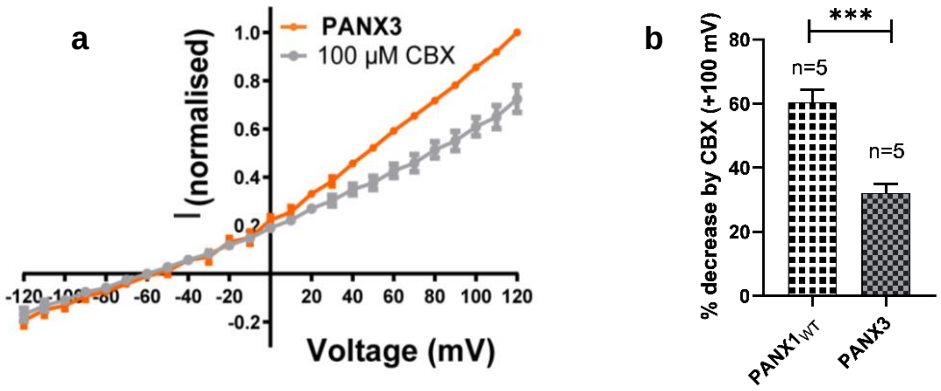

Fig. 5.25: a) Current-Voltage curve for PANX3 without CBX (orange) and with CBX (gray). **b)** Percentage inhibition by a PANX inhibitor, CBX plotted at +100mV for wild-type PANX1, 3. The number of recordings is mentioned in the parenthesis, error bar represents SEM. A two-tailed unpaired t-test is used for calculating the significance, ***p < 0.001; n.s., not significant.

5.7 PANX3 binding with ATP-γS

PANX1 and 3 isoforms have been observed to release ATP from the cells. We used MST to measure the binding affinity of PANX3 to ATP-γS (Fig.5.26). The binding affinity of PANX3 (75 µM) was lower than $PANX1_{WT}$ (13 µM). However, it is difficult to comment on the observed differences in the binding affinity between PANX1 and 3 due to the lack of information regarding the ATP binding pocket in PANX3.

Nevertheless, we have observed a decrease in ATP-γS binding affinity in $PANX1_{R217H}$ due to the alteration of the surface charge in the permeation pathway. Since the surface charge in PANX1 and 3 isoforms differ, the reduced ATP-γS binding affinity could result from the altered charge in PANX3.

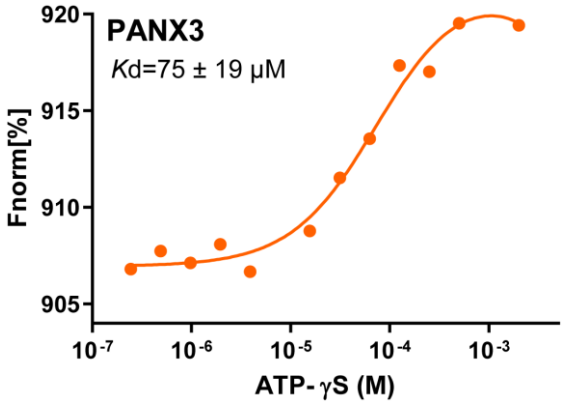

Fig. 5.26: Binding affinity with ATP-γS for PANX3 was determined as 75±19 µM. The binding affinity of PANX3 with ATP--γS is lower than $PANX1_{WT}$ (13 µM).

5.8 Summary

In this chapter, we have outlined PANX3's structural arrangement and made a comparison to $PANX1_{WT}$. PANX3 has a similar overall fold to PANX1 but with a few distinctive differences. PANX3 has distinct electrostatic potentials within the pore and a significant lateral tunnel that could function as a conduit for small ions to pass through. PANX3 has a wider pore than PANX1 and uses isoleucine as the gating residue instead of tryptophan. The vestibule is divided into two separate chambers with distinct surface charges.

In addition, we investigated how PANX3 binds to ATP-γS to understand the functional differences amongst PANX isoforms better. PANX3 has a reduced propensity to interact with ATP-γS than $PANX1_{WT}$, shown by PANX3's lesser binding to ATP-γS, which can result from the altered charge in the permeation pathway of PANX3.

We also looked into PANX3's sensitivity to voltage in HEK293 cells. In contrast to past studies conducted on N2A, HEK293 cells, we detected a voltage dependence of PANX3 at higher voltages similar to the $PANX1_{WT}$, indicating a similarity in channel activity among PANX1 and 3 isoforms concerning their ATP release and electrical properties.

In summary, this chapter highlights the structural and functional differences between the PANX1 and 3 isoforms.

CHAPTER 6

Discussion

In this study, we report the previously unknown structure of PANX3, a PANX1 isoform. PANX3 shows a heptamer oligomeric assembly similar to PANX1 with differences in TM1 and C-terminus. In contradiction with existing literature, our study reveals that PANX3 has a weak voltage dependency similar to PANX1 and responds to positive voltages. Although our data lack experimental evidence to support the closure of the pore by lipids, we observed lipid-like densities between the transmembrane domain in PANX3, similar to those observed in CALHM channels[103]. Interestingly, neither wild-type nor mutant PANX1 structures contain this type of density. More recently, the role of lipids in closing the channel has been proposed in LRRC8 channels[109,109,176]. As more and more studies on large pore channels become available, a plausible mechanism for channel blockage by lipids can be proposed. Currently, it can be summarized as an intriguing observation.

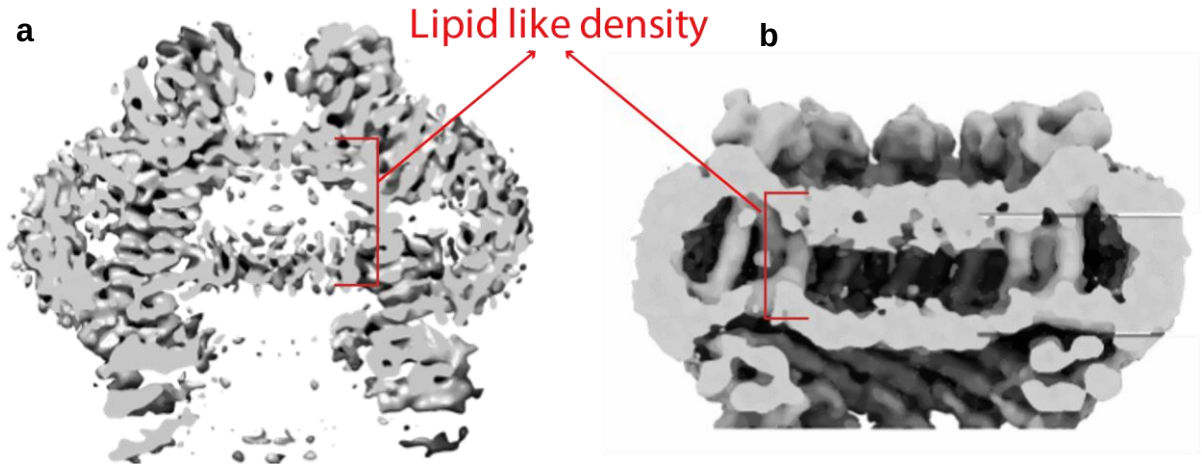

Fig. 6.1: Lipids are speculated to act as a pore gate in large pore channels. Lipid-like density present in a) PANX3, b) CALHM[103]

A distinctive feature of PANX3 is the presence of F58 in the neck region towards the pore, which creates a boundary in the PANX3 permeation pathway, dividing it into two vestibules. Moreover, phenylalanine residue at the neck has been observed to act as a determinant of ion flux through channels like Bestrophin. Also, a mutant of a similar size, such as isoleucine, is observed to diminish the influx of ions[177]. Since a similar mutation is observed in PANX1, where F58 in PANX3 is replaced by I58 in PANX1, it would be interesting to explore the role of F/I 58 in ion flux in PANX isoforms. The comparison of ATP-γS binding affinities between PANX1 and 3 reveals that PANX3

has lower ATP-γS binding affinity compared to PANX1. Although we could grasp the function of positively charged residues in ATP binding, we could not identify clear ATP-binding pocket in PANX isoforms. Consequently, it is challenging to collect experimental evidence for the decreased ATP binding in PANX3.

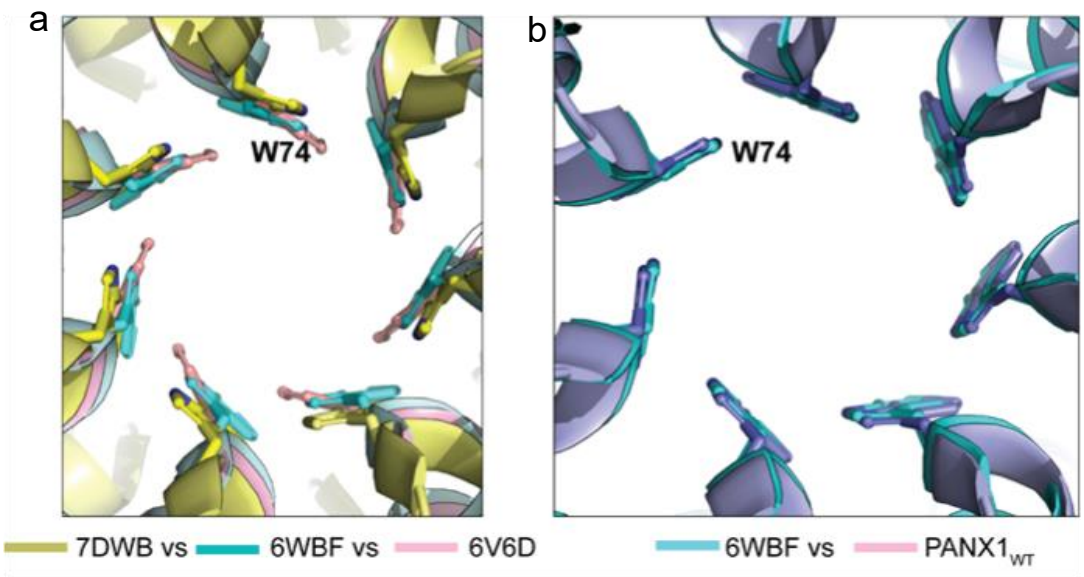

Fig. 6.2: a) Superposition of $PANX1_{WT}$ (Cα rmsd =0.3-0.5 Å for 324 atoms aligned) determined by three individual groups[17,57,178], **b)** Superposition of $PANX1_{WT}$ determined by our group and Ruan *et al*.

However, there is a major charge alteration in the permeation pathway between the isoforms, suggesting that the charge alteration could play a role in the reduced ATP-γS binding. Previous structures of $PANX1_{WT}$ were determined by multiple groups in different buffer conditions reported to retain the channel in different states; for example, high K^+ is the most commonly used stimulus to open the channel[13,53,174], and C-terminus cleavage was shown to have increased current density in whole-cell recordings[17]. However, all the previously determined structures have similar pore diameters, as shown in Fig. For clarity, only 3 structures are shown[17,57,178].

A comparison of the $PANX1_{WT}$ structure determined in this study and Ruan *et al*. reveals that both the $PANX1_{WT}$ structures have similar pore diameters. Also, both structures were determined in similar buffer conditions[17].

As there is no structure of PANX1 in the current scientific literature that displays a different conformation, the mechanism of channel opening and closing remains unknown. Thus, we tried to reveal the mechanism of closure of the pore by a congenital mutation ($PANX1_{R217H}$) and a double mutant ($PANX1_{DM}$) which could give us an insight into the mechanism of channel closing.

The Cryo-EM structure of congenital mutant R217H reveals a smaller pore than $PANX1_{WT}$. The structural comparison with $PANX1_{WT}$ reveals an outward movement of the extracellular domain and an inward movement of the intracellular domain. We also observed the disruption of the local network in $PANX1_{R217H,}$ which translates to the movement of TM1 and, subsequently, rotation of the W74 by its χ torsion angle by ~87° and partially closing the pore. Like the R217H mutant, the PANX2 pore mimic, double mutant, also exhibits a narrower pore than $PANX1_{WT}$.

The PANX2 mimic resembles LRRC8A at the primary constriction, where the constriction is lined by a ring of positively charged arginine residue and plays an essential role in ion permeability[108]. In other isoforms of LRRC8, the arginine is replaced by leucine and phenylalanine; a similar substitution can also be seen in pannexin isoforms.

The analysis of the pore profiles generated by the Hole V2.0 program reveals a major difference in the primary constriction[179]. The primary characteristic that differentiates $PANX1_{WT}$ from pore mutants is the smaller size of the primary constriction in both the mutants (Fig.6.3). The smallest Vander Waal radii were measured to be 2.3 Å for $PANX1_{DM}$, 2.4 Å for $PANX1_{R217H}$, 4.0 Å for PANX3, and 4.2 Å for $PANX1_{WT}$ at the entrance of the pore. However, PANX3 has a slightly bigger pore than the $PANX1_{WT}$.

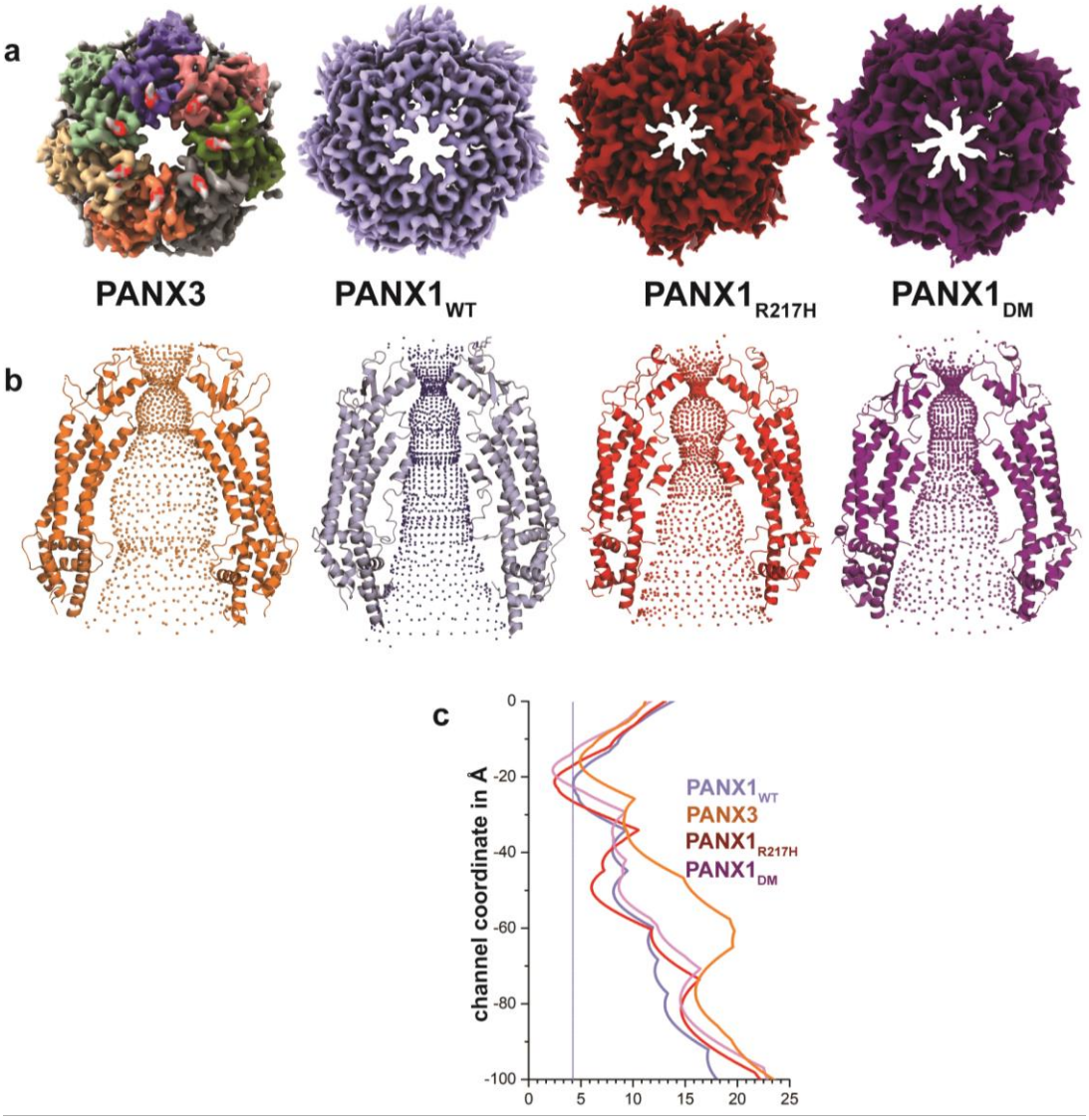

Fig. 6.3: a) Cryo-EM maps for PANX1, 3 and the mutants, **b)** Pore profiles generated by hole program. The minimum radius is observed at the first constriction in PANX isoforms, and **c)** 2D representation of the hole profile exhibiting differences in the constriction in PANXs. The dashed line represents the Van der Waal radius for $PANX1_{WT}$ (4.2 Å).

To understand the implications of the smaller pore in the mutants, we performed electrophysiology recording and plotted the current density vs. voltage graph. The smaller pore radius showed a decrease in the current density compared to the $PANX1_{WT}$.

Moreover, a comparison of ATP-γS binding affinities of the mutants with the $PANX1_{WT}$ suggests the role of the positive residues lining the pore in ATP binding. Moreover, mutating these residues lead to charge alteration and reduced ATP binding, as observed in $PANX1_{R217H}$.

We also studied the role of these residues in the voltage dependence of the channel and performed patch clamp electrophysiology recordings.

While the change in the geometry of pore residues is essential for partially closing the channel, our study suggests that the pore residues do not play a role in the voltage sensitivity of the channel. The conductance-voltage plot implies that voltage sensitivity is imparted to the PANX channel by the transmembrane region.

In conclusion, the study gives insight into the voltage sensitivity and provides a mechanism for the partial closure of the PANX1 channel. Also, this thesis suggests that PANX3 may have a unique mechanism for closing the pore, and further studies are required to understand the disparity between PANX isoforms.

Limitations

One limitation of this study is the low resolution of the PANX1 and PANX3 structures. Conclusions drawn from higher resolution structures are generally more reliable. However, due to limited microscope access and a small particle dataset, it was not feasible to obtain higher resolution structures for the proteins studied. In addition, the PANX3 and $PANX1_{DM}$ mutant proteins were not stable in multiple detergents, which resulted in only a subset of particles forming proper heptamers. While there is limited control over the stability of the proteins, increasing the signal-to-noise ratio by collecting more data could improve the resolution of the structures.

Another limitation is the inability to establish a proper ATP release experiment to correlate with ATP binding studies due to inconsistencies in the experiment. Despite testing different cell lines and conditions, the results were highly inconsistent and non-reproducible. A single-cell study, as done by Narahari *et al*. may be beneficial for observing ATP release in Pannexin channels.

Supplementary Figure

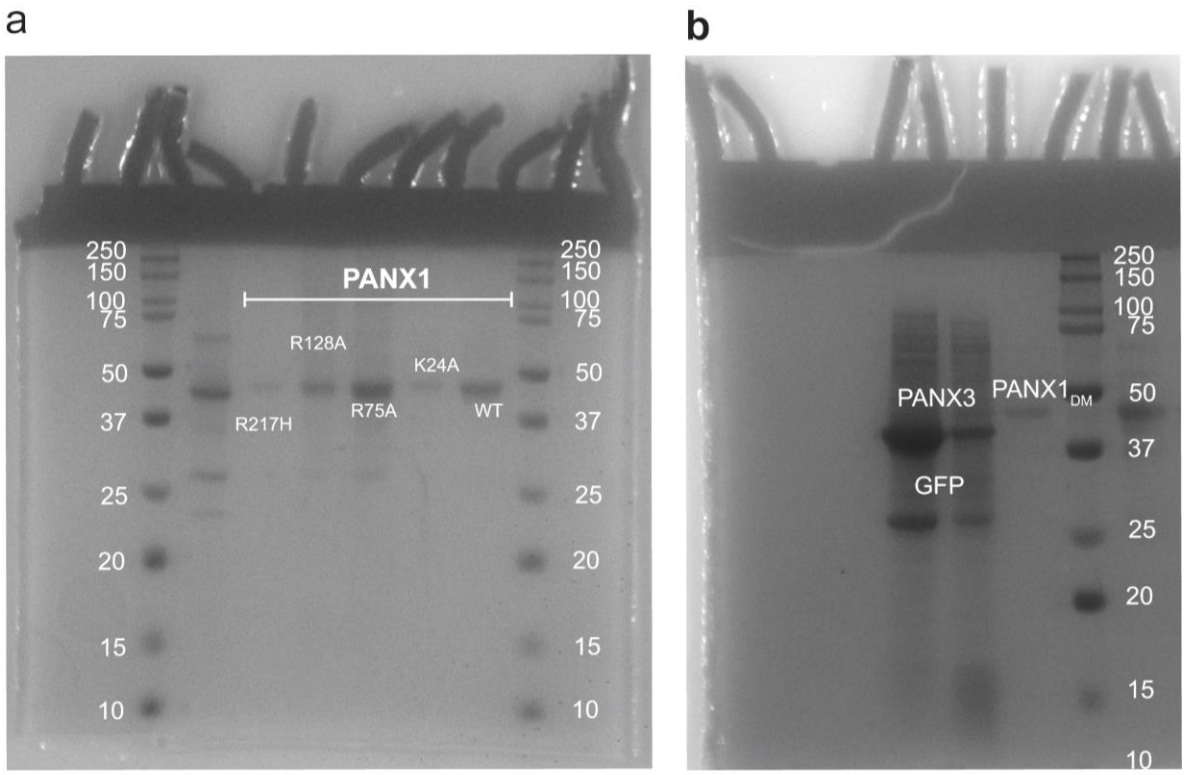

Fig. S1: a-b) SDS-PAGE profile for the $PANX1_{WT}$, PANX3 and the PANX1 mutants ($PANX1_{K24A}$, $PANX1_{DM}$, $PANX1_{R75A}$, $PANX1R_{128A}$) used in this study.

Appendix-A

ATP Release Assay:

In order to assess the activity of Pannexin channel in releasing ATP, we utilized high extracellular levels of potassium as a stimulus to trigger the opening of the channel. The phenomenon of Pannexin channels being activated by high potassium and subsequently releasing ATP has been extensively studied in the literature. When the Pannexin channels are stimulated by high levels of extracellular potassium, they release ATP which is then utilized in the conversion of D-luciferin to oxyluciferin.

We made use of the luciferase enzyme, which is dependent on ATP for the oxidation of D-luciferin to oxyluciferin. The formation of oxyluciferin is associated with the emission of light, and we utilized this light emission to measure the ATP release activity of the Pannexin channels. The schematics for the conversion of of luciferin to oxyluciferin is described below.

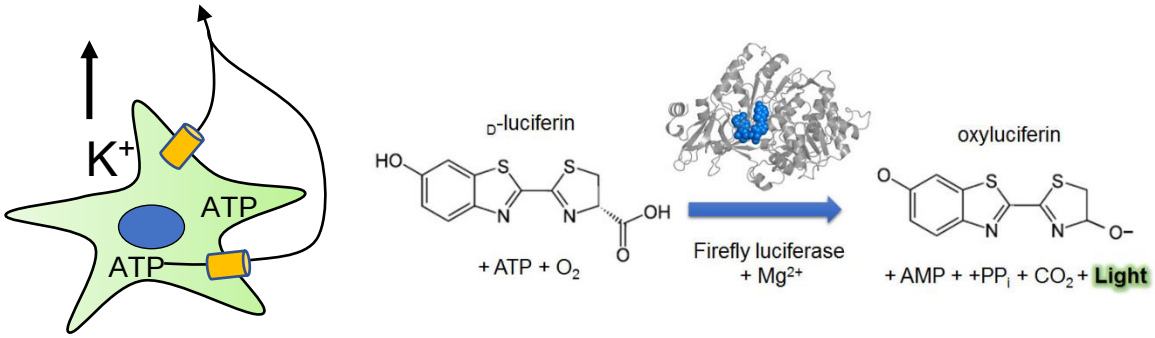

Protocol

* Throughout the protocol, it is imperative to minimize plate agitation to prevent mechanical stimulation of the cells, which can lead to the release of adenosine triphosphate (ATP) into the media.

Day 1

- Coat sterile culture dishes with 0.1% poly-L-lysine for 30 minutes in a sterile cell culture hood.
- Wash the coated plates with 1x phosphate-buffered saline (PBS) three times and expose them to ultraviolet (UV) light for 10 minutes.

- Plate adherent cells at an appropriate seeding density to achieve confluency by the end of the transfection protocol.

Day 2

- Wash cells three times with sterile 1x PBS using a P-1000 pipette to slowly change solutions.
- Replace fetal bovine serum (FBS) with 1% bovine serum albumin (BSA) in basal culture media (DMEM), keeping the final volume to 150 µl for a 24-well dish.
- Incubate cells at 37°C in a humidified cell culture incubator for 30 minutes to allow degradation of any ATP that may have been released into the media during the wash steps.
- Inhibit ectonucleotides activity from your cells by adding 50 µM ARL 67156 to each well of your plate. Extracellular ATP can be rapidly degraded by these enzymes depending on their expression in your cell type.
- Incubate cells at 37°C in a humidified cell culture incubator for 30 minutes.
- Treat your cells with carbenoxolone (100 µM) for 10 minutes at 37°C.
- Stimulate ATP release from your cells by adding 100 mM potassium chloride and 140 mM potassium gluconate, and incubate for 15 minutes at 37°C.
- Collect a sample from each well by removing the extracellular media with a pipette using ice-cold tips and transfer to sterile microfuge tubes on ice. For experiments using 24-well plates, collect 10 µl of media from each well.
- Prepare serial dilutions of ATP standard using the ATP standard supplied in the ATP bioluminescence assay kit.
- Prepare the luciferin: luciferase reagent supplied in the ATP bioluminescence assay kit (Thermofisher) following the manufacturer's instructions.
- Pipette 90 µl of luciferin-luciferase reagent and 10 µl of each sample into wells of an opaque 96-well plate.
- Read the luminescence for each sample.
- Create a standard curve to determine ATP concentrations in your samples using the luminescence values obtained for each of your ATP standards.

- Calculate the concentration of ATP in each of your samples using the standard curve created.

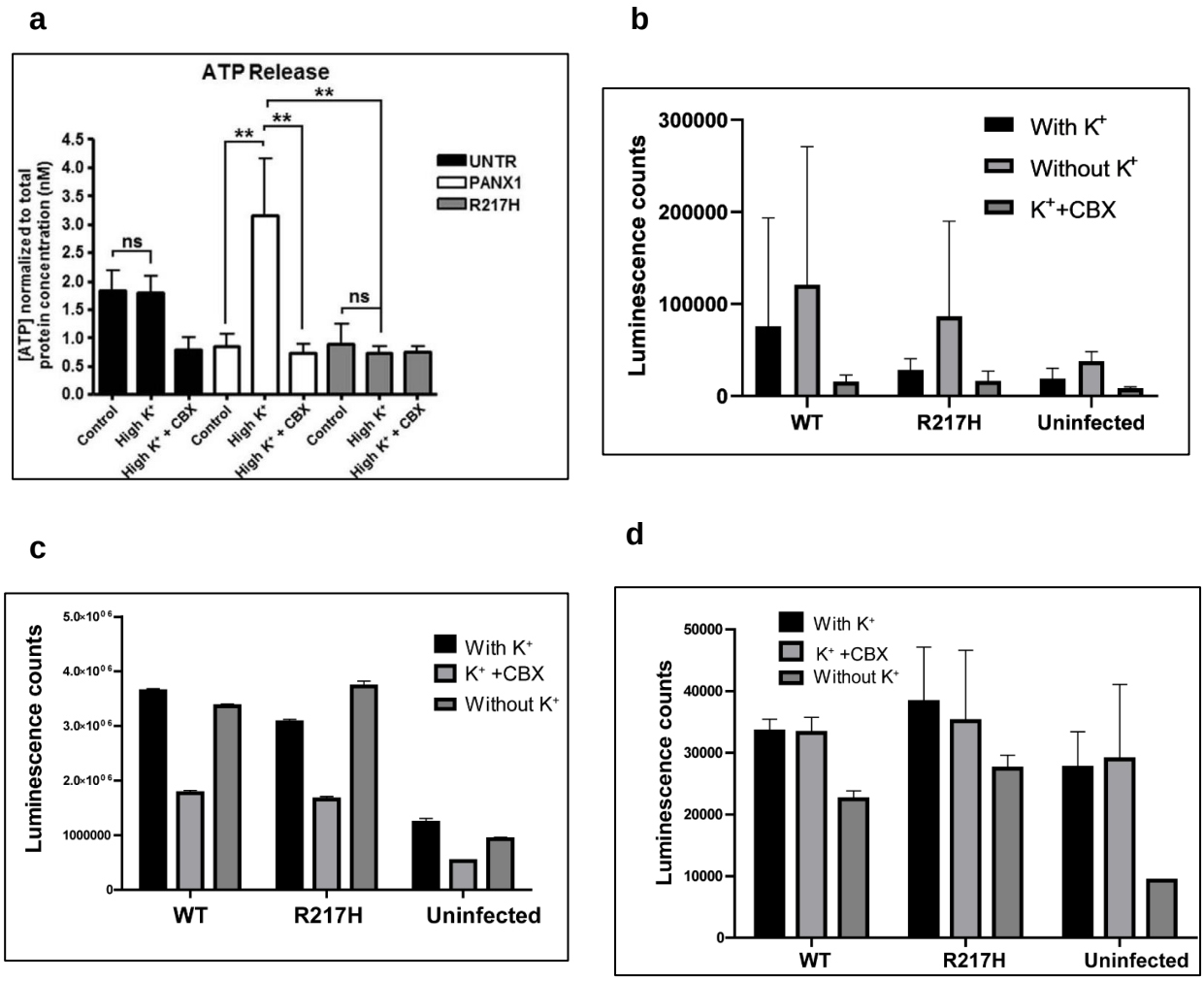

Fig. ATP release experiment in Pannexin channels using luciferase based detection of ATP in presence of Pannexin inhibitor, CBX (100µM) **a)** ATP release experiment performed by Shao *et al*. showing reduced ATP release in the mutant Pannexin1 channel. **b)** in MDCK cells (n=21) **c)** in HEK 293 cells (n=9) **d)** in SF9 cells (n=3).

Observations

We performed ATP release experiment to understand the ATP release property of Pannexin channels. However, the results were inconsistent across different cell lines (MDCK, HEK293, SF9). To avoid any potential bias, we did not include the ATP release data in our analysis.

Data Availability

The structures have been deposited with the accession numbers in PDB, 8GTR(PANX3), 8GTS($PANX1_{R217H}$), 8GTT($PANX1_{DM}$). The CryoEM density maps have been deposited in EMDB under accession numbers, EMD-34265(PANX3), EMD-34268($PANX1_{WT}$), EMD-34266($PANX1_{R217H}$), EMD-34267($PANX1_{DM}$).

References

1. Dale, H. H., Feldberg, W. & Vogt, M. Release of acetylcholine at voluntary motor nerve endings. *J. Physiol.* **86**, 353–380 (1936).

2. del Castillo, J. & Katz, B. Quantal components of the end-plate potential. *J. Physiol.* **124**, 560–573 (1954).

3. Furshpan, E. J. & Potter, D. D. Transmission at the giant motor synapses of the crayfish. *J. Physiol.* **145**, 289–325 (1959).

4. Bennett, M. V. L., Spray, D. C. & Harris, A. L. Gap junctions and development. *Trends Neurosci.* **4**, 159–163 (1981).

5. Pereda, A. E. Electrical synapses and their functional interactions with chemical synapses. *Nat. Rev. Neurosci.* **15**, 250–263 (2014).

6. Beyer, E. C. & Berthoud, V. M. Gap junction gene and protein families: Connexins, innexins, and pannexins. *Biochim. Biophys. Acta - Biomembr.* **1860**, 5–8 (2018).

7. Dev, G. A ubiquitous family of putative gap junction molecules Yuri Panchin *, Ilya Kelmanson *, Mikhail Usman † and Sergey. *Curr. Biol.* 473–474 (2000).

8. Penuela, S., Gehi, R. & Laird, D. W. The biochemistry and function of pannexin channels. *Biochim. Biophys. Acta - Biomembr.* **1828**, 15–22 (2013).

9. Bargiello, T. A. *et al.* Gating of Connexin Channels by transjunctional-voltage: Conformations and models of open and closed states. *Biochim. Biophys. Acta - Biomembr.* **1860**, 22–39 (2018).

10. Sosinsky, G. E. *et al.* Pannexin channels are not gap junction hemichannels. *Channels* **5**, 193–197 (2011).

11. Penuela, S. *et al.* Pannexin 1 and pannexin 3 are glycoproteins that exhibit many distinct characteristics from the connexin family of gap junction proteins. *J. Cell Sci.* **120**, 3772–3783 (2007).

12. Huang, Y., Grinspan, J. B., Abrams, C. K. & Scherer, S. S. Pannexin1 is

expressed by neurons and glia but does not form functional gap junctions. *Glia* **55**, 46–56 (2007).

13. Sahu, G., Sukumaran, S. & Bera, A. K. Pannexins form gap junctions with electrophysiological and pharmacological properties distinct from connexins. *Sci. Rep.* **4**, 1–9 (2014).

14. Bruzzone, R., Hormuzdi, S. G., Barbe, M. T., Herb, A. & Monyer, H. Pannexins, a family of gap junction proteins expressed in brain. *Proc. Natl. Acad. Sci. U. S. A.* **100**, 13644–13649 (2003).

15. Boassa, D. *et al.* Pannexin1 channels contain a glycosylation site that targets the hexamer to the plasma membrane. *J. Biol. Chem.* **282**, 31733–31743 (2007).

16. Penuela, S. *et al.* Diverse post-translational modifications of the pannexin family of channel-forming proteins. *Channels* **8**, 124–130 (2014).

17. Ruan, Z., Orozco, I. J., Du, J. & Lü, W. Structures of human pannexin 1 reveal ion pathways and mechanism of gating. *Nature* **584**, 646–651 (2020).

18. Boassa, D., Qiu, F., Dahl, G. & Sosinsky, G. Trafficking Dynamics of Glycosylated Pannexin1 Proteins. *Cell Commun. Adhes.* **15**, 119–132 (2008).

19. Penuela, S., Bhalla, R., Nag, K. & Laird, D. W. Glycosylation Regulates Pannexin Intermixing and Cellular Localization. *Mol. Biol. Cell* **20**, 4313–4323 (2009).

20. Baranova, A. *et al.* The mammalian pannexin family is homologous to the invertebrate innexin gap junction proteins. *Genomics* **83**, 706–716 (2004).

21. Dvoriantchikova, G., Ivanov, D., Panchin, Y. & Shestopalov, V. I. Expression of pannexin family of proteins in the retina. *FEBS Lett.* **580**, 2178–2182 (2006).

22. Bruzzone, R., Hormuzdi, S. G., Barbe, M. T., Herb, A. & Monyer, H. Pannexins, a family of gap junction proteins expressed in brain. *Proc. Natl. Acad. Sci.* **100**, 13644–13649 (2003).

23. Sanchez-Pupo, R. E. *et al.* Pannexin 2 is expressed in murine skin and promotes UVB-induced apoptosis of keratinocytes. *Mol. Biol. Cell* **33**, (2022).

24. Le Vasseur, M., Lelowski, J., Bechberger, J. F., Sin, W.-C. & Naus, C. C. Pannexin 2 protein expression is not restricted to the CNS. *Front. Cell. Neurosci.* **8**, (2014).

25. Fu, D. *et al.* Expression of Pannexin3 in human odontoblast-like cells and its hemichannel function in mediating ATP release. *Arch. Oral Biol.* **60**, 1510–1516 (2015).

26. Penuela, S., Celetti, S. J., Bhalla, R., Shao, Q. & Laird, D. W. Diverse Subcellular Distribution Profiles of Pannexin1 and Pannexin3. *Cell Commun. Adhes.* **15**, 133–142 (2008).

27. MacKinnon, R. Potassium channels. *FEBS Lett.* **555**, 62–65 (2003).

28. Michalski, K. *et al.* The Cryo-EM structure of a pannexin 1 reveals unique motifs for ion selection and inhibition. *Elife* **9**, 1–14 (2020).

29. Narahari, A. K. *et al.* Atp and large signaling metabolites flux through caspase-activated pannexin 1 channels. *Elife* **10**, 1–21 (2021).

30. Ma, W. *et al.* Pannexin 1 forms an anion-selective channel. *Pflugers Arch. Eur. J. Physiol.* **463**, 585–592 (2012).

31. Romanov, R. A. *et al.* The ATP permeability of pannexin 1 channels in a heterologous system and in mammalian taste cells is dispensable. *J. Cell Sci.* **125**, 5514–5523 (2012).

32. Allen, N. J. Sequential Release of GABA by Exocytosis and Reversed Uptake Leads to Neuronal Swelling in Simulated Ischemia of Hippocampal Slices. *J. Neurosci.* **24**, 3837–3849 (2004).

33. Van der Kloot, W. Acetylcholine quanta are released from vesicles by exocytosis (and why some think not). *Neuroscience* **24**, 1–7 (1988).

34. Rahman, M. A. *et al.* Norepinephrine exocytosis stimulated by α–latrotoxin requires both external and stored Ca 2+ and is mediated by latrophilin, G proteins and phospholipase C. *Philos. Trans. R. Soc. London. Ser. B Biol. Sci.* **354**, 379–386 (1999).

35. Elmore, S. Apoptosis: A Review of Programmed Cell Death. *Toxicol. Pathol.*

35, 495–516 (2007).

36. Richter, C., Schweizer, M., Cossarizza, A. & Franceschi, C. Control of apoptosis by the cellular ATP level. *FEBS Lett.* **378**, 107–110 (1996).

37. Zamaraeva, M. V *et al.* Cells die with increased cytosolic ATP during apoptosis: a bioluminescence study with intracellular luciferase. *Cell Death Differ.* **12**, 1390–1397 (2005).

38. Cotrina, M. L., Lin, J. H.-C., López-García, J. C., Naus, C. C. G. & Nedergaard, M. ATP-Mediated Glia Signaling. *J. Neurosci.* **20**, 2835–2844 (2000).

39. Taruno, A. *et al.* CALHM1 ion channel mediates purinergic neurotransmission of sweet, bitter and umami tastes. *Nature* **495**, 223–226 (2013).

40. Reisin, I. L. *et al.* The cystic fibrosis transmembrane conductance regulator is a dual ATP and chloride channel. *J. Biol. Chem.* **269**, 20584–91 (1994).

41. Dahl, G. ATP release through pannexon channels. *Philos. Trans. R. Soc. B Biol. Sci.* **370**, 1–11 (2015).

42. Locovei, S., Bao, L. & Dahl, G. Pannexin 1 in erythrocytes: Function without a gap. *Proc. Natl. Acad. Sci.* **103**, 7655–7659 (2006).

43. Leybaert, L. *et al.* Connexin Channels, Connexin Mimetic Peptides and ATP Release. *Cell Commun. Adhes.* **10**, 251–257 (2003).

44. Taylor, K. A., Wright, J. R. & Mahaut-Smith, M. P. Regulation of Pannexin-1 channel activity: Table 1. *Biochem. Soc. Trans.* **43**, 502–507 (2015).

45. Bao, L., Locovei, S. & Dahl, G. Pannexin membrane channels are mechanosensitive conduits for ATP. *FEBS Lett.* **572**, 65–68 (2004).

46. Grygorczyk, R., Tabcharani, J. A. & Hanrahan, J. W. CFTR Channels Expressed in CHO Cells Do Not Have Detectable ATP Conductance. *J. Membr. Biol.* **151**, 139–148 (1996).

47. Bargiotas, P. *et al.* Pannexins in ischemia-induced neurodegeneration. *Proc. Natl. Acad. Sci. U. S. A.* **108**, 20772–20777 (2011).

48. Idzko, M., Ferrari, D. & Eltzschig, H. K. Nucleotide signalling during inflammation. *Nature* **509**, 310–317 (2014).

49. Adamson, S. E. *et al.* Pannexin 1 is required for full activation of insulin-stimulated glucose uptake in adipocytes. *Mol. Metab.* **4**, 610–618 (2015).

50. Yang, K. *et al.* Mechanisms of Pannexin 1 (PANX1) Channel Mechanosensitivity and Its Pathological Roles. *Int. J. Mol. Sci.* **23**, 1523 (2022).

51. Wang, J. & Dahl, G. Pannexin1: a multifunction and multiconductance and/or permeability membrane channel. *Am. J. Physiol. Physiol.* **315**, (2018).

52. Ma, W., Hui, H., Pelegrin, P. & Surprenant, A. Pharmacological Characterization of Pannexin-1 Currents Expressed in Mammalian Cells. *J. Pharmacol. Exp. Ther.* **328**, 409–418 (2009).

53. Dahl, G. The Pannexin1 membrane channel: distinct conformations and functions. *FEBS Lett.* **592**, 3201–3209 (2018).

54. Grizel, A. V, Glukhov, G. S. & Sokolova, O. S. Mechanisms of activation of voltage-gated potassium channels. *Acta Naturae* **6**, 10–26 (2014).

55. Kuzuya, M. *et al.* Structures of human pannexin-1 in nanodiscs reveal gating mediated by dynamic movement of the N terminus and phospholipids. *Sci. Signal.* **15**, (2022).

56. Zhang, S. *et al.* Structure of the full-length human Pannexin1 channel and insights into its role in pyroptosis. *Cell Discov.* **7**, (2021).

57. Deng, Z. *et al.* Cryo-EM structures of the ATP release channel pannexin 1. *Nat. Struct. Mol. Biol.* **27**, 373–381 (2020).

58. Chiu, Y. H., Schappe, M. S., Desai, B. N. & Bayliss, D. A. Revisiting multimodal activation and channel properties of Pannexin 1. *J. Gen. Physiol.* **150**, 19–39 (2018).

59. Michalski, K., Henze, E., Nguyen, P., Lynch, P. & Kawate, T. The weak voltage dependence of pannexin 1 channels can be tuned by N-terminal modifications. *J. Gen. Physiol.* **150**, 1758–1768 (2018).

60. Silverman, W. R. *et al.* The Pannexin 1 Channel Activates the Inflammasome in Neurons and Astrocytes. *J. Biol. Chem.* **284**, 18143–18151 (2009).

61. Li, S., Bjelobaba, I. & Stojilkovic, S. S. Interactions of Pannexin1 channels with purinergic and NMDA receptor channels. *Biochim. Biophys. Acta - Biomembr.* **1860**, 166–173 (2018).

62. Wilkaniec, A. *et al.* P2X7 receptor-pannexin 1 interaction mediates extracellular alpha-synuclein-induced ATP release in neuroblastoma SH-SY5Y cells. *Purinergic Signal.* **13**, 347–361 (2017).

63. Sawynok, J. Adenosine receptor activation and nociception. *Eur. J. Pharmacol.* **347**, 1–11 (1998).

64. Harcha, P. A., López-López, T., Palacios, A. G. & Sáez, P. J. Pannexin Channel Regulation of Cell Migration: Focus on Immune Cells. *Front. Immunol.* **12**, (2021).

65. Pelegrin, P. & Surprenant, A. The P2X7 receptor–pannexin connection to dye uptake and IL-1β release. *Purinergic Signal.* **5**, 129–137 (2009).

66. Inoue, H. *et al.* Functional Coupling between the P2X7 Receptor and Pannexin-1 Channel in Rat Trigeminal Ganglion Neurons. *Int. J. Mol. Sci.* **22**, 5978 (2021).

67. Lee, N. S. *et al.* Focused Ultrasound Stimulates ER Localized Mechanosensitive PANNEXIN-1 to Mediate Intracellular Calcium Release in Invasive Cancer Cells. *Front. Cell Dev. Biol.* **8**, (2020).

68. Cocco, R. E. & Ucker, D. S. Distinct Modes of Macrophage Recognition for Apoptotic and Necrotic Cells Are Not Specified Exclusively by Phosphatidylserine Exposure. *Mol. Biol. Cell* **12**, 919–930 (2001).

69. McIlwain, D. R., Berger, T. & Mak, T. W. Caspase Functions in Cell Death and Disease. *Cold Spring Harb. Perspect. Biol.* **5**, a008656–a008656 (2013).

70. Tummers, B. & Green, D. R. Caspase-8: regulating life and death. *Immunol. Rev.* **277**, 76–89 (2017).

71. Ashkenazi, A. Targeting death and decoy receptors of the tumour-necrosis factor superfamily. *Nat. Rev. Cancer* **2**, 420–430 (2002).

72. Robertson, J. D., Enoksson, M., Suomela, M., Zhivotovsky, B. & Orrenius, S.

Caspase-2 Acts Upstream of Mitochondria to Promote Cytochromec Release during Etoposide-induced Apoptosis. *J. Biol. Chem.* **277**, 29803–29809 (2002).

73. Lassus, P., Opitz-Araya, X. & Lazebnik, Y. Requirement for Caspase-2 in Stress-Induced Apoptosis Before Mitochondrial Permeabilization. *Science (80-.).* **297**, 1352–1354 (2002).

74. Guo, Y., Srinivasula, S. M., Druilhe, A., Fernandes-Alnemri, T. & Alnemri, E. S. Caspase-2 Induces Apoptosis by Releasing Proapoptotic Proteins from Mitochondria. *J. Biol. Chem.* **277**, 13430–13437 (2002).

75. Ayna, G. *et al.* ATP release from dying autophagic cells and their phagocytosis are crucial for inflammasome activation in macrophages. *PLoS One* **7**, (2012).

76. Chekeni, F. B. *et al.* Pannexin 1 channels mediate 'find-me' signal release and membrane permeability during apoptosis. *Nature* **467**, 863–867 (2010).

77. Chiu, Y. H. *et al.* A quantized mechanism for activation of pannexin channels. *Nat. Commun.* **8**, 1–15 (2017).

78. Bunse, S., Schmidt, M., Prochnow, N., Zoidl, G. & Dermietzel, R. Intracellular Cysteine 346 Is Essentially Involved in Regulating Panx1 Channel Activity. *J. Biol. Chem.* **285**, 38444–38452 (2010).

79. Lohman, A. W. *et al.* S-nitrosylation inhibits pannexin 1 channel function. *J. Biol. Chem.* **287**, 39602–39612 (2012).

80. DeLalio, L. J. *et al.* Constitutive SRC-mediated phosphorylation of pannexin 1 at tyrosine 198 occurs at the plasma membrane. *J. Biol. Chem.* **294**, 6940–6956 (2019).

81. Ishikawa, M. *et al.* Pannexin 3 ER Ca2+ channel gating is regulated by phosphorylation at the Serine 68 residue in osteoblast differentiation. *Sci. Rep.* **9**, 1–14 (2019).

82. Penuela, S., Harland, L., Simek, J. & Laird, D. W. Pannexin channels and their links to human disease. *Biochem. J.* **461**, 371–381 (2014).

83. Navis, K. E., Fan, C. Y., Trang, T., Thompson, R. J. & Derksen, D. J. Pannexin 1 Channels as a Therapeutic Target: Structure, Inhibition, and Outlook. *ACS*

Chem. Neurosci. **11**, 2163–2172 (2020).

84. Eltzschig, H. K., Sitkovsky, M. V. & Robson, S. C. Purinergic Signaling during Inflammation. *N. Engl. J. Med.* **367**, 2322–2333 (2012).

85. Poon, I. K. H. *et al.* Unexpected link between an antibiotic, pannexin channels and apoptosis. *Nature* **507**, 329–334 (2014).

86. Zhang, P. *et al.* Pannexin-3 Deficiency Delays Skin Wound Healing in Mice due to Defects in Channel Functionality. *J. Invest. Dermatol.* **139**, 909–918 (2019).

87. Ishikawa, M. & Yamada, Y. The Role of Pannexin 3 in Bone Biology. *J. Dent. Res.* **96**, 372–379 (2017).

88. Penuela, S. *et al.* Loss of pannexin 1 attenuates melanoma progression by reversion to a melanocytic phenotype. *J. Biol. Chem.* **287**, 29184–29193 (2012).

89. Jiang, T. *et al.* Altered expression of pannexin proteins in patients with temporal lobe epilepsy. *Mol. Med. Rep.* **8**, 1801–1806 (2013).

90. Santiago, M. F. *et al.* Targeting pannexin1 improves seizure outcome. *PLoS One* **6**, (2011).

91. Kim, Y. *et al.* Connexins and Pannexins in cerebral ischemia. *Biochim. Biophys. acta. Biomembr.* **1860**, 224–236 (2018).

92. Bargiotas, P. *et al.* Pannexins in ischemia-induced neurodegeneration. *Proc. Natl. Acad. Sci.* **108**, 20772–20777 (2011).

93. Good, M. E. *et al.* Pannexin 1 channels as an unexpected new target of the anti-hypertensive drug spironolactone. *Circ. Res.* **122**, 606–615 (2018).

94. Moon, P. M. *et al.* Deletion of Panx3 Prevents the Development of Surgically Induced Osteoarthritis. *J. Mol. Med.* **93**, 845–856 (2015).

95. O'Donnell, B. L. & Penuela, S. Pannexin 3 channels in health and disease. *Purinergic Signal.* **17**, 577–589 (2021).

96. Feig, J. L. *et al.* The antiviral drug tenofovir, an inhibitor of Pannexin-1-mediated ATP release, prevents liver and skin fibrosis by downregulating

adenosine levels in the liver and skin. *PLoS One* **12**, 1–22 (2017).

97. Poon, I. K. H. *et al.* Unexpected link between an antibiotic, pannexin channels and apoptosis. *Nature* **507**, 329–334 (2014).

98. Burma, N. E. *et al.* Blocking microglial pannexin-1 channels alleviates morphine withdrawal in rodents. *Nat. Med.* **23**, 355–360 (2017).

99. Michalski, K. & Kawate, T. Carbenoxolone inhibits Pannexin1 channels through interactions in the first extracellular loop. *J. Gen. Physiol.* **147**, 165–174 (2016).

100. Burma, N. E. *et al.* Blocking microglial pannexin-1 channels alleviates morphine withdrawal in rodents. *Nat. Med.* **23**, 355–360 (2017).

101. Shao, Q. *et al.* A germline variant in the PANX1 gene has reduced channel function and is associated with multisystem dysfunction. *J. Biol. Chem.* **291**, 12432–12443 (2016).

102. Purohit, R. & Bera, A. K. Mutational effects of Pannexin 1 R217H depend on the carboxyl-terminus. *Biochem. Biophys. Res. Commun.* **548**, 143–147 (2021).

103. Drożdżyk, K. *et al.* Cryo-EM structures and functional properties of CALHM channels of the human placenta. *Elife* **9**, (2020).

104. Burendei, B. *et al.* Cryo-EM structures of undocked innexin-6 hemichannels in phospholipids. *Sci. Adv.* **6**, (2020).

105. Lee, H.-J. *et al.* Cryo-EM structure of human Cx31.3/GJC3 connexin hemichannel. *Sci. Adv.* **6**, (2020).

106. Kasuya, G. *et al.* Cryo-EM structures of the human volume-regulated anion channel LRRC8. *Nat. Struct. Mol. Biol.* **25**, 797–804 (2018).

107. Syeda, R. *et al.* LRRC8 Proteins Form Volume-Regulated Anion Channels that Sense Ionic Strength. *Cell* **164**, 499–511 (2016).

108. Nakamura, R. *et al.* Cryo-EM structure of the volume-regulated anion channel LRRC8D isoform identifies features important for substrate permeation. *Commun. Biol.* **3**, 240 (2020).

109. Karakas, E. Structure of a LRRC8 chimera with physiologically relevant properties reveals heptameric assembly and pore-blocking lipids. 1–27 (2022).

110. Dreses-Werringloer, U. *et al.* A Polymorphism in CALHM1 Influences Ca2+ Homeostasis, Aβ Levels, and Alzheimer's Disease Risk. *Cell* **133**, 1149–1161 (2008).

111. Demura, K. *et al.* Cryo-EM structures of calcium homeostasis modulator channels in diverse oligomeric assemblies. *Sci. Adv.* **6**, (2020).

112. Boassa, D., Nguyen, P., Hu, J., Ellisman, M. H. & Sosinsky, G. E. Pannexin2 oligomers localize in the membranes of endosomal vesicles in mammalian cells while pannexin1 channels traffic to the plasma membrane. *Front. Cell. Neurosci.* **8**, 1–15 (2015).

113. Vasseur, M. Le. The role of Pannexin 2 in mitochondrial functions and cell death. (2016).

114. Lai, C. P. K., Bechberger, J. F. & Naus, C. C. Pannexin2 as a novel growth regulator in C6 glioma cells. *Oncogene* **28**, 4402–4408 (2009).

115. Ishikawa, M. *et al.* Pannexin 3 functions as an ER Ca 2+ channel, hemichannel, and gap junction to promote osteoblast differentiation. *J. Cell Biol.* **193**, 1257–1274 (2011).

116. Zhang, P. *et al.* Pannexin 3 regulates skin development via Epiprofin. *Sci. Rep.* **11**, 1–16 (2021).

117. Iwamoto, T. *et al.* Pannexin 3 regulates proliferation and differentiation of odontoblasts via its hemichannel activities. *PLoS One* **12**, 1–20 (2017).

118. Ishikawa, M. *et al.* Pannexin 3 and connexin 43 modulate skeletal development through their distinct functions and expression patterns. *J. Cell Sci.* **129**, 1018–1030 (2016).

119. Smith, A. M. & Klugman, K. P. 'Megaprimer' method of PCR-based mutagenesis: The concentration of megaprimer is a critical factor. *Biotechniques* **22**, 438–442 (1997).

120. Kawate, T. & Gouaux, E. Fluorescence-Detection Size-Exclusion

Chromatography for Precrystallization Screening of Integral Membrane Proteins. *Structure* **14**, 673–681 (2006).

121. Hjelmeland, L. M. [19] Solubilization of native membrane proteins. in 253–264 (1990). doi:10.1016/0076-6879(90)82021-S

122. Kalipatnapu, S. & Chattopadhyay, A. Membrane Protein Solubilization: Recent Advances and Challenges in Solubilization of Serotonin1A Receptors. *IUBMB Life (International Union Biochem. Mol. Biol. Life)* **57**, 505–512 (2005).

123. Lenoir, G. *et al.* Screening of Detergents for Stabilization of Functional Membrane Proteins. *Curr. Protoc. protein Sci.* **93**, e59 (2018).

124. Lee, H. & Hu, Y. Expression in mammalian cells using BacMam viruses. *Expr. Syst. Methods Express* 261–276 (2007).

125. Goehring, A. *et al.* Screening and large-scale expression of membrane proteins in mammalian cells for structural studies. *Nat. Protoc.* **9**, 2574–2585 (2014).

126. Hofmann, C. *et al.* Efficient gene transfer into human hepatocytes by baculovirus vectors. *Proc. Natl. Acad. Sci.* **92**, 10099–10103 (1995).

127. Boyce, F. M. & Bucher, N. L. Baculovirus-mediated gene transfer into mammalian cells. *Proc. Natl. Acad. Sci.* **93**, 2348–2352 (1996).

128. Dukkipati, A., Park, H. H., Waghray, D., Fischer, S. & Garcia, K. C. BacMam system for high-level expression of recombinant soluble and membrane glycoproteins for structural studies. *Protein Expr. Purif.* **62**, 160–170 (2008).

129. Ely, L. K., Fischer, S. & Garcia, K. C. Structural basis of receptor sharing by interleukin 17 cytokines. *Nat. Immunol.* **10**, 1245–1251 (2009).

130. Juers, D. H., Matthews, B. W. & Huber, R. E. LacZ β-galactosidase: Structure and function of an enzyme of historical and molecular biological importance. *Protein Sci.* **21**, 1792–1807 (2012).

131. Ullmann, A., Jacob, F. & Monod, J. Characterization by in vitro complementation of a peptide corresponding to an operator-proximal segment of the β-galactosidase structural gene of Escherichia coli. *J. Mol. Biol.* **24**, 339–

343 (1967).

132. Brandt, M. E., Gabrik, A. H. & Vickery, L. E. A vector for directional cloning and expression of polymerase chain reaction products in Escherichia coli. *Gene* **97**, 113–117 (1991).

133. Weissenberger, G., Henderikx, R. J. M. & Peters, P. J. Understanding the invisible hands of sample preparation for cryo-EM. *Nat. Methods* **18**, 463–471 (2021).

134. Punjani, A., Rubinstein, J. L., Fleet, D. J. & Brubaker, M. A. CryoSPARC: Algorithms for rapid unsupervised cryo-EM structure determination. *Nat. Methods* **14**, 290–296 (2017).

135. Deploying CryoSPARC on AWS - CryoSPARC Guide.

136. Noble, A. J. *et al.* Routine single particle CryoEM sample and grid characterization by tomography. *Elife* **7**, (2018).

137. Moriya, T. *et al.* Size matters: optimal mask diameter and box size for single-particle cryogenic electron microscopy. *bioRxiv* 2020.08.23.263707 (2020).

138. Punjani, A., Zhang, H. & Fleet, D. J. Non-uniform refinement: adaptive regularization improves single-particle cryo-EM reconstruction. *Nat. Methods* **17**, 1214–1221 (2020).

139. Varadi, M. *et al.* AlphaFold Protein Structure Database: massively expanding the structural coverage of protein-sequence space with high-accuracy models. *Nucleic Acids Res.* **50**, D439–D444 (2022).

140. Jumper, J. *et al.* Highly accurate protein structure prediction with AlphaFold. *Nature* **596**, 583–589 (2021).

141. Pettersen, E. F. *et al.* UCSF Chimera?A visualization system for exploratory research and analysis. *J. Comput. Chem.* **25**, 1605–1612 (2004).

142. Adams, P. D. *et al.* PHENIX : a comprehensive Python-based system for macromolecular structure solution. *Acta Crystallogr. Sect. D Biol. Crystallogr.* **66**, 213–221 (2010).

143. Emsley, P. & Cowtan, K. Coot : model-building tools for molecular graphics.

Acta Crystallogr. Sect. D Biol. Crystallogr. **60**, 2126–2132 (2004).

144. Huang, L. & Zhang, C. Microscale Thermophoresis (MST) to Detect the Interaction Between Purified Protein and Small Molecule. in 187–193 (2021). doi:10.1007/978-1-0716-0954-5_17

145. Velasquez, S. & Eugenin, E. A. Role of Pannexin-1 hemichannels and purinergic receptors in the pathogenesis of human diseases. *Front. Physiol.* **5 MAR**, 1–12 (2014).

146. Wang, J. & Dahl, G. Pannexin1: a multifunction and multiconductance and/or permeability membrane channel. *Am. J. Physiol. Physiol.* **315**, C290–C299 (2018).

147. Anandan, A. & Vrielink, A. Detergents inmembrane protein purification and crystallisation. *Adv. Exp. Med. Biol.* **922**, 13–28 (2016).

148. Linke, D. Chapter 34 Detergents. in 603–617 (2009). doi:10.1016/S0076-6879(09)63034-2

149. Chae, P. S. *et al.* A new class of amphiphiles bearing rigid hydrophobic groups for solubilization and stabilization of membrane proteins. *Chem. - A Eur. J.* **18**, 9485–9490 (2012).

150. Grouleff, J., Irudayam, S. J., Skeby, K. K. & Schiøtt, B. The influence of cholesterol on membrane protein structure, function, and dynamics studied by molecular dynamics simulations. *Biochim. Biophys. Acta - Biomembr.* **1848**, 1783–1795 (2015).

151. Scheres, S. H. W. RELION: Implementation of a Bayesian approach to cryo-EM structure determination. *J. Struct. Biol.* **180**, 519–530 (2012).

152. Scheres, S. H. W. A Bayesian View on Cryo-EM Structure Determination. *J. Mol. Biol.* **415**, 406–418 (2012).

153. Oshima, A., Tani, K. & Fujiyoshi, Y. Atomic structure of the innexin-6 gap junction channel determined by cryo-EM. *Nat. Commun.* **7**, 13681 (2016).

154. Maeda, S. *et al.* Structure of the connexin 26 gap junction channel at 3.5 Å resolution. *Nature* **458**, 597–602 (2009).

155. Qi, C. *et al.* Structure of the connexin-43 gap junction channel reveals a closed sieve-like molecular gate. *bioRxiv* 2022.03.26.485947 (2022).

156. Chen, J., Noble, A. J., Kang, J. Y. & Darst, S. A. Eliminating effects of particle adsorption to the air/water interface in single-particle cryo-electron microscopy: Bacterial RNA polymerase and CHAPSO. *J. Struct. Biol. X* **1**, 100005 (2019).

157. Wang, J. & Dahl, G. SCAM analysis of Panx1 suggests a peculiar pore structure. *J. Gen. Physiol.* **136**, 515–527 (2010).

158. Ambrosi, C. *et al.* Pannexin1 and Pannexin2 Channels Show Quaternary Similarities to Connexons and Different Oligomerization Numbers from Each Other. *J. Biol. Chem.* **285**, 24420–24431 (2010).

159. Imamura, H. *et al.* Single-cell dynamics of pannexin-1-facilitated programmed ATP loss during apoptosis. *Elife* **9**, (2020).

160. Sandilos, J. K. *et al.* Pannexin 1, an ATP Release Channel, Is Activated by Caspase Cleavage of Its Pore-associated C-terminal Autoinhibitory Region. *J. Biol. Chem.* **287**, 11303–11311 (2012).

161. Wang, J. & Dahl, G. SCAM analysis of Panx1 suggests a peculiar pore structure. *J. Gen. Physiol.* **136**, 515–527 (2010).

162. Kasuya, G. *et al.* Cryo-EM structures of the human volume-regulated anion channel LRRC8. *Nat. Struct. Mol. Biol.* **25**, (2018).

163. Oshima, A., Tani, K. & Fujiyoshi, Y. Atomic structure of the innexin-6 gap junction channel determined by cryo-EM. *Nat. Commun.* **7**, 1–8 (2016).

164. Shao, Q. *et al.* A germline variant in the PANX1 gene has reduced channel function and is associated with multisystem dysfunction. *J. Biol. Chem.* **291**, 12432–12443 (2016).

165. Qiu, F., Wang, J. & Dahl, G. Alanine substitution scanning of pannexin1 reveals amino acid residues mediating ATP sensitivity. *Purinergic Signal.* **8**, 81–90 (2012).

166. Syrjanen, J., Michalski, K., Kawate, T. & Furukawa, H. On the molecular nature of large-pore channels. *J. Mol. Biol.* **433**, 166994 (2021).

167. Iwamoto, T. *et al.* Pannexin 3 regulates proliferation and differentiation of odontoblasts via its hemichannel activities. *PLoS One* **12**, e0177557 (2017).

168. Postis, V. *et al.* The use of SMALPs as a novel membrane protein scaffold for structure study by negative stain electron microscopy. *Biochim. Biophys. Acta - Biomembr.* **1848**, 496–501 (2015).

169. Hellwig, N. *et al.* Native mass spectrometry goes more native: investigation of membrane protein complexes directly from SMALPs. *Chem. Commun.* **54**, 13702–13705 (2018).

170. Sahu, I. D. *et al.* DEER EPR Measurements for Membrane Protein Structures via Bifunctional Spin Labels and Lipodisq Nanoparticles. *Biochemistry* **52**, 6627–6632 (2013).

171. Karlova, M. G. *et al.* Detergent-free solubilization of human Kv channels expressed in mammalian cells. *Chem. Phys. Lipids* **219**, 50–57 (2019).

172. Knowles, T. J. *et al.* Membrane proteins solubilized intact in lipid containing nanoparticles bounded by styrene maleic acid copolymer. *J. Am. Chem. Soc.* **131**, 7484–7485 (2009).

173. Knowles, T. J. *et al.* Membrane Proteins Solubilized Intact in Lipid Containing Nanoparticles Bounded by Styrene Maleic Acid Copolymer. *J. Am. Chem. Soc.* **131**, 7484–7485 (2009).

174. Dahl, G. ATP release through pannexon channels. *Philos. Trans. R. Soc. B Biol. Sci.* **370**, 1–11 (2015).

175. Syrjanen, J. L. *et al.* Structure and assembly of calcium homeostasis modulator proteins. *Nat. Struct. Mol. Biol.* **27**, 150–159 (2020).

176. Kern, D. M. *et al.* Structural basis for assembly and lipid-mediated gating of LRRC8A:C volume-regulated anion channels. *bioRxiv* 2022.07.31.502239 (2022).

177. Kane Dickson, V., Pedi, L. & Long, S. B. Structure and insights into the function of a Ca2+-activated Cl− channel. *Nature* **516**, 213–218 (2014).

178. Zhang, S. *et al.* Structure of the full-length human Pannexin1 channel and

insights into its role in pyroptosis. *Cell Discov.* **7**, 30 (2021).

179. Smart, O. S., Neduvelil, J. G., Wang, X., Wallace, B. A. & Sansom, M. S. P. HOLE: A program for the analysis of the pore dimensions of ion channel structural models. *J. Mol. Graph.* **14**, 354–360 (1996).